MAY 2018

Ph.D. in Mechanical Engineering

HAKAN ÇANDAR

UNIVERSITY OF GAZİANTEP

GRADUATE SCHOOL OF

NATURAL & APPLIED SCIENCES

EXPERIMENTAL AND NUMERICAL ANALYSIS OF AUTOFRETTAGE PROCESS FOR THICK WALLED CYLINDERS

Ph.D. THESIS

IN

MECHANICAL ENGINEERING

BY

HAKAN ÇANDAR

MAY 2018

Experimental and Numerical Analysis of Autofrettage Process for Thick Walled Cylinders

Ph.D. Thesis

in

Mechanical Engineering

University of Gaziantep

Supervisor

Prof. Dr. İ. Hüseyin FİLİZ

by

Hakan ÇANDAR

May 2018

REPUBLIC OF TURKEY
UNIVERSITY OF GAZİANTEP
GRADUATE SCHOOL OF NATURAL & APPLIED SCIENCES
MECHANICAL ENGINEERING

Name of the thesis: Experimental and Numerical Analysis of Autofrettage Process for Thick Walled Cylinders

Name of the student: Hakan ÇANDAR
Exam date: 04/05/2018

Approval of the Graduate School of Natural and Applied Sciences

Prof. Dr. Ahmet Necmeddin YAZICI
Director

I certify that this thesis satisfies all the requirements as a thesis for the degree of Doctor of Philosophy.

Prof. Dr. Mehmet Sait SÖYLEMEZ
Head of Department

This is to certify that we have read this thesis and that in our majority opinion it is fully adequate, in scope and quality, as a thesis for the degree of Doctor of Philosophy.

Prof. Dr. İ. Hüseyin FİLİZ
Supervisor

Examining Committee Members:	Signature
Prof. Dr. İ. Hüseyin FİLİZ	....
Prof. Dr. Ömer Faruk BAKKALOĞLU	....
Prof. Dr. Ömer EYERCİOĞLU	....
Prof. Dr. Abdülkadir EKŞİ	....
Prof. Dr. Cengiz DOĞAN	....

I hereby declare that all information in this document has been obtained and presented in accordance with academic rules and ethical conduct. I also declare that, as required by these rules and conduct, I have fully cited and referenced all material and results that are not original to this work.

Hakan ÇANDAR

ABSTRACT

EXPERIMENTAL AND NUMERICAL ANALYSIS OF AUTOFRETTAGE PROCESS FOR THICK WALLED CYLINDERS

ÇANDAR, Hakan
Ph.D. in Mechanical Engineering
Supervisor: Prof. Dr. İ. Hüseyin FİLİZ
May 2018
114 pages

Experimental and numerical and analysis of autofrettage process for thick-walled cylinders is presented in this study. Autofrettage tests are carried out on a hydraulic autofrettage test stand available in Delphi Automotive Systems in İzmir. AISI 4140 steel is used as the test material in the experiments. The samples are produced from a solid cylindrical bar with 10mm inner diameter, 30mm outer diameter and 200mm long. Eight different autofrettage pressures in the range between 530 to 666 MPa are used in the tests. Axial and tangential strains are measured during the tests in order to see the changes in strains with both autofrettage pressure and pressure holding time. Residual stresses developed on the wall of the cylinders due to autofrettage pressure are measured at five different points along the wall of the cylinders by using X-ray diffraction method. Radial and tangential residual stress distributions are plotted in order to see the effects of autofrettage pressure. A finite element model is also created by using ANSYS® Workbench 15.0 to compare the experimental results with the numerical results. 2D axisymmetric analyses are performed for each autofrettage condition. Measured strains during the tests and results obtained from numerical model are found to be almost the same. The tendency of change in the distribution of residual stresses is found to be similar for experimental and numerical results.

Keywords: Hydraulic autofrettage, FEM analysis, Strain measurement, XRD residual stress measurement

ÖZET

KALIN CİDARLI SİLİNDİRLERDE OTOFRETAJ İŞLEMİNİN DENEYSEL VE NÜMERİK ANALİZİ

ÇANDAR, Hakan
Doktora Tezi, Makine Müh. Bölümü
Tez Yöneticisi: Prof. Dr. İ. Hüseyin FİLİZ
Mayıs 2018
114 sayfa

Bu çalışmada, kalın cidarlı silindirlerde otofretaj işleminin deneysel ve numerik analizleri sunulmuştur. Otofretaj testleri, İzmir'de yerleşik Delphi Otomotiv Sistemleri'nde mevcut olan bir hidrolik otofretaj test standında gerçekleştirilmiştir. Deneylerde test malzemesi olarak AISI 4140 çeliği kullanılmıştır. Test numuneleri, 10 mm iç çapında, 30 mm dış çapında ve 200 mm uzunluğunda olacak şekilde içi dolu silindirik bir çubuktan üretilmiştir. Testlerde 530 ile 666 MPa arasında değişen sekiz farklı otofretaj basıncı kullanılmıştır. Gerinimlerin otofretaj basıncı ve basınçta bekleme süresiyle değişimini görmek için test süresince eksenel ve teğetsel gerinimler ölçülmüştür. Otofretaj basıncı nedeniyle silindir duvarında oluşan kalıntı gerilmeler, silindirin duvarı boyunca beş farklı noktadan X-ışını kırınım yöntemi kullanılarak ölçülmüştür. Otofretaj basıncının etkisini görebilmek için radyal ve teğetsel kalıntı gerilme dağılımı grafikleri çizilmiştir. Deneysel sonuçları numerik sonuçlar ile kıyaslamak için ANSYS® 15.0 sonlu elemanlar paketinde bir sonlu elemen modeli oluşturulmuştur. Her bir otofretaj koşulu için iki boyutlu eksenel simetrik analizler yapılmıştır. Testler sırasında ölçülen gerinimler ve nümerik modelden elde edilen sonuçlar hemen hemen aynı bulunmuştur. Kalıntı gerilmelerin dağılımındaki değişim eğilimi, deneysel ve nümerik sonuçlar için benzer bulunmuştur.

Anahtar Kelimeler: Hidrolik otofretajlama, Sonlu eleman analizi, Gerinim ölçümü, X-ışını kırınımı ile kalıntı gerilme ölçümü.

To my lovely daughter, ECE…

ACKNOWLEDGEMENTS

I would like to express my deep gratitude to my supervisor, Prof. Dr. İ. Hüseyin FİLİZ for his patient guidance, enthusiastic encouragement, useful critiques and constructive suggestions during the planning and development of this thesis.

I would like to thank to Delphi Automotive Systems in İzmir, Turkey for technical support during the autofrettage experiments, Maximator GmbH Nordhausen, Germany for the documents about autofrettage process and The Metal Forming Centre of Excellence (MFCE) in ATILIM University, Ankara, Turkey for XRD residual stress measurements. Special thanks to Prof. Dr. Bilgin KAFTANOĞLU for his interest and support.

My special thanks are extended to Prof. Dr. Ömer EYERCİOĞLU and Assoc. Prof. Necip Fazıl YILMAZ for the continuous motivation and support. I also would like to thank my colleagues Res. Assist. Mahmut TANDOĞAN and Res. Assist. Özkan ÖZBEK for their assistance and encouragement.

Deepest gratitude is to my parents, for their endless support, interest and prays. I especially thank my father, M. Şevket ÇANDAR for never left me alone in this way.

Special thanks to my wife, Dürdane ÇANDAR for her continuous encouragement, patience and real love.

Finally, I would like to thank Gaziantep University Scientific Research Council (BAP) due to financial support to this study. The project no is MF.DT.16.12.

TABLE OF CONTENTS

LIST OF TABLES

Pages

LIST OF FIGURES

Pages

LIST OF SYMBOLS

a	Inner radius
b	Elastic-plastic interface radius
c	Outer radius
r	Radial distance
P_i	Internal pressure
P_o	External (outer) pressure
P_a	Autofrettage pressure
F_c	Clamping force in autofrettage process
p	Interface pressure developed between inner and outer members
δ	Total amount of interference between inner and outer members
σ_r	Radial stress
σ_t	Tangential (hoop) stress
σ_z	Axial (longitudinal) stress
σ'	Von Misses stress
ε_r	Radial strain
ε_t	Tangential strain
ε_z	Axial strain
ε'	Equivalent strain
S_{yt}	Yield strength in tension
S_{yc}	Yield strength in compression
S_u	Ultimate strength
S_{ss}	Yield strength in shear

ν	Poisson’s ratio
E	Modulus of elasticity
b_{ef}	Bauschinger effect factor
XRD	X-ray diffraction
ND	Neutron diffraction
SD	Synchrotron diffraction
FEM	Finite element analysis

CHAPTER 1

INTRODUCTION

Thick walled cylinders are very common type of pressure vessels which are designed to store, transfer and process of the liquids, vapours, or gases under the effect of internal or external pressures. They are widely used in chemical, military, automotive industries as well as nuclear power plants. General application of thick-walled cylinders include, cannon and gun barrels, fuel rails in diesel engines, abrasive waterjet equipments (high pressure cylinders of intensifier, nozzle etc.), air compressor units, high pressure reactor vessels used in metallurgical operations. They also appear as components of aerospace and marine vehicles [1,2].

Thick walled cylinders are usually working under high internal pressures which may be constant or cyclic. When a thick walled cylinder is subjected to an internal pressure, three types of stresses are developed as radial (σ_r), tangential (hoop, σ_t) and longitudinal (axial, σ_z) stress. All these stresses are the principle stresses and they are distributed along the wall of the cylinder in such a way that maximum at the inner surface and minimum at the outer surface. Failure occurs due to the effect of equivalence of these stress components (Von Misses stress) at the inner surface which is of tension type. If there is a cyclic loading condition, in this case, alternating component of Von Misses stress causes fatigue failure.

Fatigue life and high strength to weight ratio are two prime requirements that must be considered in the design of thick walled cylinders. In order to improve these requirements without changing any dimensions of the cylinder, the value of Von-Misses stress at the inner surface must be decreased. The only way to do that is to create a compressive type of residual stress at this region. Interference fit was the first process that has been used to meet this demand. In this process, two or more cylinders are mounted on each other with a certain interference to create a useful residual compressive stress at the inner wall of the cylinder. This method seems advantageous especially due to the simplicity of the process. However, there is a problem of using this method for the parts with complex geometry such as tubes and rails. Also, there is no continuity of the hoop stresses at the elastic plastic interface where the critical section is present. That is, the hoop stress on the inner surface of the outer part is different from the hoop stress on the outer surface of the inner part. Sudden change in hoop stress values at this region may cause unexpected failures. These problems mentioned above were solved by the invention of the autofrettage process.

Autofrettage process is an elastic-plastic technique which is widely used in the production of many components such as high pressure cylinders of intensifiers, steel pipes, gun and cannon barrels, injection nozzles, common rails, and fuel lines. In this process, a thick walled cylinder is internally pressurized so that the cylinder becomes partially plastic surrounded by elastic region. The pressure is then released and the outer elastic part of the wall attempt to return to its original diameter, thus tries to compress the inner plastic part and causes useful compressive residual stresses at the inner surface [3].

There are many different types of autofrettage methods. Mechanical (swage) and hydraulic autofrettage are the most commonly used methods [4]. In addition to these methods, some new methods such as thermal, rotational, explosive and creep autofrettage have been developed in recent years [5-7]. Among these methods, short processing time and applicability to complex parts make hydraulic autofrettage the most preferred method.

The main problem in the hydraulic autofrettage process is to determine the reasonable value of autofrettage pressure for the given application. This pressure is governed by the values of residual stresses developed on the wall of the cylinder. As the residual stresses are known then the optimum autofrettage pressure is determined in such a way that the maximum Von Misses stress due to working pressure will be minimum. Determining the optimum autofrettage pressure allows the user to obtain maximum benefit from the autofrettage process. Numerous attempts have been made for this purpose by using both analytical and numerical methods. Owing to simplifying assumptions made in the analytical and numerical methods, the accuracy of the evaluation of the stress distributions may be limited. Hence, experimental investigation of stress distributions may be of great help in this respect.

In this thesis, an experimental study was carried out to investigate the stress distributions in the hydraulic autofrettage process. Thick-walled cylinders made from AISI 4140 steel with 10 mm inner diameter, 30 mm outer diameter and 200 mm long were autofrettaged under 8 different pressures which were selected in the range of minimum and maximum autofrettage pressures calculated based on an analytical model proposed by Huang [12]. Strain distributions during the autofrettage process were measured with strain gauges mounted on the outer surface of each specimen. After autofrettage process, residual stresses in tangential and radial directions were measured at five different points on the half section of the cylinders by using XRD method. Electro-polishing was applied to eliminate detrimental effects of cutting process before the residual stress measurements. A FE model was then developed based on the experimental setup to verify experimental results by using ANSYS Workbench 15.0. 2D axisymmetric analyses were performed for each autofrettage conditions. Stress-strain behaviour of the material was assumed as multi-linear isotropic in the plastic region. The autofrettage test unit itself creates a clamping force in axial direction as to improve sealing requirement. This force was included in the numerical analyses as a compression load in addition to the autofrettage pressures. Experimental and numerical results were then compared with each other and a coherent relation was obtained between the results.

There are many researches in the literature on hydraulic autofrettage process. The vast majority of the works have been done in the defence industry, the nuclear industry and the automotive industry in developed countries or countries that follow a self-development policy. In this context, prominent studies are seen especially in the UK, the USA, Israel, Iran, China and India. In our country, this issue has been handled by only a few researchers and there is a lack of knowledge about how to apply this process. This study is going to fill this gap and build up a platform on which further researches based. On the other hand, thick walled cylinders used in many industrial applications are imported from abroad at extremely high prices. It is the intention of this thesis to start to produce high pressure cylinders at home. Also, as the material of the samples used in this thesis has similar mechanical properties and dimensions with fuel rails used in diesel engines, the results obtained in this study may contribute to the autofrettage process of fuel rails.

Topics covered in this thesis are namely; introduction, literature survey, analysis of thick walled cylinders, experimental and numerical study, results and discussion and conclusions and future works. Literatures related to mathematical modelling and experimental investigation of hydraulic autofrettage process are presented in Chapter 2. Optimization studies on autofrettage process are also presented in this chapter. Analysis of thick walled cylinders is briefly presented and the autofrettage process is introduced in Chapter 3. In Chapter 4, equipments used in the experimental work are presented and the procedures followed in the experimental study are explained in detail. Also, construction of FE model is presented and numerical model is verified by comparing the results with the analytical results for a sample autofrettage pressure. The results obtained from both experimental and numerical studies are presented and compared to each other in Chapter 5. Last chapter, Chapter 6 is devoted to conclusions and recommendations for future works.

CHAPTER 2

LITERATURE REVIEW

2.1 Introduction

Many researchers have studied the autofrettage process. These studies can be classified in three groups as analytical, numerical and experimental studies. In this chapter, the emphasis is given to the studies on hydraulic autofrettage process which is used in the experimental work and some of those studies are summarized in the following sections. Reviews of studies on both analytical and FE modelling of the autofrettage process are presented first. The experimental studies and the studies on optimization of autofrettage process are then presented.

2.2 Studies on Mathematical Modelling of Hydraulic Autofrettage Process

In general, modelling of a typical autofrettage process consists of formulating a set of differential equations which are solved by applying proper boundary conditions and assumptions. The elastic limit of the cylinder is governed by a yield criterion. The stresses developed on the wall of the cylinder after yielding is described by a strain hardening function. Since the loading cycle in an autofrettage process includes an unloading stage which may result as reverse yielding, the Bauschinger effect also becomes an important factor [8].

Hill [9] proposed the first analytical autofrettage model by assuming the stress–strain relationship of the material as elastic-perfectly plastic (EPP). This model is limited in accuracy because of the Bauschinger effect and strain hardening, but it provides a good approximation when the plastic deformation is low. Topcu and Filiz [10] compared the performance characteristics of shrink fit and autofrettage processes by going through analytical and numerical analysis by assuming the material behaviour as elastic-perfectly plastic. For optimum interference value of shrink fit and autofrettage pressure, shrink fit process provided less Von Misses stress at the critical section than the autofrettage process under a certain amount of working pressure.

Milligan et al. [11] investigated the Bauschinger effect in a 4330 modified steel and showed dependency of this effect on plastic strains. They used both a conventional approach and a new technique which takes strain-hardening into account in the determination of the magnitude of the Bauschinger effect. They found that, the Bauschinger effect was independent of yield strength for three different strength levels of the martensitic material and it increased with increasing permanent strain up to approximately 2 percent and thereafter remained essentially constant. They also stated that the typical values of Bauschinger effect factor (b_{ef}) was in the range 0.3–1.0.

Huang [12], proposed an autofrettage model considering the material strain hardening relationship and Bauschinger effect, based on actual tensile-compressive curve of material, modified yield criterion, and plane-strain, incompressible conditions. They found that the smaller Bauschinger effect coefficient (b_{ef}) causes the reverse yielding to take place more easily and affects the residual stress distribution. They also state the influence of different yielding criteria in their study. Çandar and Filiz [13] developed a bi-linear kinematic-hardening model by using the same assumptions considered in the Huang's model.

White el al. [14] developed an improved isotropic-kinematic hardening model based on the mechanical properties of the material which were determined by different types of tests including tension tests, large strain compression tests, reverse loading tests, symmetric strain cyclic tests, unsymmetric strain cyclic tests (mean stress relaxation), unsymmetric stress cyclic tests (cyclic ratcheting), and large strain torsion tests. Key features of small strain uniaxial cyclic behavior was captured well in this model. Although the model was able to predict a monotonic increase of both the shear stress and the normal compressive stress toward saturation values in monotonic large strain torsion tests, the predicted stress levels were not in very good agreement with the experimental results.

Parker et al. [15] started their investigations on autofrettaged mono-block cylinders by comparing different unloading models and then Parker [16] extended this work by taking into account the Bauschinger effect. He found that the Bauschinger effect is significant when the autofrettage radius to bore radius exceeds 1.2 and the material exhibits an elastic-perfectly plastic behaviour below this ratio.

Eun Yeup Lee et al. [17] investigated the elastic- perfectly plastic and strain hardening models for autofrettaged compound cylinder. They found that the compressive residual stress of the strain hardening model is smaller than that of the elastic- perfectly plastic model because of the bauschinger effect.

Chen [18] obtained a closed-form solution for calculating the residual stresses and strains with reverse yielding in the autofrettaged cylinders. In this model, the small strain hardening at loading stage was neglected, but the large strain-hardening after reverse yielding was taking into account. It was found from the numerical results that the influence of the combined Bauschinger and hardening effects on the residual stress distribution was significant.

Ragab et al. [19] used a generalized material behaviour model includes reverse yielding, non-linear hardening and Bauschinger effect. They used high strength steel known commercially as gun steel as a test specimen and experiments were conducted by moving a swage mandrel through the test tube. Theoretical calculations and experimental results of both residual stress and diametral expansions are found as very close to each other.

Researchers have also used the FE model to simulate accurate material behaviour or validate newly developed numerical models. The Von Misses yield criteria is used in most of the FE model [8]. Chen and O'Hara [20] carried out a FEM simulation by using ADINA® which is a general purpose finite element program for Automatic Dynamic Incremental Nonlinear Analysis. A multi-linear stress-strain curve was used in both isotropic and kinematic material models. Four different wall ratios (b/a) were considered in the analyses. They found that there was a considerable difference between hoop stress results obtained from these two material models.

Gibson et al. [21] create a framework to represent realistic behaviour of candidate gun steels by using USERMAT subroutine in ANSYS®. A723 is used in simulations of both uni-axial test and hydraulic autofrettage to verify the model. They compared the results with spreadsheet data from the material-fit equations and equivalent results from the Hencky program and close agreement was observed between the results in both cases.

Feng et al. [22] carried out FE analysis to investigate the efficiency of low-temperature autofrettage for the austenitic stainless steel AISI 304 L on residual compressive stress at the inner wall of the cylinder. The thick-walled cylinder considered as infinitely long is subjected to both a particular ambient temperature and pressure. MARC K6.1 FE code was employed to calculate the stresses and strains developed in the cylinder. A more beneficial residual stress pattern was obtained at low temperatures rather than at room temperature. For the steel investigated in this study with wall thickness ratio of 3, the optimum temperature pressure values were determined as -90° and 400 MPa respectively.

Çandar and Filiz [13] compared the stress results for loading unloading and operating stages of autofrettage process obtained from both analytical model and FE model which was created by using ANSYS® Workbench 15.0. Quarter of the cylinder was modelled by using symmetric boundary conditions. Plane strain method was selected in the analyses. The results obtained from both methods were found to be almost the same.

2.3 Experimental Studies on Autofrettage Process

Experimental studies involve building up an experimental setup on the one hand, and measurements of stresses and strains on the wall of the autofrettaged cylinders on the other hand. In the experimental studies, different techniques are used for autofrettage process and for measurements of stresses. This section is devoted to a review of some of those experimental studies.

In the determination of residual stresses induced in the cylinder wall due to autofrettage pressure, both destructive and non-destructive methods have been used by many researchers. Hole drilling and Sach’s boring are mostly used destructive methods. Jahed et al. [23] and George and Smith [24] used the hole drilling technique for hydraulically autofrettaged cylinders. Franklin and Morrison [25], Faupel [26] and Stacey and Webster [27] used Sachs boring technique. Parker [28, 29] developed a numerical model to simulate Sach’s method. He found that, the assumption of elastic unloading used in this method was invalidated by the

Bauschinger effect. By neglecting the Bauschinger effect caused 24% and 43% overestimation of residual radial stress and residual hoop stress respectively. Therefore, it was not recommended to use this method for the determination of residual stress.

Non-destructive methods such as X-ray and neutron diffraction were more commonly used methods by the researchers. Ma et al. [30] studied on residual strain profiles for different autofrettage pressures by using neutron diffraction method. Elastic–plastic interfaces were determined and confirmed by using the peak analysis. The study was also simulated in ANSYS APDL and good agreement between the experimental results and finite element results were achieved.

Lee et al. [31] investigated the relationship between residual stress and hardness characteristic of a symmetric and eccentric autofrettaged cylinder. Residual stresses were determined by X-ray diffraction (XRD) peak width analysis and a successful correlation between residual stress and hardness was found.

Jain et al. [32] compared analytical, numerical and experimental results of residual hoop stresses. Test sample made of Al 6082T6 with 14 mm inner, 24 mm outer diameter and 90 mm length was autofrettaged in a hydraulic test set-up. Optimum autofrettage pressure of 195 MPa was used in the tests. This pressure was determined from 2D axisymmetric FEM analyses results for working pressure of 150 MPa. Residual hoop stresses along the radius of the cylinder were measured by using X-Ray diffraction technique. Although the numerical and analytical results closely agreed with each other, there was a significant difference in the experimental results. Experimental value of residual hoop stress at the bore was found 95.8% more than the numerical results.

Venter et al. [33] investigated residual stress–strain states along the thickness of autofrettaged cylinders with neutron diffraction, Sachs' boring and compliance methods. Similar results were obtained for Sachs boring and neutron diffraction methods.

Influence of the pressure holding time on strain generation in hydraulic autofrettage process is studied by Basara et al. [34] Six fuel lines with 8mm x 2.2 mm dimensions made of St 52 steel were exposed to 6 autofrettage pressures ranging from 580 to 680

MPa for 600 seconds. It was found that completion of the plastic deformation due to autofrettage pressure requires much longer period than the assumed several seconds in industrial series production. It was also suggested that instead of keeping the components for a long period at the autofrettage pressure determined, the samples should be autofrettaged at some higher autofrettage pressure for a short period.

Some researchers have also studied the effect of autofrettage on the bursting pressure of the cylinder. Majzoobi et al. [35] investigated the effect of the autofrettage process on pressure capacity of the high pressure cylinders. A series of autofrettage experiments were carried out for different pressures and stages. Two pressures, P_{y1} and P_{y2} were considered as the limit pressures for the autofrettage process and calculated by using Xiaoying and Gangling approach [36]. P_{y1} is the pressure required for the onset of yielding and P_{y2} is the pressure just sufficient to bring the outer surface of the cylinder to yielding. It was observed that there was an increase in the pressure capacity with an increase in the autofrettage pressure from P_{y1} to P_{y2} and any pressure higher than P_{y2} had an inverse effect. It was also found that the flow stress did not change when the autofrettage pressure was lower than the working pressure and there was no influence of repeating the autofrettage process under the same pressure. The experimental work was also simulated by performing axisymmetric analysis using FE code NISA. A close agreement was observed between the pressure P_{y2} calculated from the Xioying and Gangling relation and those obtained from the experiments and numerical simulations.

Seifi et al. [37] studied on the effects of external surface cracks on bursting pressure of autofrettaged cylinders. Two types of specimens made from Al alloy (from series 7000) with 30 mm outer and 20 mm inner diameter and another with 35 mm outer and 25 mm inner diameter were used in the experiments. The autofrettage process was also simulating by using Abacus software. Experimental and numerical results were compared with each other and it was found that the numerical methods could acceptably predict the bursting pressure when the fracture parameter was calculated from the modified equation.

2.4 Optimization Studies on Autofrettage Process

Determination of optimum autofrettage pressure and corresponding radius of elasto-plastic boundary is one of the key factors in the design of thick walled cylinders. There are many studies on this subject in which different variables and optimization techniques are used. Some of these studies are summarized below.

Maleki et al. [38] developed an extension of variable material properties (VMP) method in a spherical vessel to determine the optimum autofrettage. The material behaviour in the VMP model was based on actual material behaviour both in loading and unloading stages and considering variable Bauschinger effect. Radial and hoop residual stress distributions obtained by VMP method were also compared with finite element results and a significant difference in hoop stresses near the inner surface was found.

Varga [39] carried out an optimization study for a cylindrical vessel closed with hemi-spherical ends subjected to hydraulic autofrettage. Based on an analytical procedure, the optimum autofrettage pressure and corresponding elastic-plastic interface radius were obtained from minimization of Von-Misses stress which was developed at the interface due to the working pressure.

Darijani et al. [1] studied the optimal design of hydraulically autofrettaged cylinders based on an elastic-plastic approach considering the Bauschinger effect and the yield criterion of Tresca. Two optimization methods of the hoop and equivalent stresses were used to determine the optimum autofrettage pressure. It was found that the optimum autofrettage pressure was depended on the Bauschinger effect, working pressure and geometric dimensions.

Zhu and Yang [40] studied on the influence of autofrettage on stress distribution and load bearing capacity. They presented an analytical equation for optimum value of elastic-plastic interface for elastic-perfectly material model. Majzoobi and Ghomi [41] determined optimum value of interface radius by using numerical simulations and experiments. The results are then compared with those given by Zhu and Yang [40]. In the optimization problem, the objective function was defined as the weight of compound cylinder. The difference between the results obtained and those given by Zhu and Yang was 6.4% for aluminium and 7.1% for steel, thus, it was concluded that there was no significant difference between elastic perfectly plastic and strain hardening models for prediction of optimum value of elastic-plastic interface.

Hojjati and Hassani [42] stated the optimum autofrettage pressure and radius by theoretically and by finite-element modeling based on von misses yielding criteria. They stated that optimum autofrettage pressure is not a constant and it depends on the working pressure.

Rayhan et al. [43] observed that working pressure and the ratio of outer to inner radius (b/a=k) effects the optimum autofrettage pressure. Table 2.1 represents the effect of working pressure on maximum von misses stress. It is clear that the autofrettage effect is more beneficial at higher working pressure. It is also seen in Table 2.2 that, the autofrettage effect increases with an increase in the thickness of the cylinder wall.

Table 2.1 Effect of working pressure at maximum von mises stress

WP (MPa)	MVMS Without autofrettage (MPa)	MVMS Autofrettaged (MPa)	% Reduction of MVMS
100	225	193	14.22
200	450	348	22.67
300	676	496	26.62
400	840	615	26.78

Table 2.2 Effect of k (b/a) on maximum von mises stress

k	MVMS Without autofrettage (MPa)	MVMS Autofrettaged (MPa)	% Reduction of MVMS
2.0	450	348	22.67
2.5	405	312	22.97
3.0	380	281	26.05

Çandar and Filiz [13] studied on determination of optimum autofrettage pressure for high pressure cylinder of an abrasive waterjet intensifier. The stress analysis was based on an analytical model by using Von Misses yield criterion with bilinear kinematic hardening model. Elasto-plastic radius was considered as the design variable and optimization procedure was implemented in the optimization toolbox available in MATLAB®. For a 160mm long AISI 4340 alloy steel cylinder with 14 mm inner, 24 mm outer diameter, the optimum autofrettage pressure was determined as 936 MPa.

CHAPTER 3

ANALYSIS OF THICK WALLED CYLINDERS

3.1 Introduction

In this chapter, the analysis of thick walled cylinders is presented. Stresses and their distributions on the wall when the cylinder is subjected to inner and outer pressure are analysed first. Development of residual stress at the inner surface by using interference fit is discussed. And the rest of the chapter is devoted to the development of residual stress due to autofrettage process. Expressions for stresses under loading, unloading and working conditions are given.

3.2 Stresses in a Thick Walled Cylinder

Thick walled cylinders are generally used in industries where they are subjected to high pressures. These pressures may be constant or fluctuating between two values. When a thick walled cylinder with closed ends is subjected to an internal or/and external pressure, three types of stresses (radial, σ_r; tangential (hoop), σ_t; and longitudinal (axial), σ_z) are developed [44]. These stresses are principle stresses and their expressions can be derived from the force equilibrium in radial and axial directions.

Consider a thick walled cylinder which is axially symmetric about the z axis and pressurized at $r=r_i$ (P_i) and $r=r_o$ (P_o) as shown in Figure 3.1(a). From the force equilibrium on the infinitesimally small element in the radial direction, expressions for radial and tangential stresses are derived as follows:

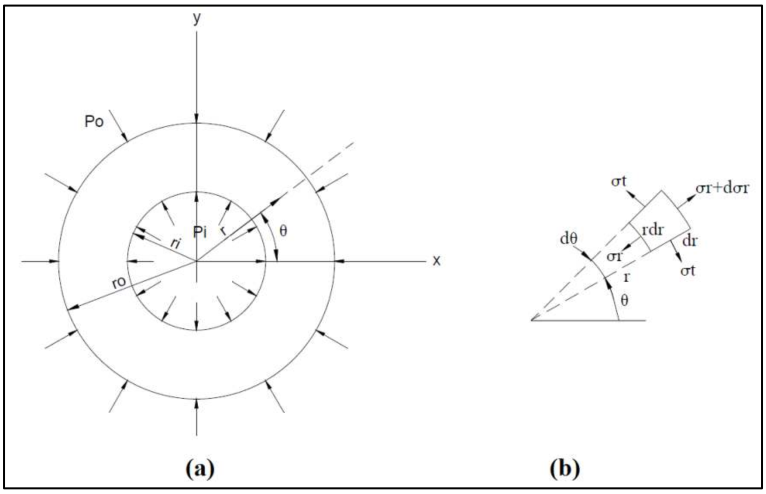

Figure 3.1 Cross section of a thick walled cylinder under internal (Pi) and external (Po) pressure

The forces in the radial direction are obtained from Figure 3.1(b) by multiplying the stresses by their respective areas. Thus;

$$-\sigma_r(rd\theta) + (\sigma_r + d\sigma_r)(r + dr)d\theta - 2\sigma_t \sin\frac{d\theta}{2}dr = 0$$

$$-\sigma_r rd\theta + \sigma_r rd\theta + \sigma_r drd\theta + rd\sigma_r d\theta + d\sigma_r drd\theta - \sigma_t d\theta dr = 0$$

"$d\sigma_r drd\theta$" is very small and can be neglected, and assuming "$\sin\frac{d\theta}{2} \cong \frac{d\theta}{2}$", the equation above reduces to,

$$\sigma_r drd\theta + rd\sigma_r d\theta - \sigma_t d\theta dr = 0$$

$$\sigma_r + r\frac{d\sigma_r}{dr} - \sigma_t = 0 \tag{3.1}$$

Assuming the cylinder is thin in the z direction (plane stresses), $\sigma_z=0$ and the radial and tangential strains are given by Eqs. (3.2) and (3.3);

$$\varepsilon_r = \frac{d\Delta r}{dr} = \frac{1}{E}(\sigma_r - \nu\sigma_t) \tag{3.2}$$

$$\varepsilon_t = \frac{\Delta r}{r} = \frac{1}{E}(\sigma_t - \nu\sigma_r) \tag{3.3}$$

Solving for Δr in Eq. (3.3) and differentiating yields,

$$\frac{d\Delta r}{dr} = \frac{1}{E}\left[r\frac{d\sigma_t}{dr} + \sigma_t - \nu\left(\sigma_r + r\frac{d\sigma_r}{dr}\right)\right] \tag{3.4}$$

Equating Eqs. (3.2) and (3.4) results in,

$$r\frac{d\sigma_t}{dr} - \nu r\frac{d\sigma_r}{dr} + (1+\nu)(\sigma_t - \sigma_r) = 0 \tag{3.5}$$

From Eq. (3.1),

$$\sigma_t = r\frac{d\sigma_r}{dr} + \sigma_r \tag{3.6}$$

Differentiation with respect to r results in,

$$\frac{d\sigma_t}{dr} = r\frac{d^2\sigma_r}{dr^2} + 2\frac{d\sigma_r}{dr} \tag{3.7}$$

Substituting Eqs. (3.6) and (3.7) into Eq.(3.5) yields,

$$r\frac{d^2\sigma_r}{dr^2} + 3\frac{d\sigma_r}{dr} = 0 \tag{3.8}$$

The form of the solution of Eq.(3.8) is $\sigma_r = Cr^n$. Substituting this into Eq.(3.8) yields $n=0$ *and* $n=-2$. Thus the solution is,

$$\sigma_r = C_1 + \frac{C_2}{r^2} \tag{3.9}$$

Substituting this into Eq.(3.6);

$$\sigma_t = C_1 - \frac{C_2}{r^2} \tag{3.10}$$

From Figure 3.1(a), the boundary conditions are,

$$\sigma_r = \begin{cases} -P_i \ at \ r = r_i \\ -P_o \ at \ r = r_o \end{cases}$$

Substituting the boundary conditions into Eq.(3.9) result in,

$$C_1 = \frac{P_i r_i^2 - P_o r_o^2}{r_o^2 - r_i^2} \qquad C_2 = \frac{r_i^2 r_o^2 (P_o - P_i)}{r_o^2 - r_i^2}$$

Substituting the expressions into Eqs.(3.9) and (3.10) produces the final equations for σ_r and σ_t,

$$\sigma_r = P_i\left(\frac{r_i^2}{r_o^2 - r_i^2}\right)\left(1 - \frac{r_o^2}{r^2}\right) - P_o\left(\frac{r_o^2}{r_o^2 - r_i^2}\right)\left(1 - \frac{r_i^2}{r^2}\right) \tag{3.11}$$

$$\sigma_t = P_i\left(\frac{r_i^2}{r_o^2 - r_i^2}\right)\left(1 + \frac{r_o^2}{r^2}\right) - P_o\left(\frac{r_o^2}{r_o^2 - r_i^2}\right)\left(1 + \frac{r_i^2}{r^2}\right) \tag{3.12}$$

These equations are known as Lâme equations [44].

If the outer pressure is zero $(P_o=0)$ then the Eqs. (3.11) and (3.12) reduced to,

$$\sigma_r = P_i \frac{r_i^2}{r_o^2 - r_i^2}\left(1 - \frac{r_o^2}{r^2}\right) \tag{3.13}$$

$$\sigma_t = P_i \frac{r_i^2}{r_o^2 - r_i^2}\left(1 + \frac{r_o^2}{r^2}\right) \tag{3.14}$$

where σ_t is tension and σ_r is compression.

If the internal pressure is zero ($P_i=0$);

$$\sigma_r = -P_o \frac{r_o^2}{r_o^2 - r_i^2}\left(1 - \frac{r_i^2}{r^2}\right) \tag{3.15}$$

$$\sigma_t = -P_o \frac{r_o^2}{r_o^2 - r_i^2}\left(1 + \frac{r_i^2}{r^2}\right) \tag{3.16}$$

In this case both stresses are of compressive types.

When the ends of the cylinder are closed, force equilibrium in axial direction gives the expression for longitudinal stress.

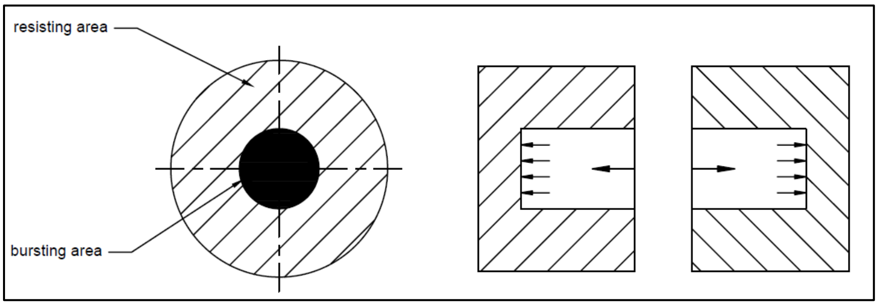

Figure 3.2 Representation of Longitudinal stress

From Figure 3.2,

Bursting force = Resisting force

Bursting force $= F_b = P_i \pi r_i^2$

Resisting force $= F_r = \sigma_l \pi (r_o^2 - r_i^2)$

$F_b = F_r$

$P_i \pi r_i^2 = \sigma_l \pi (r_o^2 - r_i^2)$

Longitudinal stress is found as:

$$\sigma_l = P_i \frac{r_i^2}{r_o^2 - r_i^2} \tag{3.17}$$

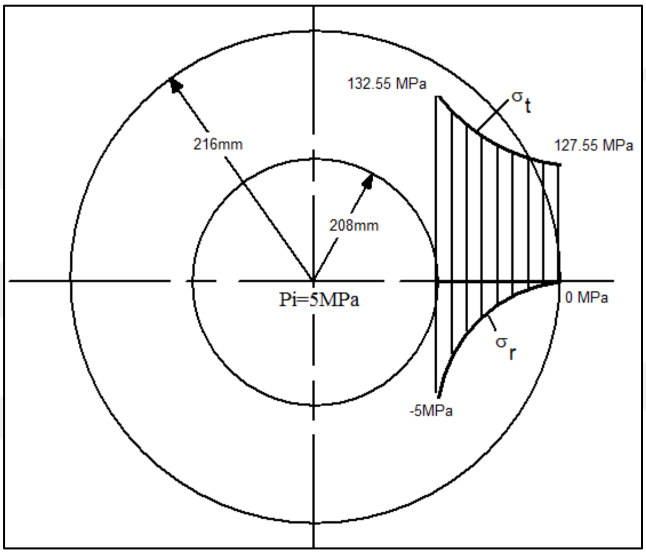

Figure 3.3 Stress distributions for a thick walled cylinder [44] (P_o=0 and both ends are open)

Both tangential (σ_t) and radial (σ_r) stresses are the functions of radial distance, r. Figure 3.3 illustrates distribution of these stresses on the wall of a cylinder (r_i=208 mm and r_o=216 mm) subjected to 5 MPa inner pressure. Tangential stress (σ_t) is maximum at the inner surface. If the stress is of repeated type, alternating component of the Von-Misses stress at this section may cause fatigue failure and the fracture occurs along the length of the cylinder. Images of such a fracture illustrated in Figure 3.4 are obtained by personal communication with an industrialist experienced in thick walled cylinders [45]. This failure had occurred after the application of a repeated pressure of 400 MPa about 24 hours. In order to overcome such a problem and improve the fatigue life of thick walled cylinders, the value of the tangential stress at the inner surface must be decreased. The only way to do this without changing any dimensions of the cylinder is to induce a compressive type of residual stress at the inner wall. Interference fit and autofrettage process are two commonly methods used for this purpose.

Figure 3.4 Failure on a high pressure cylinder of an intensifier pump [45]

3.3 Interference Fit Process

Interference fit is one of the common mechanical methods used to join two cylindrical components with a certain amount of interference to transmit torque (i.e. shaft gear connection) or to create compressive type of residual stress in thick walled cylinders. Interference fit can be obtained by heating and/or cooling the members or by applying a certain amount of force in axial direction. A typical example of interference fit is illustrated in Figure 3.5.

Figure 3.5 Press fitted cannon barrel [46]

After fitting, a certain amount of interface pressure (p) develops between the members as illustrated in Figure 3.6. Interface pressure acts as an external pressure for the inner member and as an internal pressure for the outer member. Lâme equations for each member are written as follows:

- For inner part ($a \leq r \leq b$)

$$\sigma_{ir} = -p \frac{b^2}{b^2 - a^2} \left(1 - \frac{a^2}{r^2}\right) \tag{3.18}$$

$$\sigma_{it} = -p \frac{b^2}{b^2 - a^2} \left(1 + \frac{a^2}{r^2}\right) \tag{3.19}$$

$$\sigma_{il} = -p \left(\frac{b^2}{b^2 - a^2}\right) \tag{3.20}$$

- For outer part ($b \leq r \leq c$)

$$\sigma_{or} = p \frac{b^2}{c^2 - b^2} \left(1 - \frac{c^2}{r^2}\right) \tag{3.21}$$

$$\sigma_{ot} = p \frac{b^2}{c^2 - b^2} \left(1 + \frac{c^2}{r^2}\right) \tag{3.22}$$

$$\sigma_{ol} = p \left(\frac{b^2}{c^2 - b^2}\right) \tag{3.23}$$

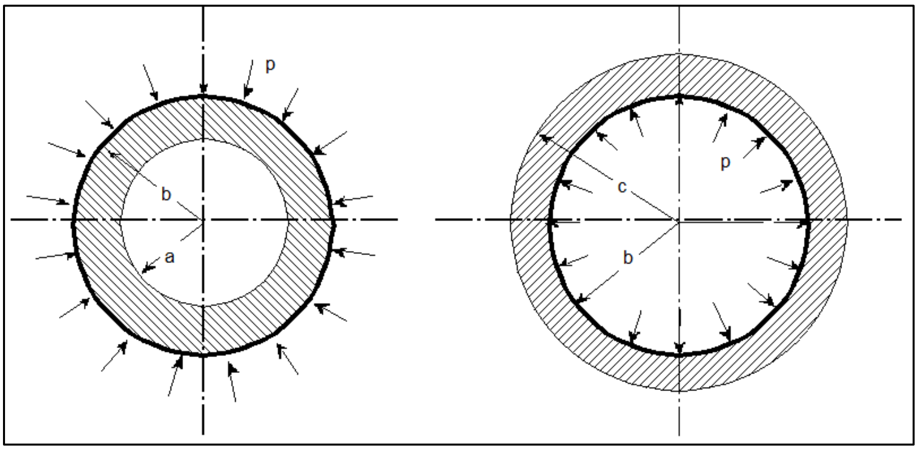

Figure 3.6 Representation of interference pressure for inner and outer member [44]

Radial and tangential stress distributions generated by Topçu and Filiz [10] for interference fit assembly are given in Figures 3.7 and 3.8. The assembly has

14.25mm inner, 24.09mm interface and 38.6mm outer radius which are denoted by "a", "b" and "c" respectively in Figure 3.7.

It is seen from Figure 3.7 that, interference fit provides a useful compressive stress at the inner wall. However, an undesirable tensile stress occurs at the contact surface. Also, discontinuity in the stress distribution at the contact surface is seen as a disadvantage.

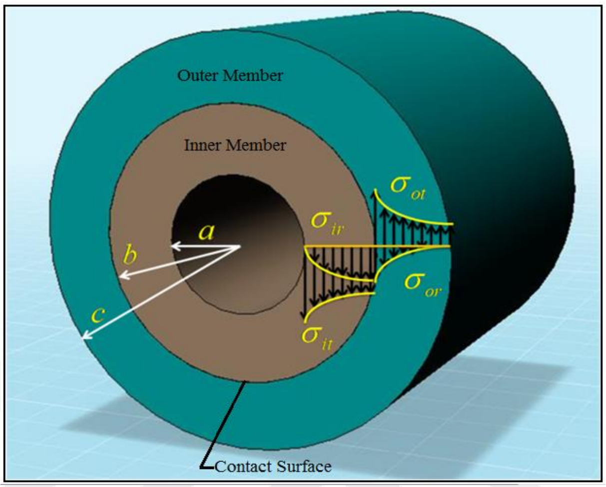

Figure 3.7 Stress distribution in shrink-fitted cylinder [10]

When a shrink-fitted cylinder is subjected to working pressure, the stress distributions in the inner and the outer member change and the new stress distributions are obtained by the sum of residual stresses created in the cylinders and stresses developed in the cylinders due to working pressure. Hence, the stress equations for the inner and the outer member become;

- For inner part ($a \leq r \leq b$)

$$\sigma_{ir} = P_w \frac{a^2}{c^2 - a^2}\left(1 - \frac{c^2}{r^2}\right) - p\frac{b^2}{b^2 - a^2}\left(1 - \frac{a^2}{r^2}\right) \tag{3.24}$$

$$\sigma_{it} = P_w \frac{a^2}{c^2 - a^2}\left(1 + \frac{c^2}{r^2}\right) - p\frac{b^2}{b^2 - a^2}\left(1 + \frac{a^2}{r^2}\right) \tag{3.25}$$

$$\sigma_{il} = P_w \frac{a^2}{c^2 - a^2} - p\left(\frac{b^2}{b^2 - a^2}\right) \tag{3.26}$$

- For outer part ($b \le r \le c$)

$$\sigma_{or} = P_w \frac{a^2}{c^2 - a^2}\left(1 - \frac{c^2}{r^2}\right) + p\frac{b^2}{c^2 - b^2}\left(1 - \frac{c^2}{r^2}\right) \tag{3.27}$$

$$\sigma_{ot} = P_w \frac{a^2}{c^2 - a^2}\left(1 + \frac{c^2}{r^2}\right) + p\frac{b^2}{c^2 - b^2}\left(1 + \frac{c^2}{r^2}\right) \tag{3.28}$$

$$\sigma_{ol} = P_w \frac{a^2}{c^2 - a^2} + p\left(\frac{b^2}{c^2 - b^2}\right) \tag{3.29}$$

where, P_w is the working pressure.

Figure 3.8 shows distribution of the radial and tangential stresses under the working pressure of 410 MPa. It is seen that tangential stress at the inner surface is decreased and the contact surface (interface) becomes the most critical section. For optimum value of interface radius (24.09 mm), maximum Von Misses stress is determined as 563 MPa while it is 822 MPa for a mono-block cylinder [10].

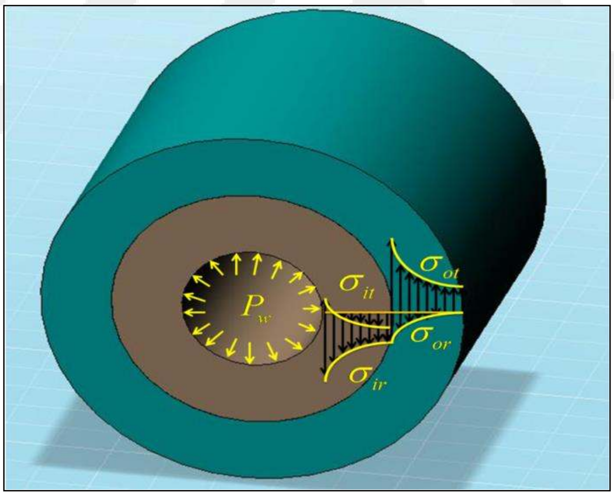

Figure 3.8 Stress distribution of a shrink-fitted cylinder under working pressure [10]

In interference fit applications, the problem is how to determine the amount of interference between inner and outer members. From strength requirement, interface pressure is determined first and then the amount of interference will be calculated. The interface pressure (p) depends on the total amount of interference (δ) which is the sum of deformations experienced by the inner and the outer member ($\delta=\delta_i+\delta_o$) as shown in Figure 3.9. The relationship between the interface pressure and the amount of interference is derived as follows:

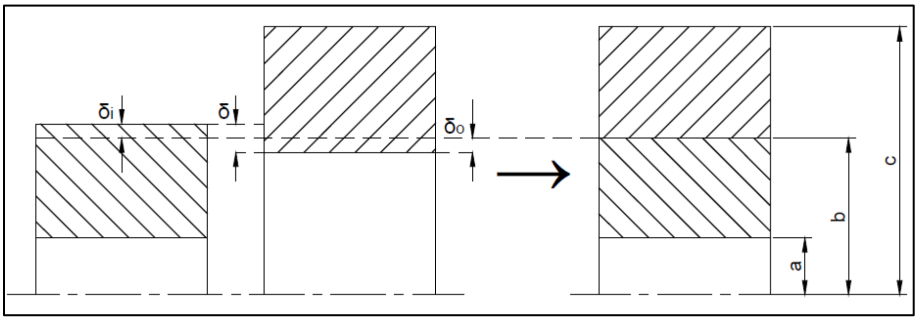

Figure 3.9 Half sectional view of shrink fit assembly

From the circumferential change in the outer member, equation for tangential strain is;

$$\varepsilon_t = \frac{2\pi(b+\delta_o) - 2\pi b}{2\pi b} = \frac{\delta_o}{b} \tag{3.30}$$

Tangential strain also equals to;

$$\varepsilon_t = \frac{\sigma_t}{E_o} - \nu_o \frac{\sigma_r}{E_o} \tag{3.31}$$

Combining Eqs. (3.30) and (3.31) yields;

$$\delta_o = \frac{b}{E_o}(\sigma_t - \nu_o \sigma_r) \tag{3.32}$$

Eqs. (3.13) and (3.14) (Lâme equations) are arranged by giving “b”, “c” and “p” instead of “r_i”, “r_o” and P_i respectively and for r=b as;

$$\sigma_r = -p \tag{3.33}$$

$$\sigma_t = p\frac{b^2 + c^2}{c^2 - b^2} \tag{3.34}$$

Substituting Eqs. (3.33) and (3.34) into Eq. (3.32), deformation experienced by the outer member is found as:

$$\delta_o = \frac{bp}{E_o}\left(\frac{b^2 + c^2}{c^2 - b^2} + \nu_o\right) \tag{3.35}$$

By using similar expressions for the inner member, deformation experienced by the inner member is found as:

$$\delta_i = \frac{bp}{E_i}\left(\frac{b^2 + a^2}{b^2 - a^2} - \nu_i\right) \tag{3.36}$$

where, E is Young's module and v is poison's ratio of the material.

And the total amount of interference is found as:

$$\delta = \frac{bp}{E_o}\left(\frac{b^2 + c^2}{c^2 - b^2} + \nu_o\right) + \frac{bp}{E_i}\left(\frac{b^2 + a^2}{b^2 - a^2} - \nu_i\right) \tag{3.37}$$

If the materials are the same E_o=E_i=E, δ is written as:

$$\delta = \frac{pb}{E}\left[\frac{2b^2 + c^2 - a^2}{(c^2 - b^2)(b^2 - a^2)}\right] \tag{3.38}$$

3.4 Autofrettage Process

Autofrettage process is another method for creating residual stresses on the wall of a thick walled cylinder. It is a metal fabrication technique in which a pressure vessel is subjected to very high pressure, causing internal portions of the part to yield resulting in compressive residual stresses [47].

In this process, a thick walled cylinder is internally pressurized so that the cylinder becomes partially plastic surrounded by elastic region. The pressure is then released and the outer elastic part of the wall attempt to return to its original diameter, thus tries to compress the inner plastic part and causing compressive residual stresses at the inner surface as shown in Figure 3.10. Owing to residual compressive stress at the inner wall, the value of tangential stress due to working pressure decreases. This provides an increase in the fatigue life or pressure carrying capacity of the cylinder.

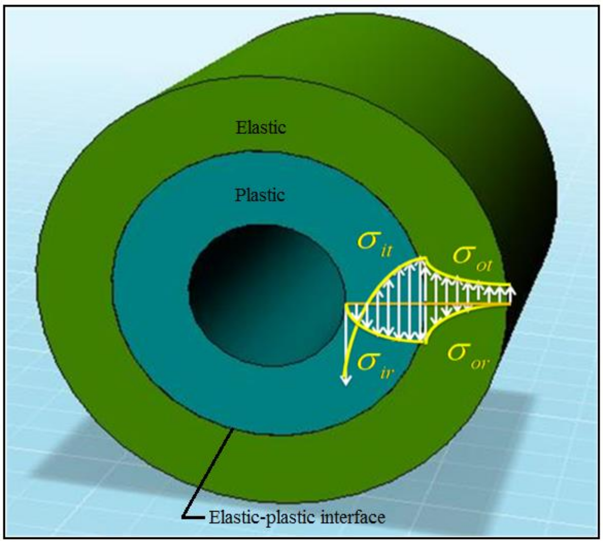

Figure 3.10 Stress distribution of a cylinder after autofrettage process [10]

The autofrettage process was first used by French army for cannon barrels at the beginning of 1900s. Since then, the idea of small, controlled plastic deformations in pressure vessels is widely accepted and greatly reduces the cost of such vessels. Nowadays, the autofrettage method is found to be very favourable to be used in the army as well as many other industrial fields. The method is commonly used in the manufacture of high pressure cylinders of intensifiers, steel pipes, gun and cannon barrels and fuel injection systems [48].

3.4.1 Autofrettage Methods

The conventional autofrettage process involves use of internal hydrostatic pressure to obtain the desired plastic deformation. This method is known as hydraulic process. The autofrettage process is achieved by the pressure effect of pressurizable hydraulic fluid such as ethylene glycol, hydraulic oil, or any similar fluid which will not freeze or solidify at the pressures encountered during the process [49]. Any type of geometries such as fuel rails, fuel injection lines and steel pipes can be easily autofrettaged in a short processing time (2-10s) [15]. However, the autofrettage equipments are very expensive and the method requires substantial capital investment and operating expenditures. Also, there is a limitation of pressure that exceeds 15000 bar [50].

In order to extend the use of autofrettage to higher pressure applications, mechanical autofrettage which is termed as the swaging method has been developed. This process basically consists of passing a swaging tool (mandrel) through the bore of the cylinder as shown in Figure 3.11. Desired permanent enlargement is achieved by the effect of the interface pressure developed between the mandrel and the cylinder. The force required to move the mandrel may be provided by direct hydraulic pressure applied behind the mandrel or by a mechanical loading device [51]. This method offers economic and processing advantages. However, different mandrels produced in extremely close geometrical and dimensional tolerances are required for each autofrettage pressures. Any dimensional error in mandrel size can directly affect the accuracy of the autofrettage process. Also, the method can be only used for straight cylindrical parts, thus its usage area is limited.

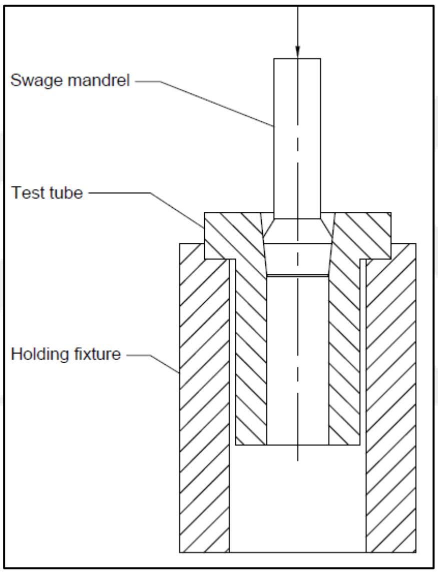

Figure 3.11 Mechanical autofrettage (Swage mandrel) method [19]

In addition to these two methods some new methods such as thermal, rotational, explosive and creep have been developed in recent years. However, there are no commercially available test units for these methods yet and studies about these methods are usually carried out in the research laboratories for low-volume jobs. Among all these methods, hydraulic autofrettage process is the most preferred method due to its distinct advantages mentioned above and selected for the experimental part of this study.

Some patented inventions about autofrettage process are briefly summarized below.

- **Apparatus for Hydraulic Autofrettage**

In this apparatus, a thick walled cylinder to undergo autofrettage is placed between a high pressure cylinder and a closure cylinder and filled with a fluid as shown in Figure 3.12a. Then autofrettage pressure is generated by moving a piston into the interior of the cylinder as shown in Figure 3.12b. Increase in the displacement of the piston inside the cylinder increases the autofrettage pressure [52].

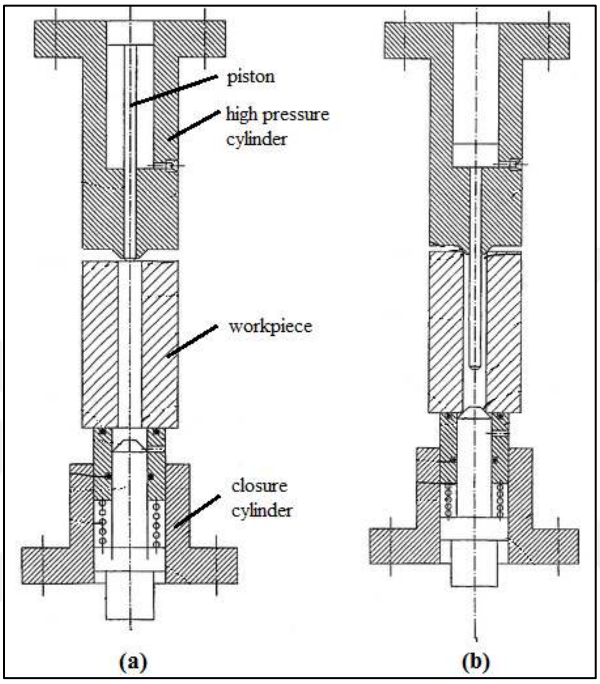

Figure 3.12 Autofrettage apparatus, (a) in an initial position, (b) loading position [52]

- **Compressed Elastomer Autofrettage**

In this method, an expander is placed adjacent to the inner surface of a thick walled cylinder to undergo autofrettage as shown in Figure 3.13. Expander can be made from any material known to those skilled in the art and is preferably made from a material that has a Poisson's ratio is between 0.3 and 0.5 (e.g., rubber’s Poisson’s ratio is almost equal to 0.5 and suitable for using as the expander material). Then the axial compressive force of sufficient magnitude to cause radial expansion of the expander is applied and the necessary pressure for autofrettage process is generated in this way. [53].

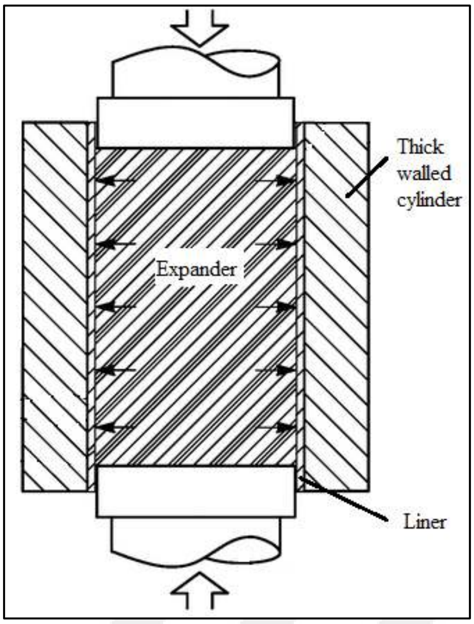

Figure 3.13 Cross sectional view of compressed elastomer autofrettage apparatus [53]

- **Explosive Autofrettage**

In this method, residual compressive stresses near the inner bore of the cylinder is achieved by the means of detonating explosive charges. Rapid burning explosive charges such as "primacord ignitor" are used with an amount of between approximately 1 to 3 grams per inch of length. One particular usage area of this method is the manufacturing of gun barrels; it is also used in the manufacturing of high pressure pipes and forging dies [54].

Figure 3.14 shows basic configuration of explosive autofrettage apparatus. A ductile tube (1) containing explosive charges and covered by a radial piston (2) is placed along the longitudinal axis of the thick walled cylinder (3) which is to be autofrettaged. The radial piston is filled with low detonation velocity explosive powders (4). Ignition of the explosive charges is supplied by the blasting cap lead (5) which is connected to a suitable electric power source. After the explosion, the explosion gases expand the radial piston and the desired residual compressive stress at the bore of the cylinder is obtained. The amount of residual compressive stress induced in the cylinder is basically based on the amount of the explosive charges and the dimensions of the radial piston [54].

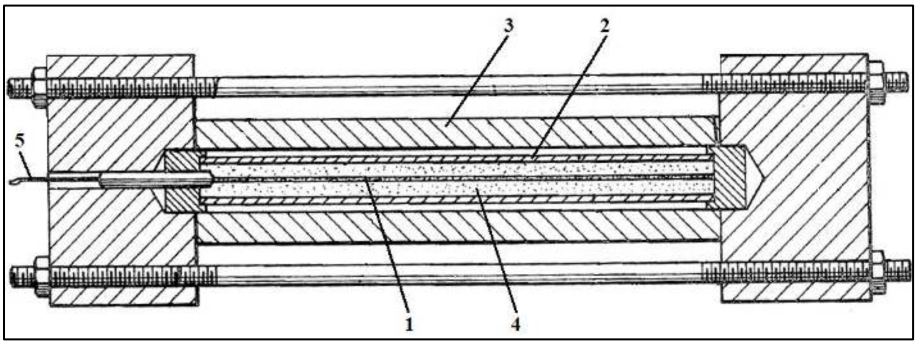

Figure 3.14 Apparatus for explosive autofrettage [54]

- **Creep Autofrettage**

In this method a thick walled cylinder to be autofrettaged is placed in an oven and the cylinder is subjected to both predetermined temperature which allows creep and autofrettage pressure supplied by a suitable pump valve and reservoir arrangement as shown in Figure 3.15. The objective of this invention is to obtain a uniform stress intensity (the maximum difference of the principle stresses at a point in a vessel wall) distribution through the vessel wall for maximum utilization of the vessel material [55].

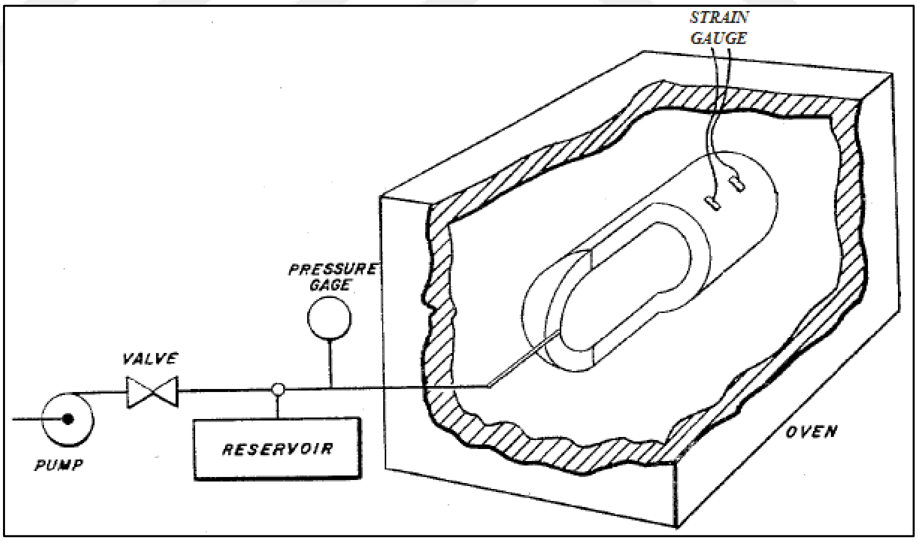

Figure 3.15 Creep Autofrettage [55]

In a plot of creep strain vs. time, creep passes first through a region of primary creep, then a region of secondary creep and finally a region of tertiary creep where the creep rate increases to failure or rupture. In this invention, the autofrettage process is carried out with the application of the parameters of creep sufficient to obtain a primary or secondary creep condition [55].

The autofrettage pressure to be used is calculated from Eq. (3.39), where "p_2" is the design pressure (the working pressure for maximum utilization from the autofrettage process) and "n" is the creep exponent (or stress exponent). Creep exponent may be simply determined from the slope of creep rate (percent/hr.) vs. stress on a logarithmic plot. There are also some sources give tabulated values of "n".

$$p_1 = p_2 \frac{n}{n-1} \tag{3.39}$$

If the ratio of inner radius to outer radius (R_i) is known the design pressure (p_2) is then calculated or vice versa from the following equation:

$$p_2 = 1/2 S_d (n)^{\frac{n}{n-1}} \left(R_i^{-2} - 1\right)^{\frac{-1}{n-1}} \left(R_i^{\frac{-2}{n}} - 1\right)^{\frac{n}{n-1}} \tag{3.40}$$

where, S_d, is the material design stress intensity and obtained from ASME Boiler and Pressure Vessel Code. For standard materials $S_d = 2/3 S_y$ and for non-standard materials $S_d < 2/3 S_y$ or $S_d = 1/2 S_u$, where S_y and S_u are yield strength and ultimate strength of the material respectively [55].

3.4.2 Benefits of Autofrettage Process

There are numbers of benefits of autofrettage process. The major benefit is that the pressure could be held by the autofrettaged components without failure (working pressure) increases up to 2 times higher or more [50]. Conversely, the service life of the component can be increased or wall thickness of the cylinder can be reduced or cheaper materials with lower strengths can be used for the same working pressure. The other benefits provided from the autofrettage process are as follows:

- In most cases, there is no crack formation in the autofrettaged cylinders due to the lower tensile stress at the bore. If there is an already developed crack on the cylinder wall, progressing of the crack may be prevented [50].
- The autofrettage process minimizes the effect of poor surface finish on fatigue life. It provides a simple and cost-effective solution to improve the surface finish of the inner bore of the cylinder which is very costly in the other commercial processes. Also, unavoidable design features can be successfully eliminated [48].
- The notch sensitivity is significantly reduced [50].

3.5 Theoretical Analysis of Autofrettage Process

Analysis of autofrettage process had received considerable attention of many researchers. Owing to different assumptions that they have used, many analytical autofrettage models have been proposed. In this section, some comments on validity and significance of the possible assumptions are presented and an analytical autofrettage model is developed based on these assumptions.

3.5.1 Fundamental Assumptions

3.5.1.1 Stress-strain relationship

In the autofrettage process, material behaviour during loading and unloading stages exhibits great importance in the analysis of residual stresses. The basic autofrettage theory proposed by Hill [9] assumes elastic–perfectly plastic behaviour for the material, as shown in Figure 3.16. This assumption still is being used in the analyses where thick walled cylinders exhibit very little strain hardening in the plastic region and reverse yielding is not under consideration.

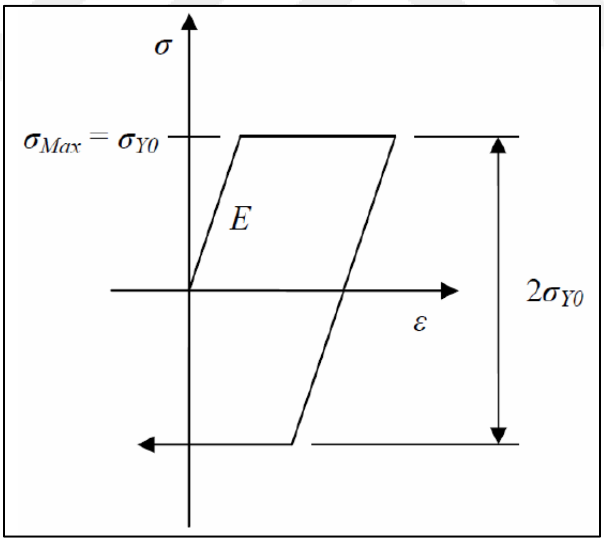

Figure 3.16 Stress-strain diagram of an elastic–perfectly plastic material [56]

There are two important phenomena in the stress-strain relationship of the material that accompany the autofrettage process. The first phenomenon is strain hardening (work hardening). In the plastic region, the load increases with further strain. This effect of the material being able to withstand a greater load despite the uniform reduction in cross sectional area is known as strain-hardening. Strain hardening causes the yield strength of the material to change. The second phenomenon is the

Bauschinger effect. In 1881, J.Bauschinger discovers realizing on a metal, compression test resulting after a first plastic deformation of tensile test, a decrease in the yield stress [57]. Since that day, this is known as Bauschinger effect. Figure 3.17 clearly demonstrates the Bauschinger-effect. Originally, the elastic tensile yield strength is equal to the compressive yield strength (OA=OF or $\sigma_{yt} = \sigma_{yc}$). When the load is increased to point (B) beyond the elastic limit and then removed, the tensile strength will increase (BC); however, the compressive yield strength will decrease to σ'_{yc}, [58]. This unexpected situation is caused by the uneven dislocation distribution of plastically deformed metals [59].

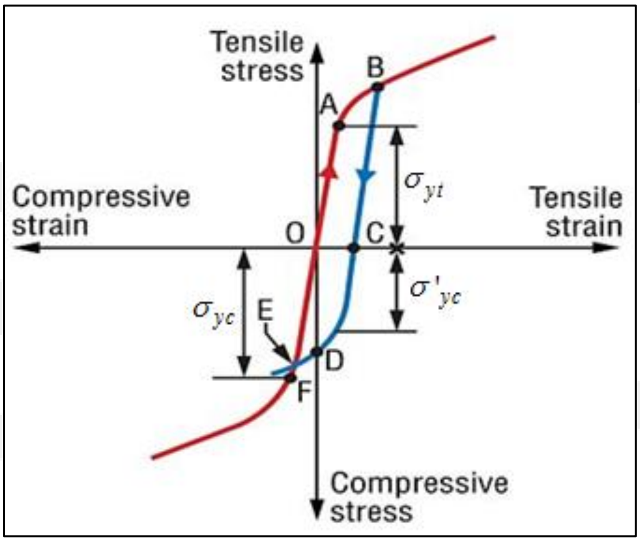

Figure 3.17 Bauschinger effect [58]

The ratio of compressive yield strength to tensile yield strength is defined as Bauschinger effect coefficient ($b_{ef} = \sigma'_{yc}/\sigma_{yt}$) [12]. In general, Bauschinger effect coefficient, b_{ef} is found to be material dependent and sensitive to the amount of prior plastic strain. Typical values of b_{ef} are in the range of 0.3–1.0 [11]. The smaller Bauschinger effect coefficient causes the reverse yielding to take place more easily and affects the residual stress distribution.

Owing to the strain-hardening and Bauschinger effect, most materials do not satisfy the elastic–perfectly plastic assumption, and consequently alternative autofrettage models, based on various simplified material strain hardening characteristics, have been proposed. Isotropic and kinematic hardening models are the most commonly used models [12].

Isotropic hardening is generally considered to be a suitable model for large plastic flows. It implies that the yield strength in tension and compression are the same. Kinematic hardening is the simplest theory that can model the Bauschinger effect. Typical uniaxial isotropic and kinematic hardening curves are shown in Figure 3.18. If unloading does not occur, there is no difference between these two models. For unloading with reverse yielding, the results based on these two models will be different. [18].

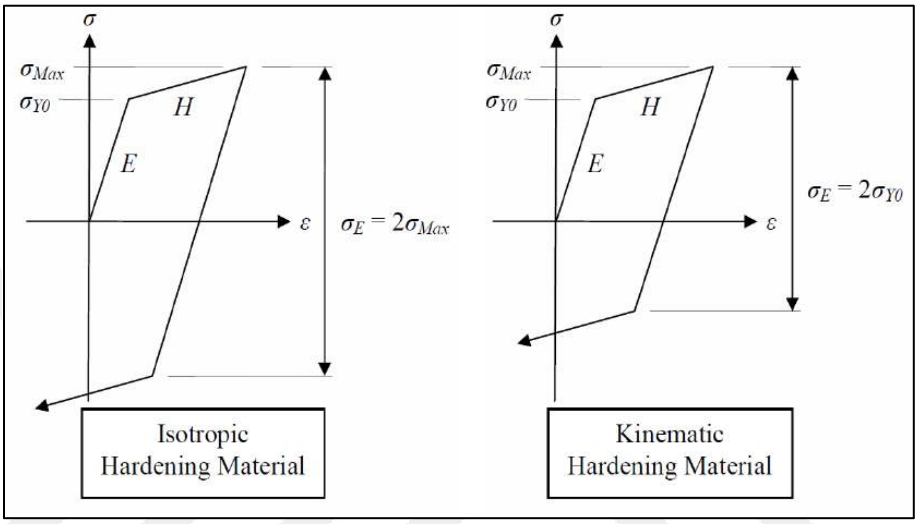

Figure 3.18 Kinematic and Isotropic hardening models [60]

In addition to these models, Huang [] proposed a general autofrettage model based on the actual stress-strain curve of the material and by considering the Bauschinger effect.

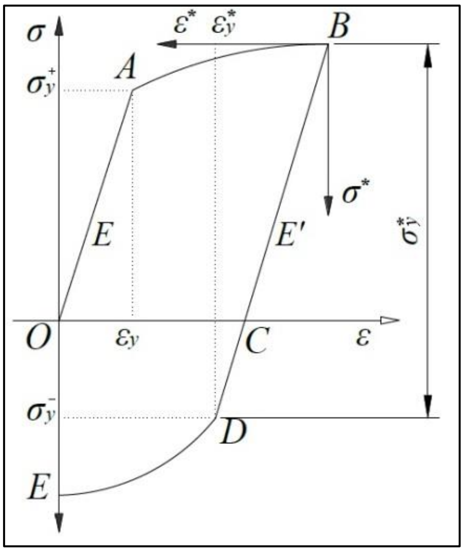

Figure 3.19 General material tensile-compressive stress-strain curve for Huang's model[12]

In this model, tensile-compressive stress-strain curve is divided into four segments as O-A, A-B, B-D and D-E where O-A-B and B-D-E refer to loading and unloading phases respectively as shown in Figure 3.19. The relationship for each segment can be expressed as

O-A (Linear elastic region-loading phase):

$$\sigma = E\varepsilon \quad (\varepsilon \leq \varepsilon_y) \tag{3.41}$$

A-B (Strain hardening region-loading phase):

$$\sigma = A_1 + A_2\varepsilon^{B_1} \quad (\varepsilon \geq \varepsilon_y) \tag{3.42}$$

B-D (Linear elastic region-unloading phase):

$$\sigma^* = E'\varepsilon^* \quad (\varepsilon^* \leq \varepsilon_y{}^*) \tag{3.43}$$

D-E (Strain hardening region-unloading phase):

$$\sigma = A_3 + A_4(\varepsilon^*)^{B_2} \quad (\varepsilon^* \geq \varepsilon_y{}^*) \tag{3.44}$$

where, A_1, A_2, A_3, A_4, B_1 and B_2 are constant terms and they are different for each material. They can be determined from the stress-strain curve of the material by using curve fitting methods.

In the theoretical analysis of the autofrettage process, Eqs. (3.41) and (3.42) are used in the derivation of stress equations for loading stage. If there is reverse yielding, the cylinder is considered to consist of three distinct areas as illustrated in Figure 3.20 as elastic loading-elastic unloading zone ($r_c \leq r \leq r_o$), plastic loading-elastic unloading zone ($r_d \leq r \leq r_c$) and plastic loading-plastic unloading zone ($r_i \leq r \leq r_d$) and in addition to Eqs. (3.41) and (3.42), Eqs. (3.43) and (3.44) are used in the derivation of stress equations. If there is no reverse yielding, the unloading will be considered as elastic and the residual stress equations will be obtained by subtracting Lâme equations from loading stress equations. Since the autofrettage pressure values for the experiments are selected so that there will be no reverse yielding in this thesis, the first case is not taking into consideration in the stress analysis section.

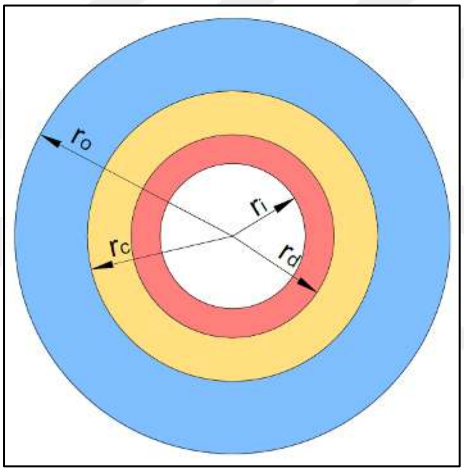

Figure 3.20 Radii of elastic-plastic zones

Huang's model is a general model and can replace the other models mentioned above. Since it uses the actual stress-strain curve of the material, it has a very strong curve fitting ability which is resulted in more realistic and accurate results.

3.5.1.2 Yield criteria

There have been a number of yield criteria proposed over the years. Among these criteria, only the Tresca and Von-Mises criteria predict the behaviour of moderately ductile steel with any degree of accuracy, as would normally be used in a pressure vessel. Although the application of Tresca yield criteria to the thick-walled cylinder problem results in comparatively simple mathematical formulation, Von-Misses criterion has been shown to be the most accurate for all combinations of triaxial stress and should be used wherever possible [61].

The Tresca yield criterion: The Tresca yield criterion (maximum-shear-stress theory) predicts that yielding begins whenever the maximum shear stress in any element equals or exceeds the maximum shear stress in a tension test specimen of the same material when that specimen begins to yield [62].

If the principle stresses are arranged as $\sigma_1 > \sigma_2 > \sigma_3$ and S_y is the maximum shear stress in a tensile test specimen at the yield point then the maximum shear stress is:

$$\tau_{max} = \frac{\sigma_1 - \sigma_3}{2} = \frac{S_y}{2} = S_{sy} \tag{3.45}$$

where, S_{sy} is the yield strength in shear and yielding occurs when $\tau_{max} \geq S_{sy}$

The Von Mises yield criterion: This theory was introduced by Von Mises and it was later suggested by Hencky, therefore this theory is also known as Von Misses Hencky theory.

Von Mises criterion states that yielding will occur when the distortion energy in a unit volume equals to the distortion energy in a unit volume when uniaxially stressed to the yield strength [44].

For a three-dimensional system, effective stress or Von Misses stress and effective strain in the plastic region (assuming that poison's ratio (ν) is 0.5) are calculated from the following equations:

$$\sigma' = \sqrt{\frac{1}{2}[(\sigma_1 - \sigma_2)^2 + (\sigma_2 - \sigma_3)^2 + (\sigma_3 - \sigma_1)^2]} \tag{3.46}$$

$$\varepsilon' = \frac{\sqrt{2}}{3}\sqrt{[(\varepsilon_1 - \varepsilon_2)^2 + (\varepsilon_2 - \varepsilon_3)^2 + (\varepsilon_3 - \varepsilon_1)^2]} \tag{3.47}$$

And yielding occurs when $\sigma' \geq S_y$

These two theories are represented in Figure 3.21 for biaxial stress state (σ_3=0). Any point lies within the area bounded with the lines (or curve) of failure theories, would be considered to be safe. Since the Tresca thory is on or within the boundary of the Von Mises theory, it will always predict a factor of safety equal to or less than the Von Mises theory. For each case, the Tresca theory gives more conservative results compared to Von Mises theory. Also the Von Mises agrees well with all data for ductile behaviour.

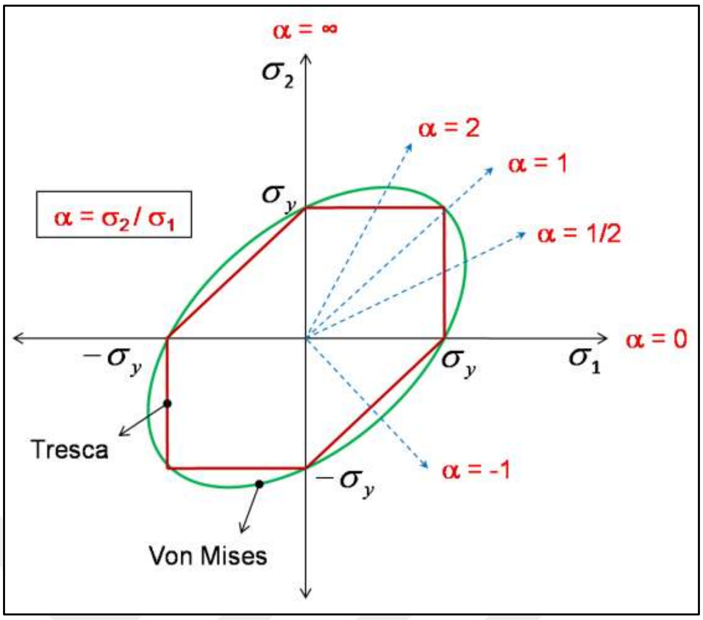

Figure 3.21 Yield boundaries of Tresca and Von Mises criteria for plane stress [62]

3.5.1.3 End condition

Thick walled cylinders may be autofrettaged in open (i.e. swage method) and closed end (i.e. hydraulic autofrettage) conditions. In practice, the restrained end condition does not exist. However, as the assumption associated with the restrained end condition (i.e., ε_z=0) provides a significant simplification of the mathematics and it is often used to obtain approximate solutions [61].

3.5.1.4 Longitudinal Stress-Strain Distributions

Distribution of the longitudinal stress along the wall of the cylinder is uniform for the elastic deformation as seen in the Lâme equations. However, when the cylinder becomes partially plastic, the difference in Poisson's ratio (ν) between the elastic and plastic zones may result in a variation in the longitudinal stress. In order to determine this stress distribution, some plastic stress-strain law must be used in the plastic zone which may result in considerable mathematical difficulties. To avoid this, many researchers assumed a uniform longitudinal stress either in the elastic region or throughout the wall. On the other hand, assuming a significant variation in longitudinal strain in a long cylinder may result in a considerable variation in the change of overall length. This would produce distortions of the end surfaces of the cylinder which have not been observed in actual practice. Therefore, the longitudinal strain is generally assumed as either constant or zero (for plane strain assumption) along the wall of the cylinder [61].

3.5.1.5 Compressibility

The assumption of compressible material in the elastic region and incompressibility in the plastic region would appear to give a better approximation. However, this may results in a discontinuity at the elastic-plastic interface. Since continuity at the interface is usually a required boundary condition for the modelling of autofrettage process, this assumption is not generally used.

Material may be assumed as incompressible ($\sigma_r+\sigma_\theta+\sigma_z=0$) in both elastic and plastic regions. This may result in some errors when there is a considerable volume change associated with elastic strains and as the elastic strains are significant parts of the total strain in a partially plastic cylinder. It was shown that autofrettage models based on this assumption provided results in fair agreement with experimental results.

3.5.1.6 Unique Curve Assumption

Unique curve assumption is used in some analytical models (i.e., Huang's model) for the autofrettage process. This assumption states that the relationship between the equivalent stress and the equivalent strain under biaxial or triaxial stress states is the same as the stress-strain relationship of a material which is obtained from a tensile test.

3.5.2 Stress Analysis

Stresses developed in the loading, unloading and operating (working) stages of autofrettage process are analysed by using proper boundary conditions and assumptions which are mentioned above. Basic equations are obtained by assuming plane strain and Von-Misses yield criterion. Huang's model is used to simulate stress-strain behaviour of the material and the material is assumed as incompressible in both elastic and plastic regions. Additionally, uniform longitudinal stress-strain distributions are assumed along the wall of the cylinder.

Residual stress distribution is obtained for elastic unloading (no reverse yielding) case. Stresses in the operating stage are considered to be superposition of residual stresses and the elastic stresses due to the operating pressure.

3.5.2.1 Basic Equations

As it was stated in Section 3.2, when an internal pressure is applied to a thick walled cylinder with closed ends radial stress (σ_r), tangential stress (hoop stress, σ_t) and longitudinal stress (σ_z) are developed. These stresses are the principal stresses. From the force equilibrium on the infinitesimally small element, Eq. (3) is obtained and corresponding strains ε_r and ε_θ are written in terms of the radial displacement, u, as:

$$\varepsilon_r = \frac{du}{dr}$$

$$\varepsilon_\theta = \frac{u}{r} \tag{3.48}$$

and the elastic constitutive relations are;

$$E\varepsilon_r = \sigma_r - \upsilon(\sigma_\theta + \sigma_z)$$

$$E\varepsilon_\theta = \sigma_\theta - \upsilon(\sigma_r + \sigma_z)$$

$$E\varepsilon_z = \sigma_z - \upsilon(\sigma_r + \sigma_\theta) \tag{3.49}$$

For plain strain assumption, ε_z=0, Eq. (3.49) gives;

$$\sigma_z = \frac{1}{2}(\sigma_\theta + \sigma_r) \tag{3.50}$$

By combining Von Mises yield condition as substituting Eq. (3.50) into Eq. (3.46) gives;

$$\sigma_\theta = \frac{2}{\sqrt{3}}\sigma' + \sigma_r \tag{3.51}$$

$$\sigma_z = \frac{1}{\sqrt{3}}\sigma' + \sigma_r \tag{3.52}$$

The radial stress σ_r can be obtained from Eqs. (3.1) and (3.51);

$$\sigma_r = \int \frac{2}{\sqrt{3}} \frac{\sigma'}{r} dr \qquad (3.53)$$

Equivalent strain *ε'* can be obtained by using plane strain and incompressible volume assumptions as follows;

$$\varepsilon_\theta + \varepsilon_r + \varepsilon_z = 0$$

$$\frac{u}{r} + \frac{du}{dr} + 0 = 0$$

$$\int \frac{1}{r} dr = -\int \frac{1}{u} du$$

$$lnr + lnu = lnc \quad \Rightarrow \quad u = c/r$$

$$\varepsilon_\theta = \frac{u}{r} = \frac{c}{r^2} \qquad (3.54)$$

$$\varepsilon_r = \frac{du}{dr} = -\frac{c}{r^2} \qquad (3.55)$$

where, ε_θ and ε_r are the maximum and the minimum principle strains respectively.

Substituting Eqs. (3.54) and (3.55) into Eq. (3.47);

$$\varepsilon' = \frac{2}{\sqrt{3}} \frac{c}{r^2} \qquad (3.56)$$

where, c is an integration constant.

3.5.2.2 Loading stage

Stress equations for loading stage are obtained for elastic and plastic regions separately by combining stress-strain relation with the basic equations derived above. Boundary conditions are applied to determine the integral constants.

(a) Elastic region

Substituting Eqs. (3.56) and (3.41) into Eq. (3.53) gives

$$\sigma_{re} = -\frac{2}{3} \frac{E}{r^2} c_{e1} + c_{e2} \qquad (3.57)$$

Substituting Eqs. (3.56), (3.41) and (3.57) into Eq. (3.51) gives

$$\sigma_{\theta e} = \frac{2}{3}\frac{E}{r^2}c_{e1} + c_{e2} \tag{3.58}$$

Substituting Eqs. (3.56), (3.41) and (3.57) into Eq. (3.52) gives

$$\sigma_{ze} = c_{e2} \tag{3.59}$$

(b) Plastic region (A-B)

Substituting Eqs. (3.56) and (3.42) into Eq. (3.53) gives

$$\sigma_{rp} = \frac{2}{\sqrt{3}}A_1 \ln r - \frac{A_2}{\sqrt{3}B}\left(\frac{2c_{p1}}{\sqrt{3}r^2}\right)^B + c_{p2} \tag{3.60}$$

Substituting Eqs. (3.56) and (3.42) and (3.57) into Eq. (3.51) gives

$$\sigma_{\theta p} = \frac{2}{\sqrt{3}}A_1(1 + lnr) + \frac{A_2}{\sqrt{3}}\left(\frac{2c_{p1}}{\sqrt{3}r^2}\right)^B\left(2 - \frac{1}{B}\right) + c_{p2} \tag{3.61}$$

Substituting Eqs. (3.56) and (3.42) and (3.57) into Eq. (3.52) gives

$$\sigma_{zp} = \frac{1}{\sqrt{3}}A_1(1 + 2lnr) + \frac{A_2}{\sqrt{3}}\left(\frac{2c_{p1}}{\sqrt{3}r^2}\right)^B\left(1 - \frac{1}{B}\right) + c_{p2} \tag{3.62}$$

Boundary conditions

The following boundary conditions exist when the cylinder is subjected to internal pressure P_a as shown in Figure 3.22.

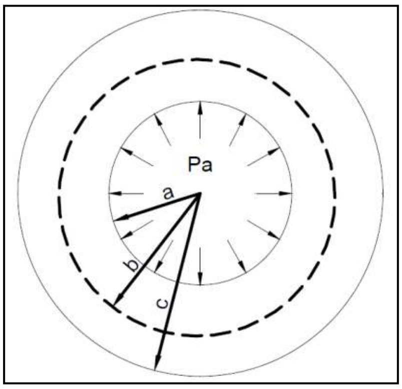

Figure 3.22 Radii of elastic and plastic zones

1 Both of the equivalent stresses in the elastic zone and plastic zone (r=b) are equal the yield strength of the material.

(a) at r=b, $\sigma'_e = S_y$, c_{e1} is found as;

$$c_{e1} = \frac{\sqrt{3}}{2}\frac{S_y}{E}b^2 \tag{3.63}$$

(b) at r=b, $\sigma'_p = S_y$, c_{p1} is found as;

$$c_{p1} = \frac{\sqrt{3}}{2}\left(\frac{(S_y - A_1)}{A_2}\right)^{1/B} b^2 \tag{3.64}$$

2 The radial stress σ_r at the outer surface (r=c) and the inner surface (r=a) are equal to zero and $-P_a$ (autofrettage pressure) respectively.

(a) at r=c, $\sigma_{re} = 0$, c_{e2} is found as;

$$c_{e2} = \frac{1}{\sqrt{3}}S_y\frac{b^2}{c^2} \tag{3.65}$$

(b) at r=a, $\sigma_{rp} = -P_a$, c_{p2} is found as;

$$c_{p2} = -\frac{2}{\sqrt{3}}A_1 \ln a + \frac{(S_y - A_1)}{\sqrt{3}B}\left(\frac{b}{a}\right)^{2B} - P_a \tag{3.66}$$

Loading stress distribution

(a) Elastic region

Substituting Eqs. (3.63) and (3.65) into Eqs. (3.57) to (3.59) gives;

$$\sigma_{re} = \frac{1}{\sqrt{3}}S_y b^2\left(\frac{1}{c^2} - \frac{1}{r^2}\right) \tag{3.67}$$

$$\sigma_{\theta e} = \frac{1}{\sqrt{3}}S_y b^2\left(\frac{1}{c^2} + \frac{1}{r^2}\right) \tag{3.68}$$

$$\sigma_{ze} = \frac{1}{\sqrt{3}}S_y\frac{b^2}{c^2} \tag{3.69}$$

(b) Plastic region

Substituting Eqs. (3.64) and (3.66) into Eqs. (3.60) to (3.62) gives;

$$\sigma_{rp} = \frac{2}{\sqrt{3}}A_1 \ln\frac{r}{a} + \frac{(S_y - A_1)}{\sqrt{3}B}b^{2B}\left(\frac{1}{a^{2B}} - \frac{1}{r^{2B}}\right) - P_a \tag{3.70}$$

$$\sigma_{\theta p} = \frac{2}{\sqrt{3}}\left[ln\left(\frac{r}{a}\right) + 1\right]A_1 + \frac{(S_y - A_1)}{\sqrt{3}B}b^{2B}\left[\frac{1}{a^{2B}} + (2B-1)\frac{1}{r^{2B}}\right] - P_a \tag{3.71}$$

$$\sigma_{zp} = \frac{1}{\sqrt{3}}\left[2ln\left(\frac{r}{a}\right) + 1\right]A_1 + \frac{(S_y - A_1)}{\sqrt{3}B}b^{2B}\left[\frac{1}{a^{2B}} + \frac{(B-1)}{r^{2B}}\right] - P_a \tag{3.72}$$

3.5.2.3 Unloading stage

When the autofrettage pressure is totally removed, the unloading will be elastic and unloading stresses follow the Lâme equations. As a result, residual stresses developed in elastic and plastic parts of the cylinder are calculated as;

(a) Residual stresses developed in elastic part of the cylinder (b≤r≤c)

$$\sigma_{re} = \frac{1}{\sqrt{3}}S_y b^2\left(\frac{1}{c^2} - \frac{1}{r^2}\right) - P_a\frac{a^2}{c^2 - a^2}\left(1 - \frac{c^2}{r^2}\right) \tag{3.73}$$

$$\sigma_{\theta e} = \frac{1}{\sqrt{3}}S_y b^2\left(\frac{1}{c^2} + \frac{1}{r^2}\right) - P_a\frac{a^2}{c^2 - a^2}\left(1 + \frac{c^2}{r^2}\right) \tag{3.74}$$

$$\sigma_{ze} = \frac{1}{\sqrt{3}}S_y\frac{b^2}{c^2} - P_a\frac{a^2}{c^2 - a^2} \tag{3.75}$$

(b) Residual stresses developed in plastic part of the cylinder (a≤r≤b)

$$\sigma_{rp} = \frac{2}{\sqrt{3}}A_1 \ln\frac{r}{a} + \frac{(S_y - A_1)}{\sqrt{3}B}b^{2B}\left(\frac{1}{a^{2B}} - \frac{1}{r^{2B}}\right) - P_a - P_a\frac{a^2}{c^2 - a^2}\left(1 - \frac{c^2}{r^2}\right) \tag{3.76}$$

$$\begin{aligned}\sigma_{\theta p} = {} & \frac{2}{\sqrt{3}}\left[ln\left(\frac{r}{a}\right) + 1\right]A_1 + \frac{(S_y - A_1)}{\sqrt{3}B}b^{2B}\left[\frac{1}{a^{2B}} + (2B-1)\frac{1}{r^{2B}}\right] - P_a \\ & - P_a\frac{a^2}{c^2 - a^2}\left(1 + \frac{c^2}{r^2}\right)\end{aligned} \tag{3.77}$$

$$\sigma_{zp} = \frac{1}{\sqrt{3}}\left[2ln\left(\frac{r}{a}\right) + 1\right]A_1 + \frac{(S_y - A_1)}{\sqrt{3}B}b^{2B}\left[\frac{1}{a^{2B}} + \frac{(B-1)}{r^{2B}}\right] - P_a - P_a\frac{a^2}{c^2 - a^2} \tag{3.78}$$

3.5.2.4 Operating Stage

When the operating (working) pressure is acting, the stresses developed in the cylinder will be reduced due to compressive residual stresses developed at the inner surface of the cylinder.

(a) Stresses developed in elastic part of the cylinder under operating pressure (b≤r≤c)

$$\sigma_{re} = \frac{1}{\sqrt{3}} S_y b^2 \left(\frac{1}{c^2} - \frac{1}{r^2}\right) - P_a \frac{a^2}{c^2 - a^2}\left(1 - \frac{c^2}{r^2}\right) + P_w \frac{a^2}{c^2 - a^2}\left(1 - \frac{c^2}{r^2}\right) \tag{3.79}$$

$$\sigma_{\theta e} = \frac{1}{\sqrt{3}} S_y b^2 \left(\frac{1}{c^2} + \frac{1}{r^2}\right) - P_a \frac{a^2}{c^2 - a^2}\left(1 + \frac{c^2}{r^2}\right) + P_w \frac{a^2}{c^2 - a^2}\left(1 + \frac{c^2}{r^2}\right) \tag{3.80}$$

$$\sigma_{ze} = \frac{1}{\sqrt{3}} S_y \frac{b^2}{c^2} - P_a \frac{a^2}{c^2 - a^2} + P_w \frac{a^2}{c^2 - a^2} \tag{3.81}$$

(b) Stresses developed in plastic part of the cylinder under operating pressure (a≤r≤b)

$$\begin{aligned}\sigma_{rp} = {} & \frac{2}{\sqrt{3}} A_1 \ln\frac{r}{a} + \frac{(S_y - A_1)}{\sqrt{3}B} b^{2B}\left(\frac{1}{a^{2B}} - \frac{1}{r^{2B}}\right) - P_a - P_a \frac{a^2}{c^2 - a^2}\left(1 - \frac{c^2}{r^2}\right) \\ & + P_w \frac{a^2}{c^2 - a^2}\left(1 - \frac{c^2}{r^2}\right)\end{aligned} \tag{3.82}$$

$$\begin{aligned}\sigma_{\theta p} = {} & \frac{2}{\sqrt{3}}\left[ln\left(\frac{r}{a}\right) + 1\right] A_1 + \frac{(S_y - A_1)}{\sqrt{3}B} b^{2B}\left[\frac{1}{a^{2B}} + (2B - 1)\frac{1}{r^{2B}}\right] - P_a \\ & - P_a \frac{a^2}{c^2 - a^2}\left(1 + \frac{c^2}{r^2}\right) + P_w \frac{a^2}{c^2 - a^2}\left(1 + \frac{c^2}{r^2}\right)\end{aligned} \tag{3.83}$$

$$\begin{aligned}\sigma_{zp} = {} & \frac{1}{\sqrt{3}}\left[2ln\left(\frac{r}{a}\right) + 1\right] A_1 + \frac{(S_y - A_1)}{\sqrt{3}B} b^{2B}\left[\frac{1}{a^{2B}} + \frac{(B - 1)}{r^{2B}}\right] - P_a - P_a \frac{a^2}{c^2 - a^2} \\ & + P_w \frac{a^2}{c^2 - a^2}\end{aligned} \tag{3.84}$$

3.5.2.5 Autofrettage Pressure

The autofrettage pressure can be obtained by equating radial stress components at elastic plastic interface (r=b). That is:

$$\sigma_{re} = \sigma_{rp} \quad (at\ r = b)$$

$$P_a = \frac{2}{\sqrt{3}} A_1 ln\left(\frac{b}{a}\right) + \frac{S_y - A_1}{\sqrt{3}B}\left[\left(\frac{b}{a}\right)^{2B} - 1\right] - \frac{Sy}{\sqrt{3}}\left[\left(\frac{b}{c}\right)^{2} - 1\right] \tag{3.85}$$

This expression may be used for the reasonable determination of autofrettage pressures.

In the autofrettage tests performed in this study, the hydraulic test unit creates a clamping force in the axial direction to prevent any leakage problem during the tests. This loading condition does not fit exactly with the analytical model derived above. Therefore, the formulas are only used for a rough estimation of the values of the lower and the upper limits of the autofrettage pressures for the experimental study and to verify some assumptions and parameters such as element type and size used in the numerical model.

CHAPTER 4

EXPERIMENTAL AND NUMERICAL STUDY

4.1 Introduction

In this chapter, all the equipments used in the experimental work are presented and the procedures followed in the experimental study are explained in details. Different methods of residual stress measurement are discussed. XRD measurement procedure used in this thesis is explained. The method of strain gauge measurement is presented. Additionally, construction of the numerical model is presented and numerical model is verified by comparing the results with the analytical results for a sample autofrettage pressure.

4.2 Experimental Study

4.2.1 Autofrettage test unit

Autofrettage tests are performed on a hydraulic autofrettage test stand, PN 497 as shown in Figure 4.1, available in Delphi Otomotiv Sistemleri San. ve Tic. A.Ş. in İzmir-Turkey. It is designed and built by the company Maximator and it serves to carry out burst pressure tests and autofrettage of various rails from the prototype construction up to 1500 MPa. The following rails can be tested in the test stand:

- Rails with a total length of between 100 and 1000 mm.
- Rails with a through-hole of 4 mm to maximum 10 mm seal diameter
- Rails with lower boreholes up to maximum 5 mm seal diameter
- Blind hole rails, the contact surface of the blind hole

Figure 4.1 Autofrettage test unit [63]

In the test stand, the axial connections are closed via a fixture as shown in Figure 4.2. Venting is effected via the last injector connection as shown in Figure 4.2(b). The stroke of the inner cylinder is maximum 15 mm and that of the outer cylinder maximum 80mm. The clamping pressure rises proportionally to the test pressure [63].

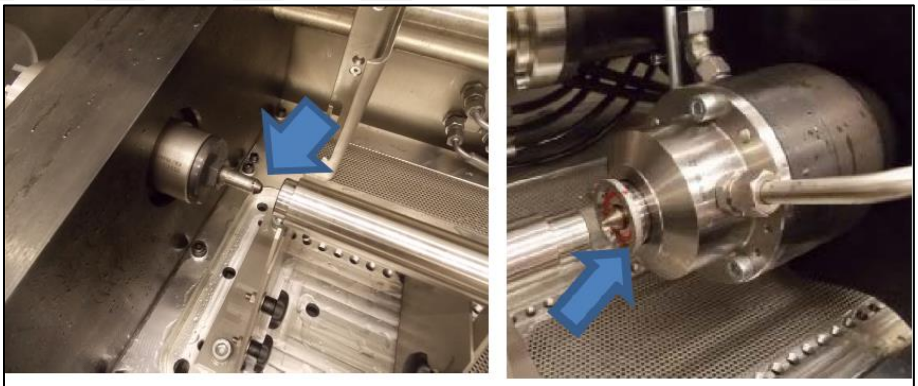

(a) (b)

Figure 4.2 Axial Fixture. (a) sealing pin, (b) upper sealing pin [63]

The main component of a hydraulic autofrettage test stand is the pressure intensifier which serves the purpose of generating high pressure for processing components. Basic principle of generating high pressure is illustrated with Figure 4.3 showing a sectional view of an intensifier. It consists of two small cylinders (high pressure cylinders) and a large central cylinder (low pressure cylinder). Ultra-high pressure is created by the ratio of the working areas of small and large cylinder.

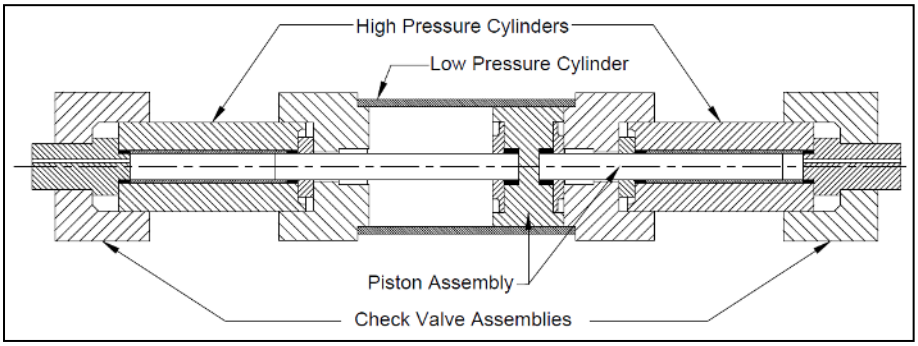

Figure 4.3 Sectional view of an intensifier pump [13]

The pressure intensifier used in this bench is given in Figure 4.4. It consists of primary (hydraulic drive) part and secondary part (high pressure drive) and it is controlled hydraulically using a proportional control valve [63].

- **Primary part (hydraulic drive):** The pressure intensifier is driven by the primary part. It works like a hydraulic cylinder. The main components are the piston rod and pistons as well as the cylinder pipe with the cylinder base and cylinder lid.
- **Secondary part (high pressure drive):** High pressure is produced in the secondary part of the pressure intensifier. This consists of the high pressure seal (found on the piston rod) and high pressure coating with the high pressure lid. The high pressure connection is found in the high pressure lid.

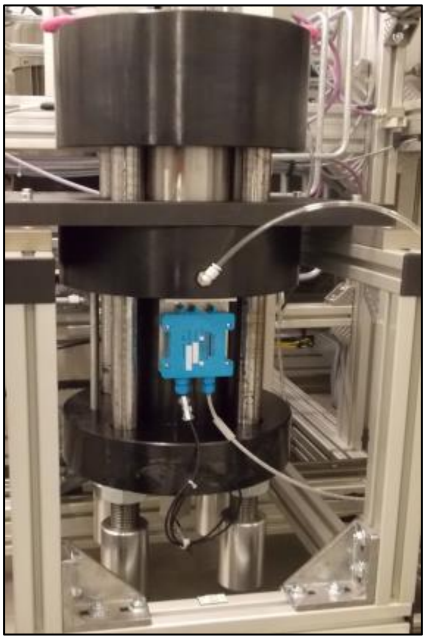

Figure 4.4 Pressure intensifier (DU 114) [63]

Maxifluid HD 15K is used as the test fluid. The cleanliness requirement (particulate contamination levels per millilitre of fluid at 3 sizes) for Maxifluid must be at least 21/18/13 according to ISO 4406 for the filling process. Hydraulic oil ISO-VG46 DIN 51524 part 2 is used to operate the hydraulic unit [63].

The system features a heat exchanger. For this reason, water quality and contents are of great importance. The hardness formers precipitate at higher temperatures and form a surface coating that diminishes the heat exchanger's cooling performance. 63°C is the deemed critical temperature. For very hard water, having dissolved mineral hardness is greater than 7 grain per gallon, this surface coating shall be considered in the heat exchanger's dimensioning [63].

4.2.2 Material

The choice of the material for the experimental study depends on several factors, including mechanical properties such as yield strength and ultimate tensile strength as well as maximum pressure capacity and the intended use of the autofrettage test unit. Up to the strength level of approximately 1200 MPa, the AISI 4140 and 4340 classes of steels have been widely used for a long period of time in many industrial applications such as fuel rails and high pressure cylinder of waterjet intensifiers. In this study 4140 steel is selected as the test material.

Young's modulus (E), yield strength (S_y) and ultimate tensile strength (S_{ut}) are determined from tensile tests performed on Zwick® test device according to ISO 6892 standards. Poisson's ratio (ν) and hardness (HRC) are determined by strain gauge and hardness test respectively. Values of these parameters are given in Table 4.1.

Table 4.1 Mechanical properties of AISI 4140 steel

E [GPa]	S_y [MPa]	S_{ut} [MPa]	ν	Hardness
208	700	992	0.3	37 HRC

The stress-strain relationship used in this thesis is expressed by a linear function for the elastic region and a power function for the plastic region (Huang's model) as illustrated in the following equations:

$$\sigma = E\varepsilon \quad (\varepsilon \leq \varepsilon_y) \tag{4.1}$$

$$\sigma = A_1 + A_2\varepsilon^{B_1} \quad (\varepsilon \geq \varepsilon_y) \tag{4.2}$$

For the test material, A_1, A_2 and B_1 are determined as 1676 MPa, -395.6 MPa and -0.1575 respectively by using Matlab® curve fitting tool.

True stress-true strain curves of the material obtained from both tensile test and Huang's model are represented in Figure 4.5 together. As it is seen in the Figure, Huang's model fits the experimental stress-strain curve very well. Statistical parameters belong to curve fitting are: Sum of square error, SSE=564.2; coefficient of regression, R-sqr=0.9997 and root mean square error, RMSE=1.76.

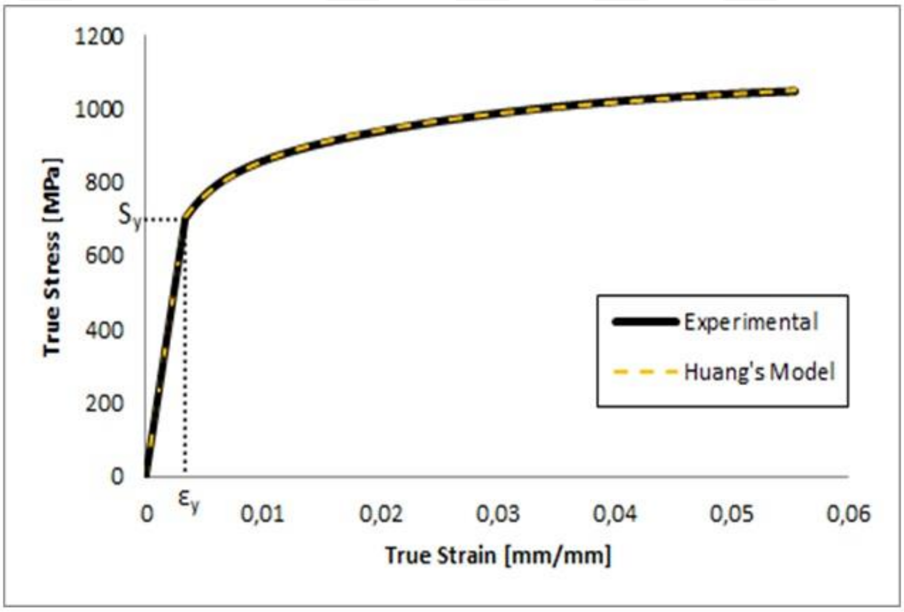

Figure 4.5 True stress-true strain curves for the test material (AISI 4140 steel)

4.2.3 Test Samples

Technical drawing of the test samples are given in Figure 4.6. The samples are produced by several processes from a solid cylindrical bar. Firstly, the stock material with 32 mm outside diameter is cut into 500 mm lengths. All the pieces are then drilled to 10 mm diameter by using gun drilling process as shown in Figure 4.7. In gun drilling process, rotational speed, feed rate and the pressure of the cutting fluid are taken as 3200 rpm, 30 mm/min and 50 bar respectively. After drilling process, the pieces are cut into 200 mm lengths and machined to 30 mm diameter by using a

CNC lathe and $2x60^0$ countersinks are machined on both ends. A total of 24 samples are produced. Some of these samples are illustrated in Figure 4.8.

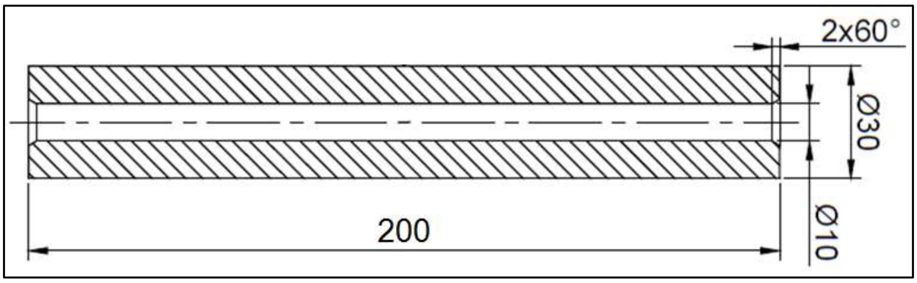

Figure 4.6 Technical drawing of the test samples

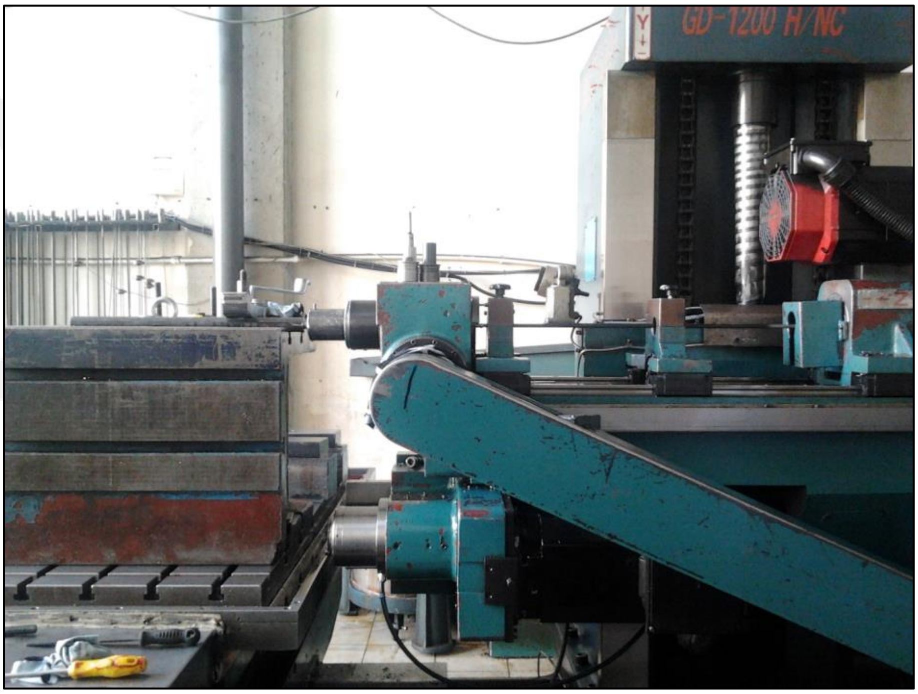

Figure 4.7 Gun drilling process [64]

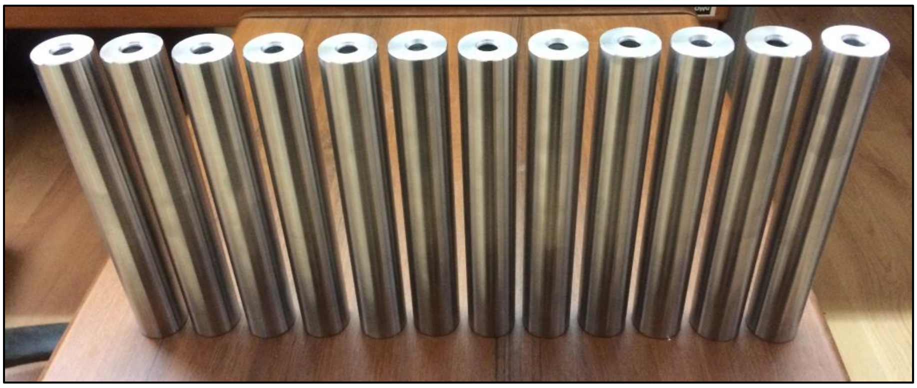

Figure 4.8 Test samples

4.2.4 Design of Experiment

In order to investigate the effect of the autofrettage pressure on residual stress distribution on the wall of the cylinders, different autofrettage pressures are applied in the autofrettage tests. The pressure range is selected in such a way that lower limit (P_{lower}) will be the pressure which causes the interface radius (b) to be equal to inner radius (a) (this means that there is no plastic deformation on the wall of the cylinder below this pressure) and the upper limit (P_{upper}) is the pressure which causes equivalent residual stress at the inner surface to be equal to the yield strength in compression (S_{yc}) of the material to avoid reverse yielding.

At the last section of Chapter 3, it was stated that experimental condition does not exactly fit to analytical analysis but can safely be used for rough estimation of autofrettage pressures to be assigned in the experimental studies.

The lower limit is calculated as 359.2 MPa from Eq. (85) and the upper limit is calculated as 805.8 MPa from Eqs. (82 to 84) and Eq. (46). Between these two pressure limits, approximate values of the autofrettage pressures used in the experiments are selected as 530, 550, 570, 590, 610, 630, 650 and 670 MPa and each test is repeated for three times to minimize the experimental error.

4.2.5 Autofrettage Test Sequence

In this section, autofrettage test procedure is described with three steps as follow:

Test preparation:

- The samples have strain gauges at the middle of the outer surface are ordered according to autofrettage test pressure values.
- Test chamber door is opened and each sample is placed into the fixture and the mandrel is pushed onto so that it is placed on a suitable prism surface. The sample is centred to the mandrel and the clamping cylinders are aligned.
- The fixture slides are moved to the end of the sample and they are unhooked on both sides.
- The test chamber door is closed.

Autofrettage process:

- On the autofrettage test unit, the process and rail type are selected as ‘autofrettage’ and ‘through-hole’ respectively via panel PC.
- Autofrettage test parameters such as autofrettage pressure and time are chosen.
- ‘Start test’ button is pushed and the process runs automatically. The outer cylinder moves toward the end of the sample; its position is regulated. When the flashing position is reached, the cylinder stops, and the filling pump is activated. At the same time, the pressure intensifier is moved forward at a defined speed (venting) and stops in the end position. Filling is carried out in the flushing time defined in the parameter configuration (defined as 4 sec.). The pressure intensifier is moved to the start position and at the same time it is filled via the filling pump. The autofrettage process is carried out according to selected parameters. The system’s clamping pressure (force) is automatically adjusted by the unit itself. As shown in Table 4.2, clamping force is proportionally to the autofrettage pressure.
- After the end of the process chain, both cylinders are automatically moved to the basic position, thereby relieving the test section.
- The test chamber door is opened and the sample is removed.

Test report:

After each autofrettage test, the test unit gives an autofrettage test report. For eight different autofrettage pressures, reports are given in Figures 4.9 to 4.16. Due to pressure tolerance limits of the autofrettage test unit (±100 bar) there are deviations between the given and the measured pressure values. Table 4.2 gives the average values of autofrettage pressures (P_a) and respective clamping force (F_c) measured by the test unit for the first 8 tests.

Table 4.2 Average values of the autofrettage pressures and clamping forces measured by the test unit

Test No	**1**	**2**	**3**	**4**	**5**	**6**	**7**	**8**
P_a [MPa]	530	550	570	587	608	628	646	666
F_c [KN]	124	126	127	128	130	132	133	134

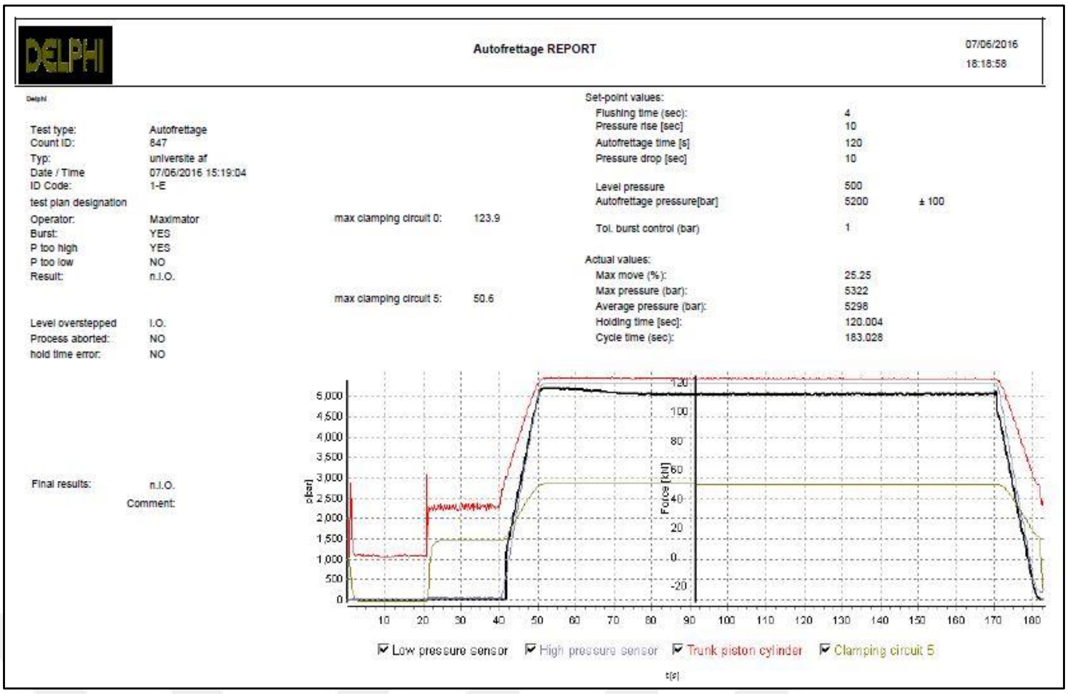

Figure 4.9 Autofrettage test report for 530MPa average pressure

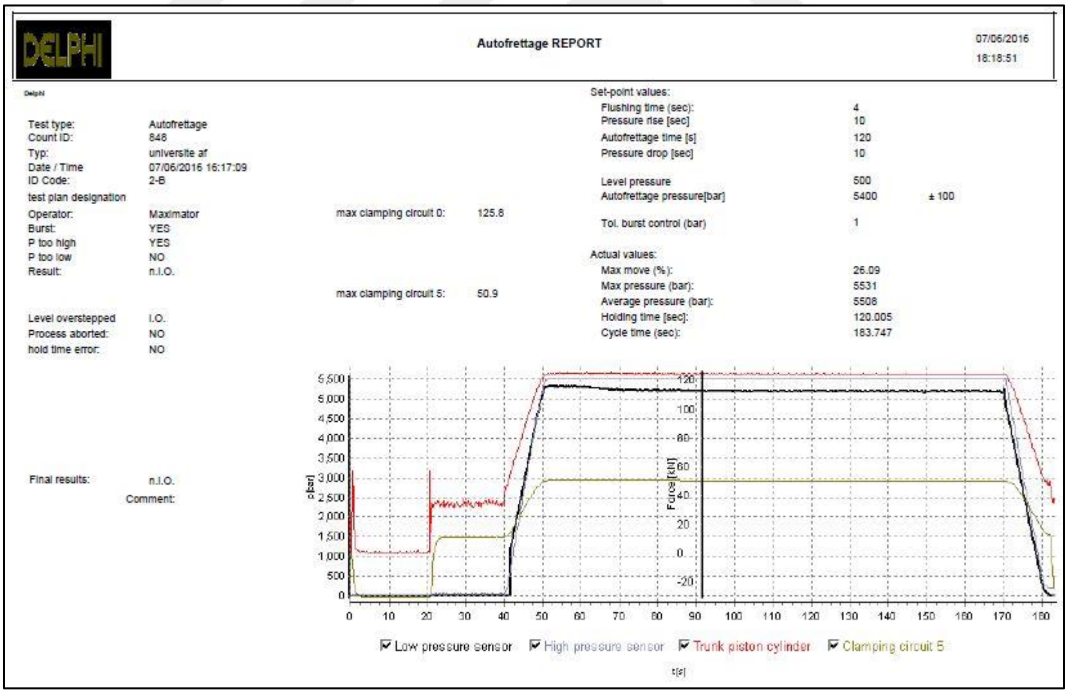

Figure 4.10 Autofrettage test report for 550MPa average pressure

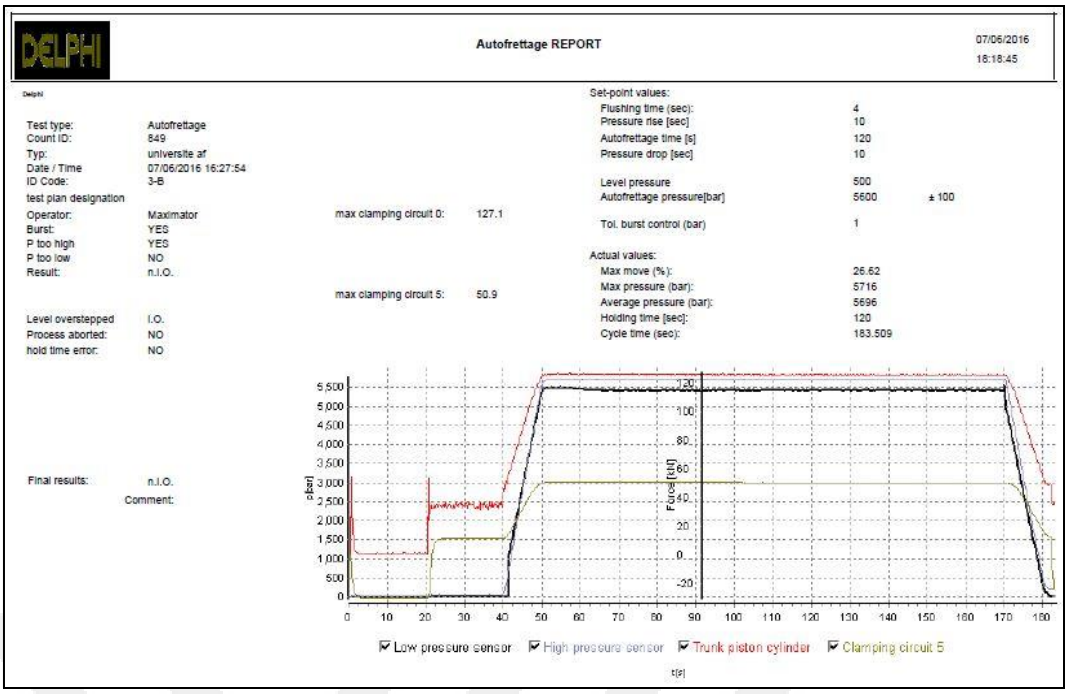

Figure 4.11 Autofrettage test report for 570MPa average pressure

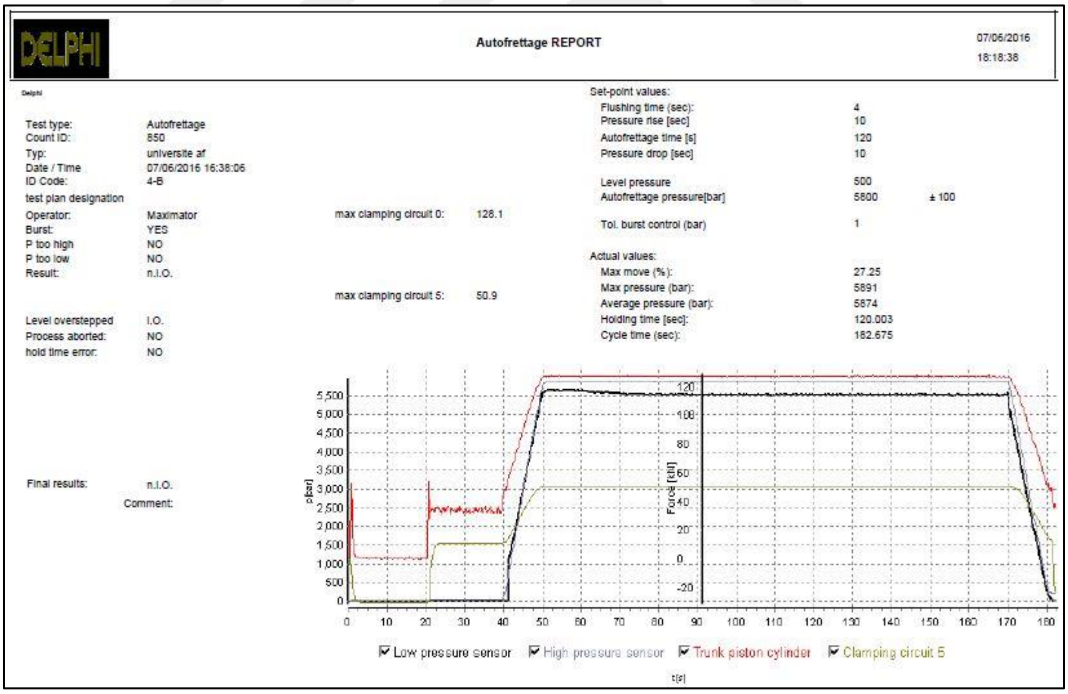

Figure 4.12 Autofrettage test report for 587MPa average pressure

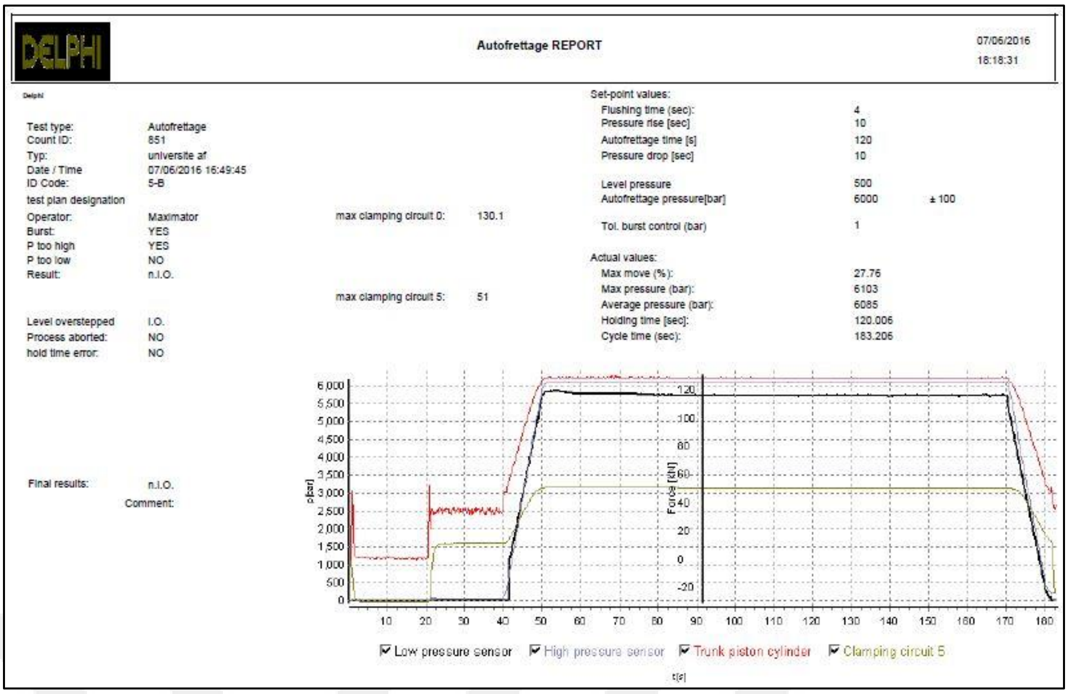

Figure 4.13 Autofrettage test report for 608 MPa average pressure

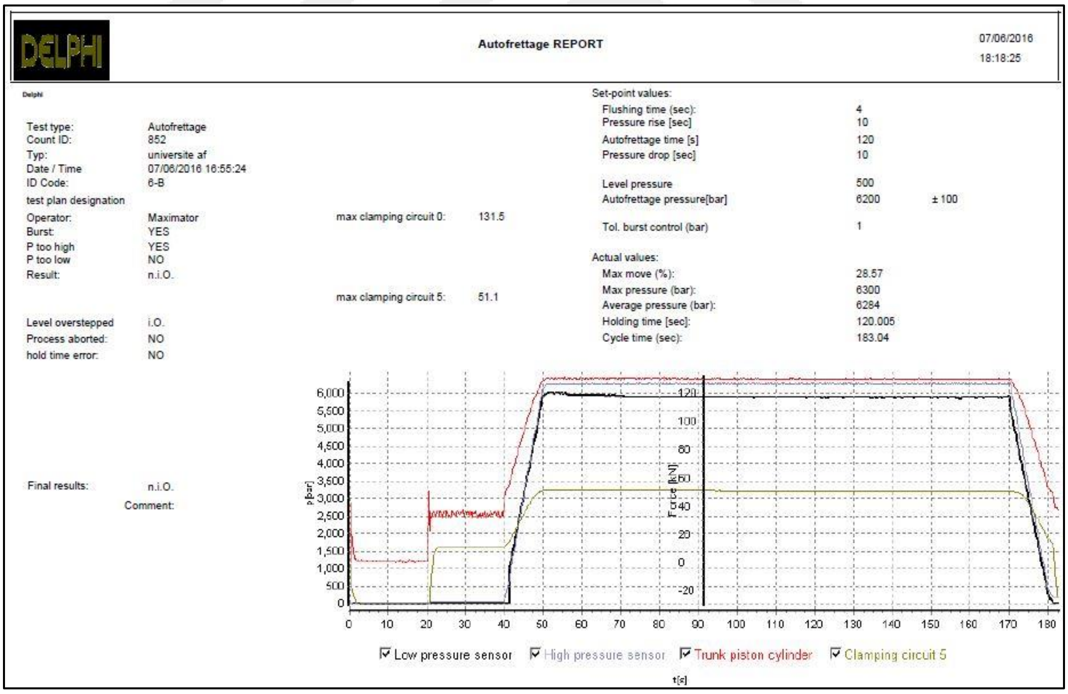

Figure 4.14 Autofrettage test report for 628 MPa average pressure

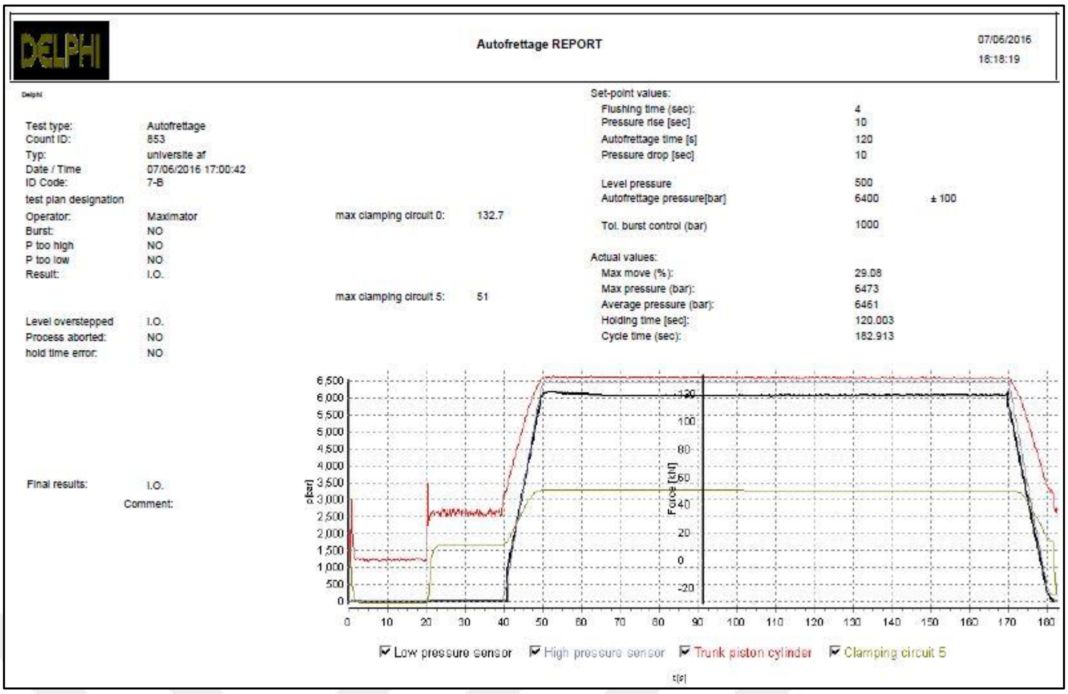

Figure 4.15 Autofrettage test report for 646 MPa average pressure

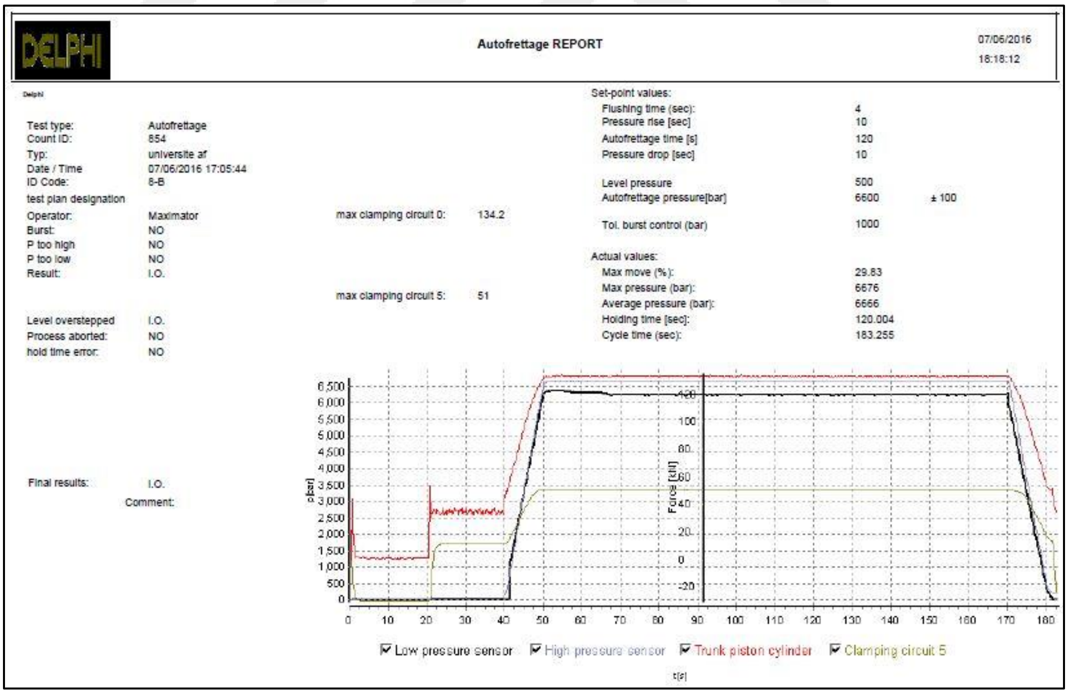

Figure 4.16 Autofrettage test report for 666 MPa average pressure

4.2.6 Strain Measurements

In order to obtain strain variation with respect to time during the autofrettage process, Vishay-C2A-06-062LT-350 type general-purpose 90° rosette strain gauges are mounted in the middle of the outer surface of 8 specimens as shown in Figure 4.17. The gauges are separately connected by two channels of a NI 9219 module and strain data in tangential and axial directions is collected in 100 Hz frequency for 120 seconds. Technical data of the strain gauge is given in Figure 4.18.

Figure 4.17 The samples with strain gauges

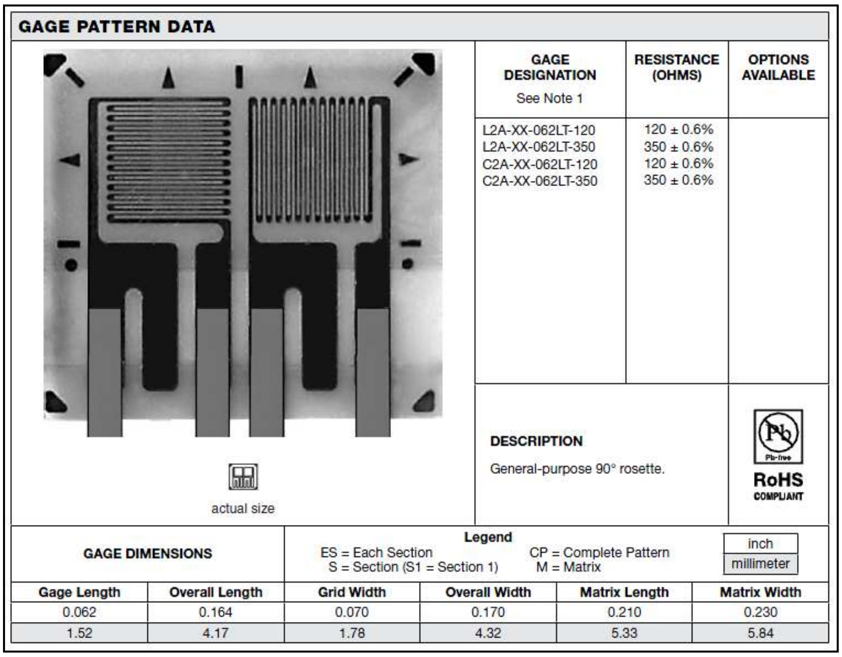

GAGE PATTERN DATA

GAGE DESIGNATION (See Note 1)	RESISTANCE (OHMS)	OPTIONS AVAILABLE
L2A-XX-062LT-120	120 ± 0.6%	
L2A-XX-062LT-350	350 ± 0.6%	
C2A-XX-062LT-120	120 ± 0.6%	
C2A-XX-062LT-350	350 ± 0.6%	

actual size

DESCRIPTION

General-purpose 90° rosette.

RoHS COMPLIANT

GAGE DIMENSIONS

Legend: ES = Each Section, S = Section (S1 = Section 1), CP = Complete Pattern, M = Matrix

	Gage Length	Overall Length	Grid Width	Overall Width	Matrix Length	Matrix Width
inch	0.062	0.164	0.070	0.170	0.210	0.230
millimeter	1.52	4.17	1.78	4.32	5.33	5.84

Figure 4.18 Strain gauge-Vishay-C2A-06-062LT-350

4.2.7 Residual Stress Measurement

Residual stress can be defined as the stresses remain in a material after manufacturing and material processing in the absence of external forces or thermal gradients [65]. These stresses can exhibit either harmful or beneficial effect depending upon the magnitude, sign and distribution of the stress with respect to the load-induced stresses. For example, the presence of tensile residual stresses in a part is generally harmful since they act as an additive stress which contributes to fatigue and other structural failures. Whereas, compressive type of residual stresses are usually beneficial since they act as subtractive stress which prevents origination and propagation of fatigue cracks, improve wear resistance and load bearing capacity (i.e. in the thick walled cylinder applications).

4.2.7.1 Available Methods

There are many types of methods for measuring the residual stress in a component. They can be classified as destructive, semi destructive or non-destructive as shown in Figure 4.19.

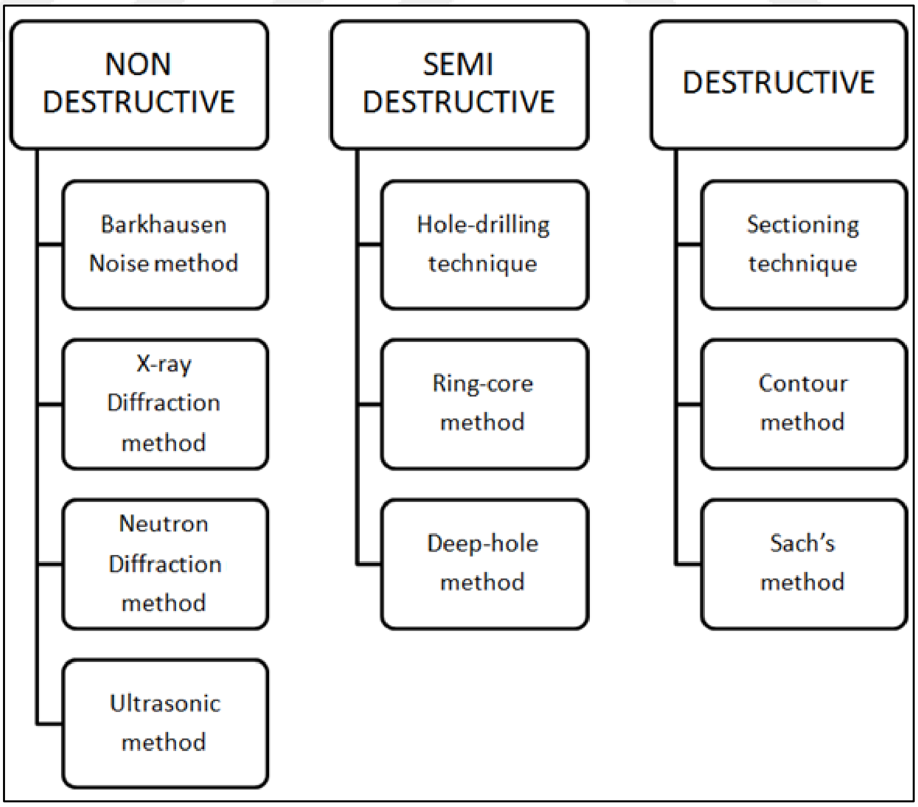

Figure 4.19 Residual stress measuring techniques [66]

Among these methods, Sach's method, hole drilling technique, X-ray diffraction and neutron diffraction are mostly used methods for measuring residual stresses in thick walled cylinders. Comparisons of these methods are given in Table 4.3.

Table 4.3 Comparison of various residual measurement techniques used in autofrettage studies [8]

Technique	**Merits**	**Demerits**
Sach's boring	Simple and accurate	Destructive and time consuming. The bore operation induces additional residual stresses in the sample.
Hole drilling	Simple and accurate	Time consuming.
X-ray diffraction	Non-destructive and accurate	Method useful only for surface measurements due to low penetrability of X-rays.
Neutron Diffraction	Non-destructive, accurate and better penetrability than XRD	Expensive and need a lot of safety measurements.

Sach's Method

Sachs's method basically involves observing the deformation caused by the removal of a sequence of layers of material [66] as shown in Figure 4.20. To carry out this technique, the test specimens is bored on a lathe machine using an automatic clamping chuck with variable adjusting clamping pressure to allow the cylinder expansion. After every removing, the dimensions of the specimens (outer radius and length) are measured e.g. with a digital micrometre or by using a strain gauge. Then the strains ε_θ* and ε_z* in radial and longitudinal direction will be calculated for a given radius r* based on the outer diameter and length before and after each removing [19]. Finally, the residual stresses can be calculated. There are some expressions for residual stress calculations. Following expressions suggested by Magehed-Abbas [67] may be used for quick calculations of residual radial stress, $(\sigma_r^*)_R$, and residual tangential stress, $(\sigma_\theta^*)_R$.

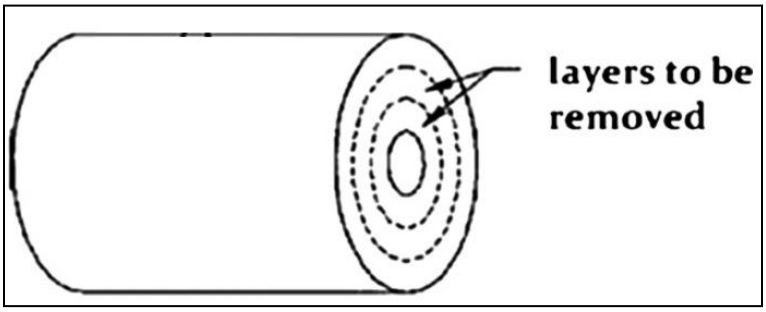

Figure 4.20 Sach's method [66]

$$(\sigma_r{}^*)_R = \frac{E}{(1-\nu^2)} \frac{(\varepsilon_\theta{}^* + \nu\varepsilon_z{}^*)(b^2 - r^{*2})}{2r^{*2}} \tag{4.3}$$

$$(\sigma_\theta{}^*)_R = \frac{E\pi}{(1-\nu^2)} \left[(b^2 - r^{*2}) \frac{d(\varepsilon_\theta{}^* + \nu\varepsilon_z{}^*)}{d(\pi r^{*2})} - \frac{b^2 + r^{*2}}{2\pi r^{*2}} (\varepsilon_\theta{}^* + \nu\varepsilon_z{}^*) \right] \tag{4.4}$$

where, b, E and ν are outer radius, modulus of elasticity and Poisson’s ratio respectively.

Hole Drilling Method

Hole drilling method is another destructive residual stress measuring method which is based on destruction of the state of equilibrium of residual stresses after machining. In this method, a special three or six element strain gauge rosette is installed on the residually stresses body and a small, shallow hole typically 0.8 to 4.8 mm in both diameter and depth is drilled through the center of the rosette by using a precise milling guide as shown in Figure 4.21. Drilling a hole eliminates the stresses at that location and changes the stress in the surrounding region. Correspondingly, the local strains on the surface of the test sample changes. By measuring these strains with a multi-channel static strain indicator and using the elastic theory, residual stresses and their angular orientation are calculated. To avoid computation lobor, a specialized computer program such as H-Drill may be used for the calculation [68].

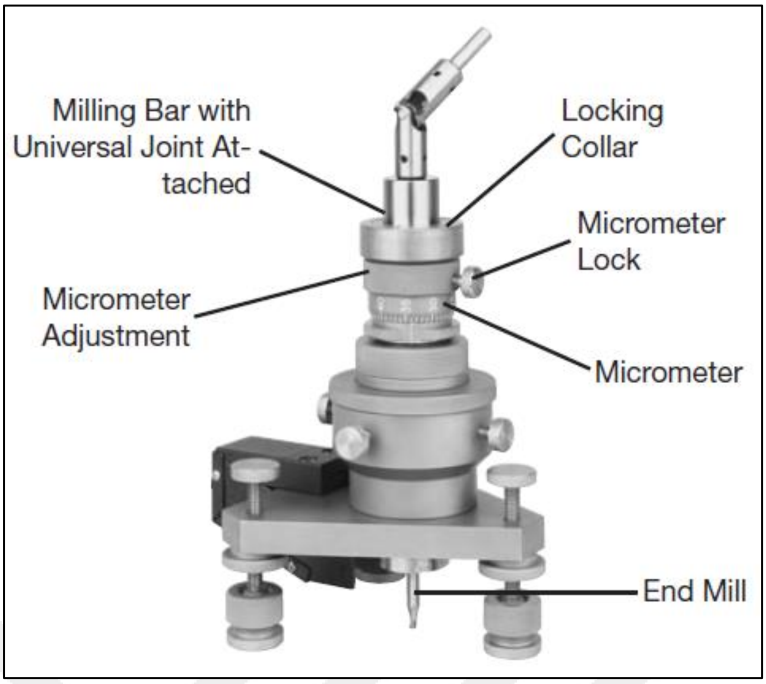

Figure 4.21 Hole-Drilling set-up [68]

Strain changes may be also determined by interferometric measurements of surface displacements by using high resolution cameras. This technique is known as Electronic Speckle Pattern Interferometry (ESPI) and there are commercial ESPI equipments as illustrated in Figure 4.22. In this method, the sample is illuminated with coherent laser light which produces speckle patterns. Four images are obtained before and after drilling. These images allow calculating a phase angle for each pixel, which then is translated into a surface displacement [69].

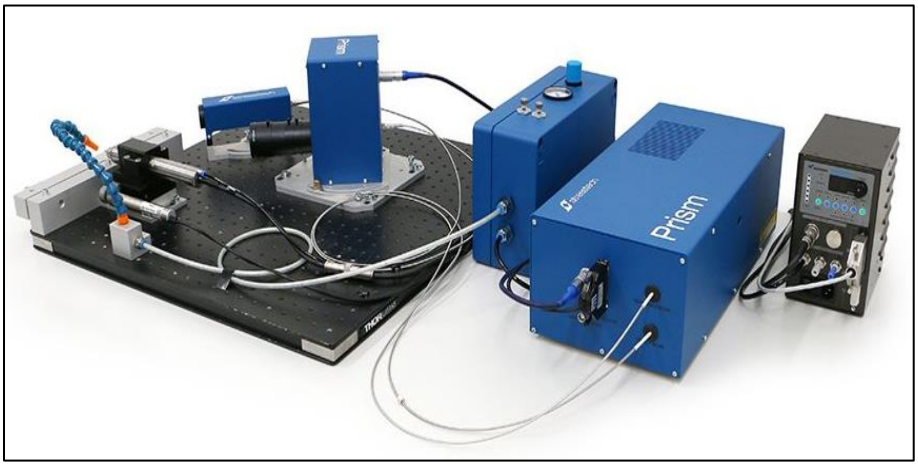

Figure 4.22 ESPI-Hole drilling [69]

Diffraction Methods

Diffraction methods such as neutron diffraction (ND) as classical X-ray diffraction (XRD) and strong X-ray synchrotron diffraction (SD) are given under the same topic as they work on the same principle. In these methods, the changes in strain is measured and converted into stress by measuring the shifts in the diffraction peak. Neutron diffraction uses neutrons generated by fission or spallation. X-ray diffraction uses x-rays instead of neutron [70].

X-ray diffraction technique is suitable only for surface measurements because X-rays interact with electrons and get absorbed in the material after moving a few micrometers. This problem does not arise in the neutron diffraction technique because the chargeless neutrons do not interact with any particle. However, the neutron method is expensive and it needs a lot of safety measurements [8].

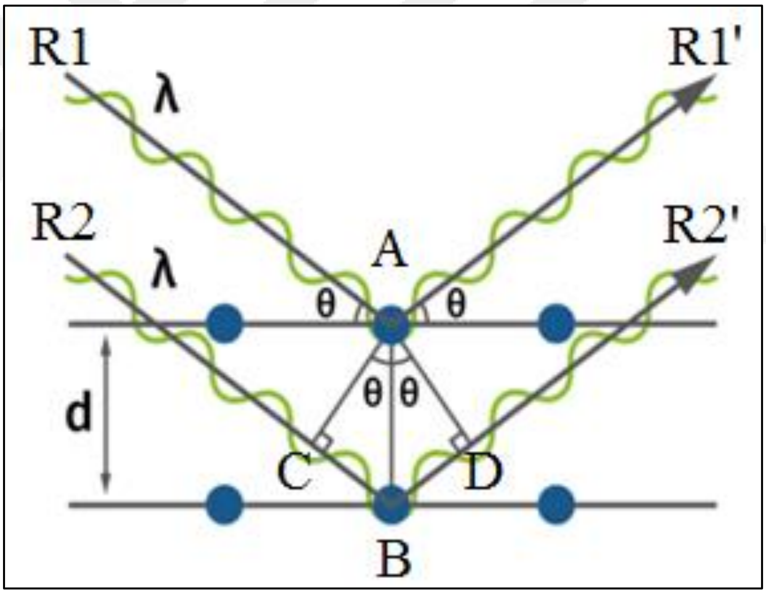

Figure 4.23 Diffraction of x-rays by a crystal lattice [69]

The basic principle of measuring the residual stresses in a material by x-ray diffraction starts by utilizing Bragg's law. Considering x-ray source placed at a suitable angle (θ) and sends two x-rays with same wavelength (R1 and R2) as shown in Figure 4.23. The x-rays are reflected by the molecules (A and B) located on the layers of atom separated by distance "d". Due to the distance between the molecules, the second ray (R2) must travel an extra path (CB+BD) which equals to "2dsinθ" from the geometry. The relationship between this distance and the wavelength of x-ray (λ) gives the Bragg's law and expressed as;

$$n\lambda = 2d\sin\theta \tag{4.5}$$

where, n is the order of the diffraction.

There is also a clear relationship between the diffraction pattern and the distance between atomic planes (d). When a material is strained, the inter-planer spacing of the lattice planes (d) is changed. By comparing the strained inter-planer spacing with unstressed lattice inter-planer spacing, the strain in the material can be obtained from the following equation.

$$\varepsilon_z = \frac{d_n - d_0}{d_0} \tag{4.6}$$

This equation gives the strain value for the measurements taken normal to the surface where the stress in this direction is assumed as zero (plane stress condition). By rotating the sample or the goniometer around the measurement location, measurements of planes at an angle ψ can be obtained which gives the planer principle stresses. In this case, the strain formula forms as follows:

$$\varepsilon_\psi = \frac{d_{\phi\psi} - d_0}{d_0} \tag{4.7}$$

where, ϕ is the angle between a fixed direction in the plane of the sample and the projection in that plane of the normal of the diffracting plane and ψ is the angle between the normal of the sample and the normal of the diffracting plane [71]. In order to calculate the stress in any chosen direction the extended version of Hook's law given in Eq. (8) can be used. For more complex solutions, e.g. presence of shear stresses and inhomogeneous stress state within the material. the inter-planer spacing or 2θ peak position is plotted and the stress is calculated from this plot by calculating the gradient of the line and the elastic properties of the material. $\mathrm{Sin}^2\psi$ and Dölle-Hauk are the most commonly methods work on this basis.

$$\sigma_\phi = \frac{E}{(1+\nu)} \frac{d_\psi - d_n}{d_n} \tag{4.8}$$

4.2.7.2 Residual Stress Measurement Procedure

Probability of having not accurate results from Sach's method and the risk of duplication of the autofrettage tests in case error in practice leads us choosing semi-destructive or non-destructive measurement methods. Due to their very nature, XRD is suitable for surface measurements, SD for shallow depths and thin specimens, and ND for bulk measurements within thick specimens. Also, ND and SD cannot provide for in-situ investigations and are only available in some facilities worldwide. Therefore, x-ray diffraction method is selected for this study.

The XRD equipment used in this work is a Stresstech portable residual stress analyser, Xstress 3000 G2/G2R model illustrated in Figure 4.24, available in The Metal Forming Center of Excellence (MFCE) in Atilim University. It has a G2 goniometer which is mounted on a tripod with magnetic anchoring. Distance between goniometer and the measurement point is automatically adjusted with ± 0.003 mm accuracy. The analysis software, XTronic version 1.9 1r5162, is a windows based package has multiple d-sin^2 exposure modes and has the capability to calculate the peak shift by cross-correlation and three other methods.

Figure 4.24 XRD residual stress measurement device [69]

Since the middle of the cylinder is taken as the reference section in this study, residual stress measurements are made on this section. Therefore, all the parts are cut in half by using both AWJ turning and EDM process before the measurements. It is also estimated that the results may be affected by the detrimental effects of the cutting process. Some trial measurements are made to find out if there is any difference between the results of different cutting methods. It is found that radial and hoop stresses are almost equal to each other for each measurement point and they are negative for the specimens that are cut by AWJ turning process and positive for the specimens cut by EDM cutting process. To overcome this problem, the affected region due to cutting process is removed by electro-polishing. A Struers Electrolytic Polisher Model LectroPol-5 shown in Figure 4.25 is used for electro-polishing process. The device uses a saltwater solution comprised of 80grams of salt (NACl) per liter of distilled water. The voltage is set to 40 V for 20 seconds. Before the process, all the test pieces are cut again from the other side with a length of 30 mm to be placed on the device and then they are electro-polished 10 times. After each polishing they are allowed to cool down and approximately 2 mm material is removed from the surface.

Figure 4.25 Electro - polishing process

Before the measurements, the x-ray device is calibrated to the zero stress position using a non-autofrettaged test specimen. Cr x-ray source is used to measure the residual stresses in tangential and axial directions in autofrettaged test samples. The samples are put on an adjustable spot perpendicularly as shown in the Figure 4.26. The tensor method is selected as 3 angles, 0°, 45° and 90° and cross correlation and Dölle-Hauk methods are selected for peak shift analysis and the calculation of stress tensor components respectively. All other set-up parameters are set to default values.

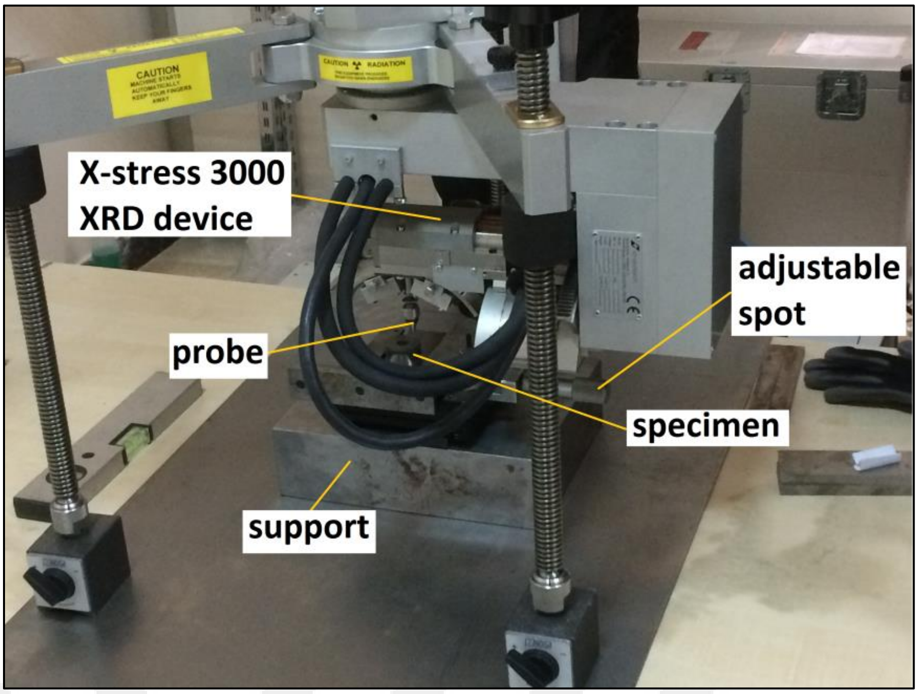

Figure 4.26 XRD residual stress measurement

Residual stresses are measured at 5 points along the thickness of the cylinders. Since the collimator used in the measurements has 1 mm spot size, each measurement gives the average stress in 1 mm diameter circle as illustrated in Figure 4.27 and corresponding radius values for each point is given in Table 4.4.

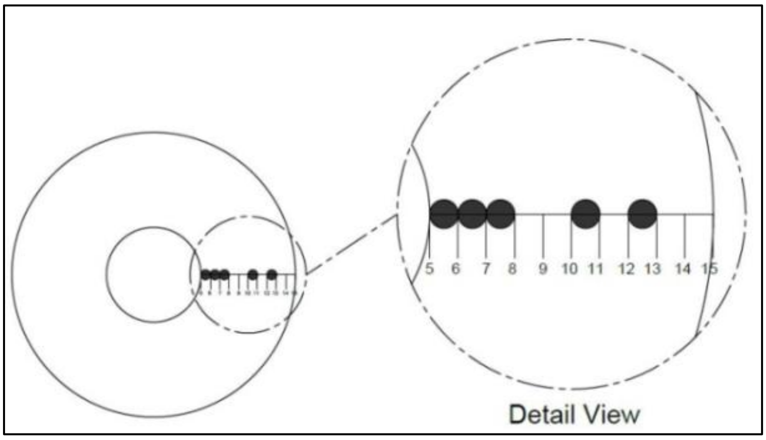

Figure 4.27 Schematic representation of the measurement points

Table 4.4 Radial distance intervals corresponding to measurements

1	2	3	4	5
5-6 mm	6-7 mm	7-8 mm	10-11 mm	12-13 mm

4.3 Finite Element Modelling

4.3.1 Introduction

The finite element method is a numerical analysis technique which has been using for predicting and simulating the physical behaviour of complex engineering systems since it was originally introduced by Turner et al. in 1956 [72]. It provides approximate solutions to wide variety of engineering problems in a short time, and therefore, receiving much attention in engineering schools and in industry.

Finite element analysis works on the basis of dividing the domain into a finite number of elements, over which a set of equations are solved and combining the solutions of each element. The elements are notionally small regions and they are connected to each other by their common "nodes". Some of the most usual elements with nodes are shown in Figure 4.28. All the elements with nodes are connected to each other and construct a grid, called mesh. The accuracy of the model is related to approximate function defined for the elements and the mesh size that is used in the analysis. As the size of the element is getting smaller which is resulted as a finer mesh, the solution will be more accurate. However, in some cases, an excessive number of elements may increase the round-off error. To overcome this problem, some methods such as adaptive meshing, mesh refinement test or sub-modelling may be used [72, 73].

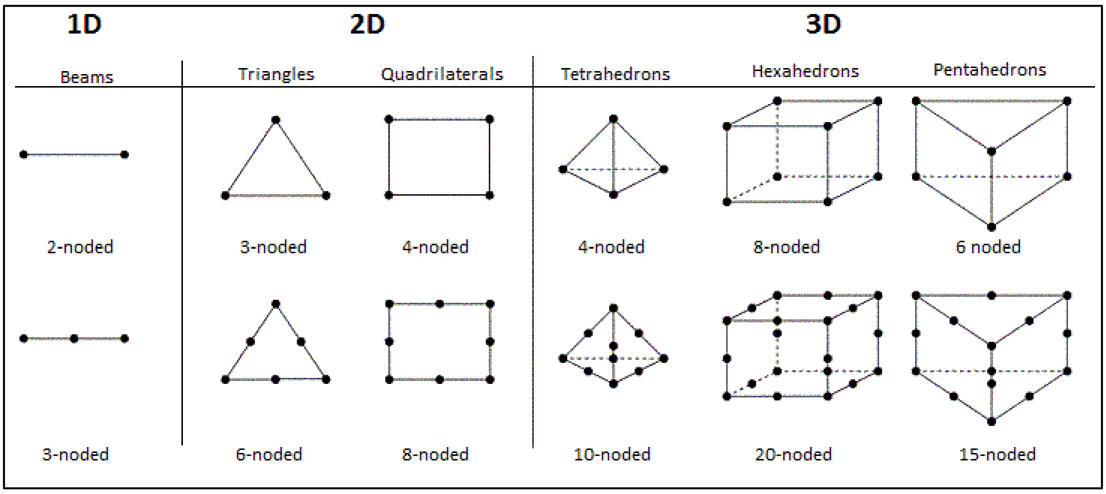

Figure 4.28 Types of line, area and volume elements with node numbers

The modelling of an engineering problem using FEA requires either development a computer program by using FEA formulation or using a commercially available general-purpose FEA program such as ANSYS, ABAQUS, WELSIM, WaveFEA etc. In this thesis, the finite element analyses are performed by using ANSYS Workbench 15.0.

4.3.2 Finite Element Modelling with ANSYS Workbench

The ANSYS program is a powerful, multi-purpose analysis tool which is capable of simulating problems in a wide range of engineering disciplines such as structural, electrical, dynamics, fluid dynamics, thermal analysis etc. [72]

Numerical analysis in ANSYS is carried out in three main levels as pre-processor, solution and postprocessor as schematically given in Figure 4.29. In the pre-processor, element type and material properties are specified, the model geometry is developed and the mesh is generated. The analysis type and options, boundary conditions are specified and the solution of the model is obtained in the solution processor. The results which include plots, deformed shapes and list of the results in tabular format are reviewed in the postprocessor level.

Figure 4.29 Schematic of ANSYS levels [72]

4.3.3 Finite Element Modelling of Autofrettage Process

Numerical model of the autofrettage process is developed in ANSYS Workbench 15.0. Each autofrettage condition applied in the experimental study is analysed separately. 2D axisymmetric analysis method is selected for the analyses to obtain finer mesh for more accurate results and the geometry is constructed based on this assumption. “Design Modeller” of ANSYS Workbench 15.0 is used in the construction of the geometry which consists of three surface bodies (fixtures and the cylinder) with zero thickness. Figure 4.30 shows the schematic view of the geometry.

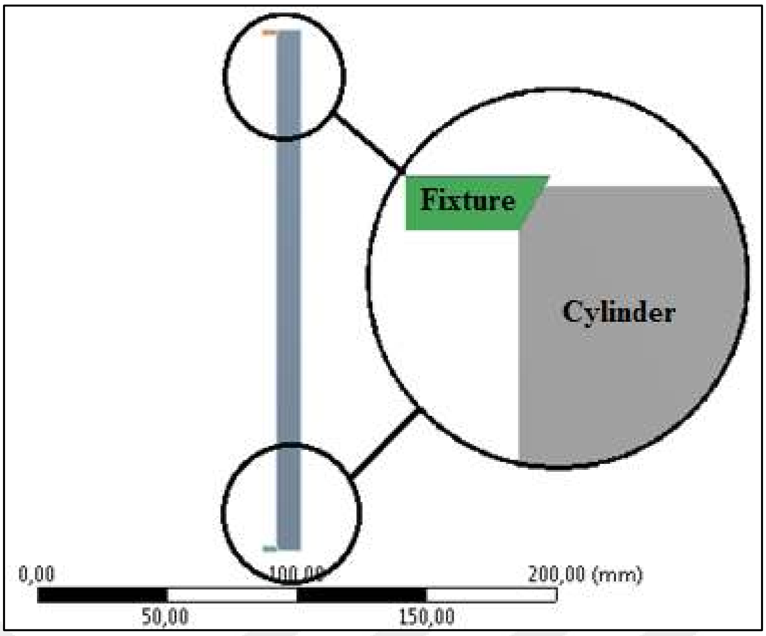

Figure 4.30 The geometry used in the 2D axisymmetric analysis

The materials for the fixtures and the cylinder are added into the "Engineering Data Source" of ANSYS Workbench 15.0. The fixture material is selected from the material list in Engineering Data Source as AISI 4340 steel with 1590 MPa tensile yield strength and 1720 MPa tensile ultimate strength. The mechanical properties of the cylinder material are defined based on the mechanical tests results performed in the experimental study. The other properties such as physical, thermal, electrical etc. are defined from the manufacturer catalogue. Since reverse yielding effect is not observed during the experiments and in the XRD results, multi-linear isotropic hardening model (which also fits with Huang's approximation) is selected to simplify stress-strain relationship of the cylinder material during plastic deformation. Five points are selected from true stress and true strain curve of the material and true stress-true plastic strain values are calculated. The formulations used in the calculations are given below:

True stress;

$$\sigma' = \sigma(1 + \varepsilon) \tag{4.9}$$

True strain;

$$\varepsilon' = \sigma'/E \tag{4.10}$$

Total elastic strain;

$$\varepsilon_t' = \ln(1 + \varepsilon) \tag{4.11}$$

Plastic true strain;

$$\varepsilon_p' = \varepsilon_t' - \varepsilon' \tag{4.12}$$

True stress-true plastic strain values calculated based on these formulas are given in Table 4.5. True stress-true plastic strain curve of the material is then plotted as shown in Figure 4.31 by adding these values in “Multi-linear Hardening Properties” section in ANSYS Workbench 15.0.

Table 4.5 True plastic strain vs. true stress values used in multi-linear hardening model

True plastic strain	True stress
0	700.000
0,0025	800.387
0,0060	860.868
0,0100	901.931
0,0281	999.838

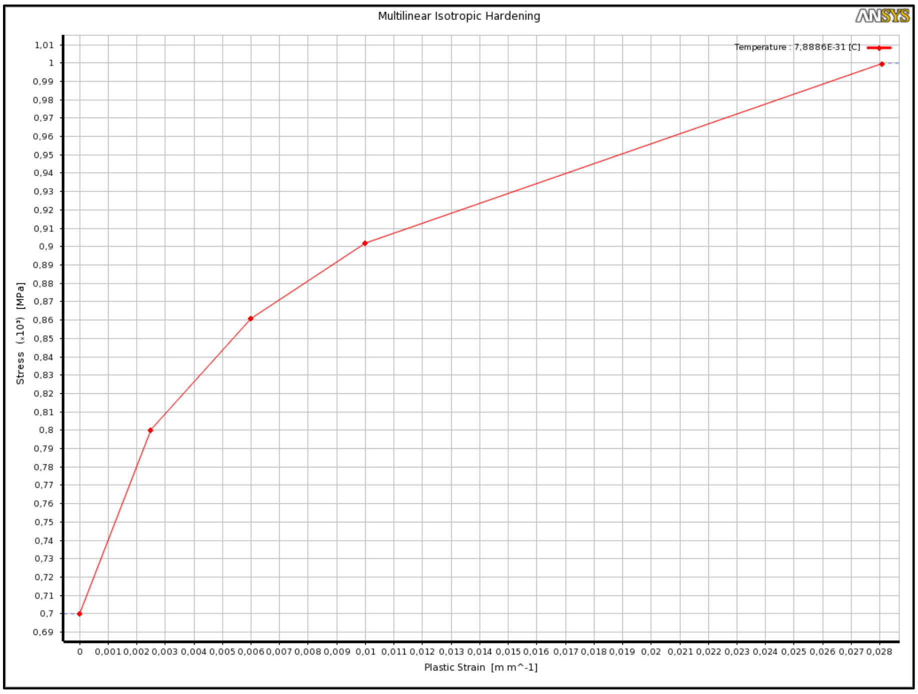

Figure 4.31 True stress-true plastic strain curve of the material

After determining the material properties, FE model is developed as schematically represented in Figure 4.32. Stiffness behaviour of each body is defined as flexible. Rough-surface body to surface body contact is assigned for each connection between the fixture and the cylinder. A total of 50735 quadratic elements with 154466 nodes are used in the model. Advanced size function, relevance center and smoothing of the mesh are assigned as curvature, coarse and medium respectively. Size of the elements is arranged to be between 0.1 and 0.2 mm.

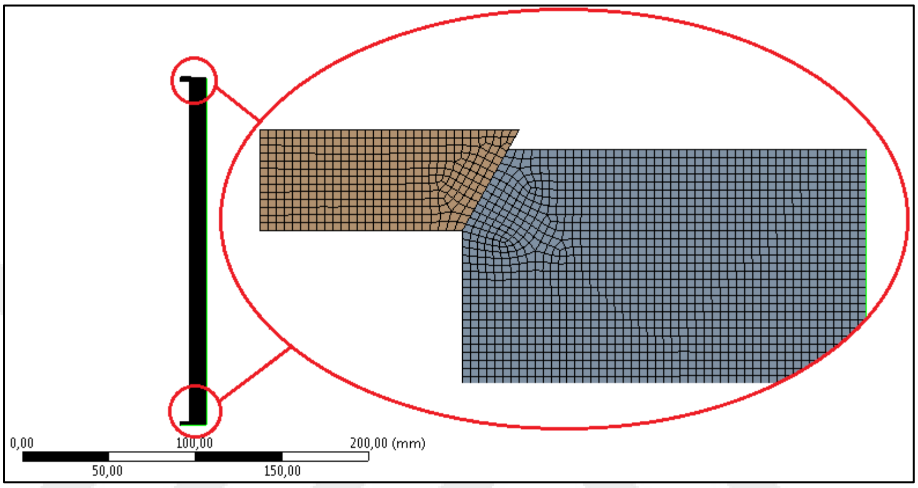

Figure 4.32 FE Model

Remote displacement in y direction and fixed support at the bottom edge of the fixture are defined as illustrated in Figure 4.33.

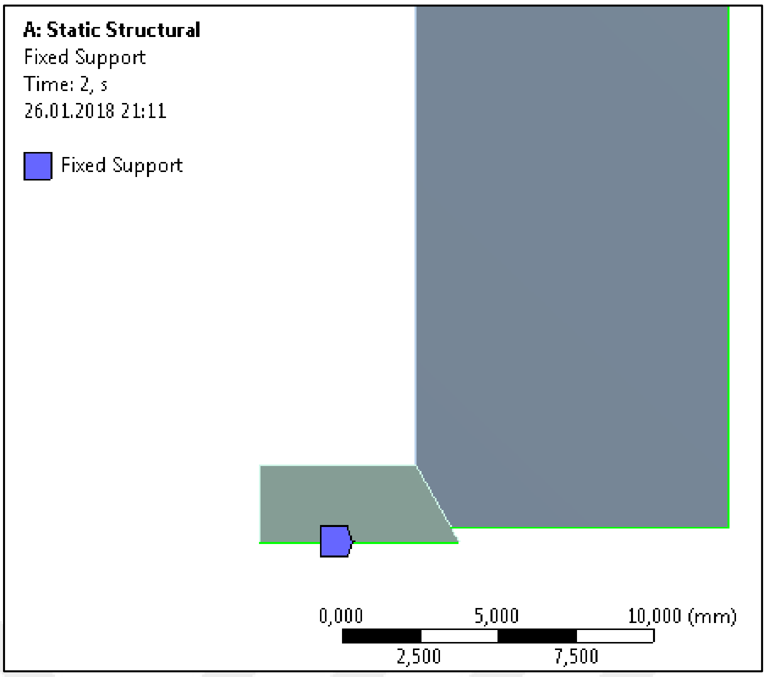

Figure 4.33 Fixed support

Loading condition is schematically represented in Figure 4.34. Fc, Pa and S represent clamping force, autofrettage pressure and the fixed support respectively. Analyses are performed in two steps for each autofrettage condition. In the first step, the autofrettage pressure and the clamping force are applied together and in the second step, the loads are removed. At the middle of the cylinder, a path is selected starting from the inner surface to the outer surface (from A to B) and stress-strain values are evaluated from this path. The path has a total of 200 sampling points.

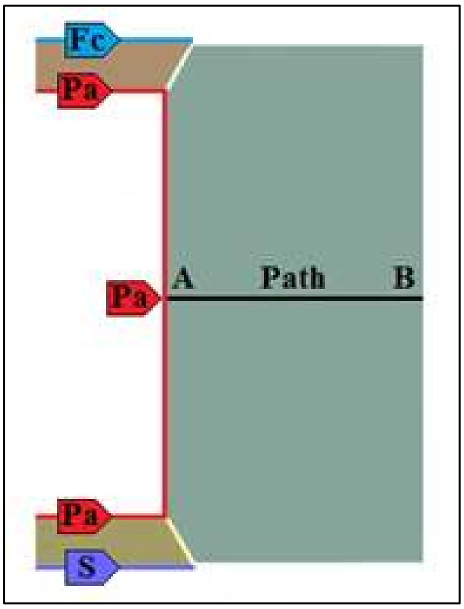

Figure 4.34 Schematic view of FE model

Before FE analyses, a FE model is created to check the accuracy of the assumptions that will be used in the generation of the main FE model. This model is developed on the basis of the analytical model assumptions in which there is no clamping force acting on the cylinder and the strain in axial direction is zero (plain strain assumption). Therefore, frictionless supports are placed on both surfaces of the cylinder and only the autofrettage pressure is applied. Radial and tangential stresses along the path (as shown in Figure 4.34) for loading and unloading steps are compared with the analytical results for each pressure value used in the experimental study. An agreement between the analytical and numerical results is obtained. Table 4.6 gives analytical and numerical results for 530 MPa autofrettage pressure. It is seen that the results are almost the same along the thickness of the cylinder. The proximity of the results shows that the assumptions used in the development of the main FE model are suitable and the main FE model can be used to make comparisons with experimental results.

Table 4.6 Comparison of numerical and analytical results for plane strain case

radii	Loading stage				Unloading stage			
	radial stress		hoop stress		radial stress		hoop stress	
	FEM	ANLYT	FEM	ANLYT	FEM	ANLYT	FEM	ANLYT
6	-372	-374	452	452	-25	-26	-27	-28
7	-255	-257	398	400	-18	-19	29	29
8	-178	-180	321	323	-13	-13	23	24
9	-125	-127	268	270	-9	-9	19	20
10	-88	-89	231	232	-6	-7	17	17
11	-60	-61	203	204	-4	-5	15	15
12	-39	-40	182	183	-3	-3	13	13
13	-23	-24	165	167	-2	-2	12	12
14	-10	-11	152	154	-1	-1	11	11
15	0	0	143	143	0	0	10	10

CHAPTER 5

RESULTS AND DISCUSSION

5.1 Introduction

In this chapter, the results obtained from both experimental and numerical studies are presented. Strain gauge and x-ray residual stress measurement results are given and influence of pressure holding time on strain generation is discussed. Distributions for all stress components along the thickness of the cylinder in both loading and unloading stages are evaluated. Experimental and numerical results are compared to each other. Coherent results are obtained.

5.2 Experimental Results

5.2.1 Strain Gauge Results

Test reports illustrated in Chapter 4 are schematically drawn in Figure 5.1 to represent the stages of a hydraulic autofrettage process which may be divided into 5 as adaptation filling, pressure increasing (loading), pressure holding, pressure decreasing, purging and unloading. In the experiments, pressure increasing, pressure decreasing and pressure holding time were set to 10, 10, and 120s respectively on the bench; thus, the cycle was lasted approximately 180 seconds.

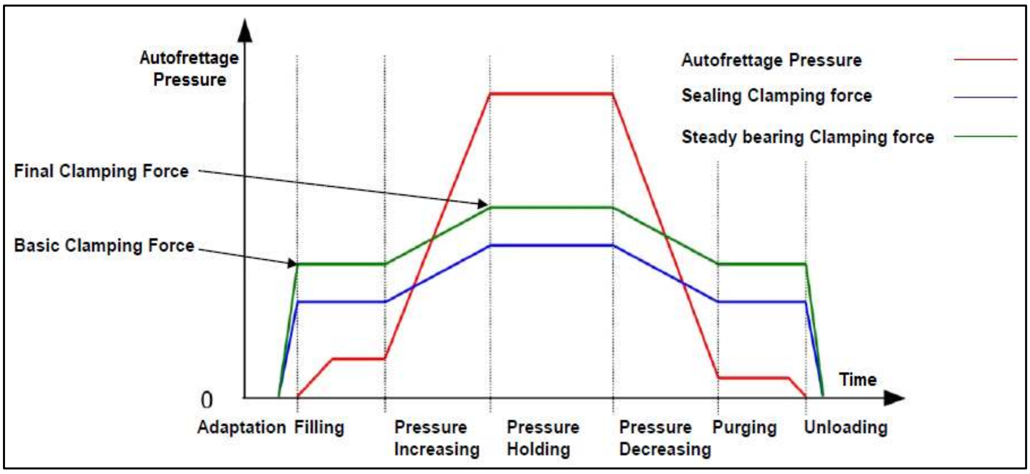

Figure 5.1 Course of a hydraulic autofrettage process [74]

Tangential and axial strains measured during the autofrettage process for each test are illustrated in Figure 5.2. In this figure, the positive values indicate the tangential strains, and the negative values indicate the axial strains. Pressure loading takes place between 25th and 35th seconds. Pressure holding starts at 35th seconds and it takes 120 seconds. Pressure is removed between 155th and 165th seconds. The strain values after 170th seconds gives the residual strains induced in the cylinder.

It is clear in the figure that, there is an increase in both tangential and axial strains with an increase in the autofrettage pressure. Both tangential and axial strains remain almost constant during the pressure holding time. Strain results in loading and unloading steps are also given in Table 5.1.

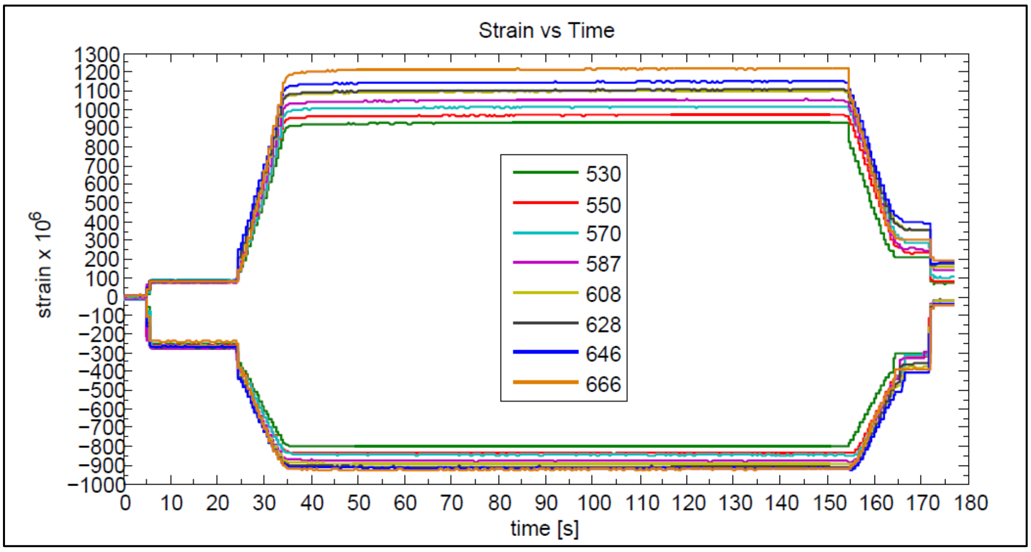

Figure 5.2 Tangential and axial strains measured during autofrettage process

Table 5.1 Experimental strain values for each autofrettage pressure

Pa (MPa)	Fc (kN)	Tangential Strain x10^6		Axial strain x 10^6	
		Loading	Unloading	Loading	Unloading
530	124	899	71	-791	-17
550	126	941	83	-825	-21
570	127	978	103	-832	-20
587	128	1018	143	-865	-23
608	130	1065	157	-880	-25
628	132	1072	175	-895	-37
646	133	1115	182	-903	-39
666	134	1167	193	-910	-47

In many industrial applications, pressure holding time is generally taken up to 20 seconds. This may be even shorter in mass production. For example, common rails are held at the autofrettage pressure for only 2-3 seconds. Figure 5.3 represents tangential strain values during the first 20 seconds of pressure holding time. It is seen in the figure that, hoop strains become almost constant after 3-6 seconds depending on the autofrettage pressure. As the autofrettage pressure increases, required time for desired strain generation increases. After 6 seconds, there is a small change in tangential strain values which may not create any significant effect in residual stress generation. Consequently, pressure holding time should be increased a little more in mass production especially for higher autofrettage pressure values.

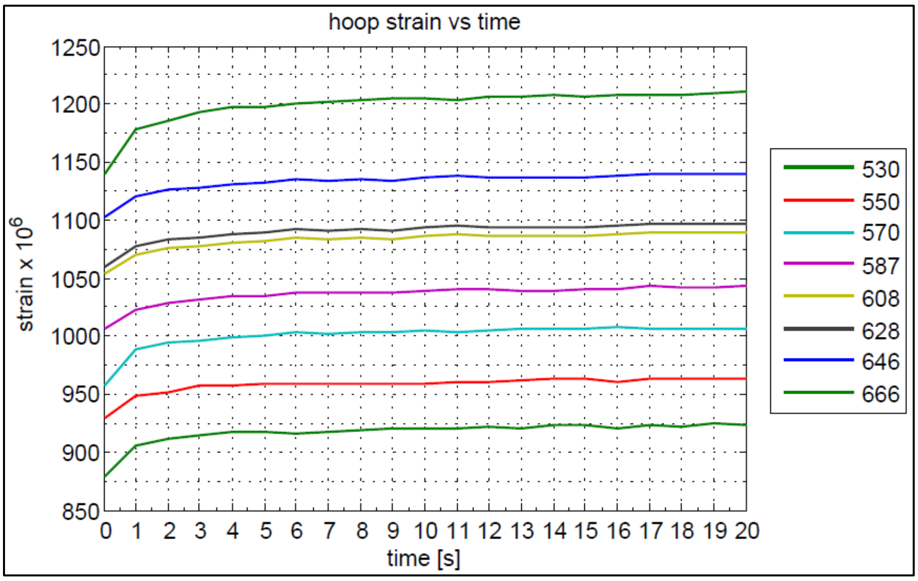

Figure 5.3 Tangential strain distributions during the first 20s of pressure holding time

5.2.2 XRD Residual Stress Results

Residual stress results at the points selected on a certain path from inner wall to outer surface as illustrated in Figure 4.27 are given in Tables 5.2 and 5.3 for radial and tangential stress respectively. Tangential stresses are of compressive type at the inner surface and become tensile after passing the interface. Tangential stress values at the second measurement points are positive for the samples autofrettaged under 530 and 550 MPa pressure. This indicates that, the interface is near to this point. The values become positive after the 2nd measurement points for higher autofrettage pressures that confirm increase in the plastic region with respect to autofrettage pressures. Radial stresses are all compressive type and decrease as moved from inner to outer surface and approaching zero as expected. Additionally, both tangential and radial stress values increase with an increase in the autofrettage pressure.

Table 5.2 Residual radial stress results

Pa [MPa]	**Measurement Points**				
	1 (5-6 mm)	**2** (6-7 mm)	**3** (7-8 mm)	**4** (10-11 mm)	**5** (12-13 mm)
530	-23,8	-31,3	-24,2	-13,3	-0,1
550	-29,8	-28,6	-28,3	-10,6	-3
570	-26,4	-42,5	-22,1	-12,0	-2,7
587	-37,7	-32,3	-36,1	-15,8	-2,8
608	-41,0	-53,3	-31,1	-15,3	-8,8
628	-43,9	-48,2	-40,5	-14,7	-7,3
646	-53,3	-63,6	-52,3	-20,0	-9,3
666	-55,9	-63,9	-51,9	-19,6	-10,2

Table 5.3 Residual tangential stress results

Pa [MPa]	**Measurement Points**				
	1 (5-6 mm)	**2** (6-7 mm)	**3** (7-8 mm)	**4** (10-11 mm)	**5** (12-13 mm)
530	-86,4	30,0	36,3	31,3	9,3
550	-96,9	1,5	56,6	24,6	27,4
570	-122,2	-74,9	4,3	55,1	37,5
587	-161,2	-100,9	8,7	48,6	30,4
608	-203,8	-103,3	8,5	41,8	23,9
628	-156,5	-100,2	3,0	67,1	25,2
646	-210,3	-123,6	5,3	60,2	53,2
666	-206,2	-146,9	1,3	72,0	67,7

5.3 FEM Results

The FE analysis results are given graphically for each autofrettage pressure in Figures 5.4 to 5.19. It is seen in the figures that, the maximum stress at the inner wall of the cylinder in the loading stage is the radial stress. This stress is of compressive type and it is almost equal to the autofrettage pressure. Coversely, the maximum residual stress at the same place is the tangential stress. All the residual stress components at the inner wall are compressive stresses, except for the radial stress which is zero. There is an increase in the stress components in both loading and unloading steps with an increase in the autofrettage pressure, however, a slight decrease is seen in the tangential stress values at the inner wall in the loading stage. The plastic region incerases with an increase in the autofrettage pressure which is resulted as an increase in the residual compressive stress at both the inner wall and the elastic-plastic interface. The amount of increase in the elastic-plastic interface radius with respect to autofrettage pressure is appoximately 0.01 mm/MPa.

In the loading step, the radial stress decreases and becomes zero; hoop stress increases and reaches the highest value at the interface and then decreases; axial stress decreases a little and remains almost constant and Von Misses stress decreases from inner wall to the outer surface. In case of unloading step, the axial and tangential stresses are highest at the inner wall, then they increase in the positive direction and reach the highest positive value at the interface and then the axial stress remains constant an the tangential stress decreases a little towards the outer surface. Radial stress is zero at the inner wall, reaches the highest negative value at the interface, and becomes zero again at the outer surface. Von-mises stress is maximum at the inner wall, decreases towards the interface, and then increases a little at the interface. After interface it decreases again towards the outer surface.

Von Mises stresses in the loading and unloading steps vary between 775.8 to 831.3 MPa and 267.1 to 476.4 MPa respectively depending on the autofrettage pressure. The maximum Von Misses stress is developed at the inner wall of the cylinder for both loading and unloading steps. For maximum autofrettage pressure (666 MPa), the maximum Von-Mises stress in the loading step is 831.3 MPa which is smaller than the ultimate tensile strength of the material (Sut=1000 MPa). Also, when the load is removed (unloading step) the maximum Von Misses stress is 476.4 MPa which is smaller than the yield strength of the material (Sy=700 MPa).

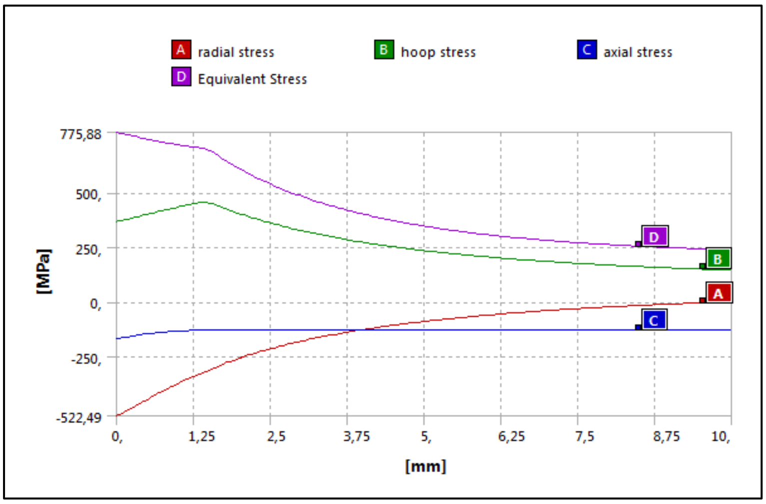

Figure 5.4 Stress distributions for loading step (Pa=530 MPa)

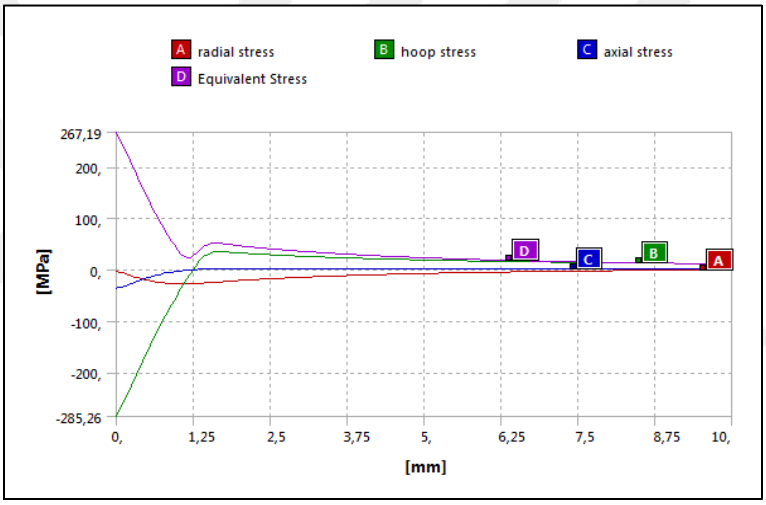

Figure 5.5 Stress distributions for unloading step (Pa=530 MPa)

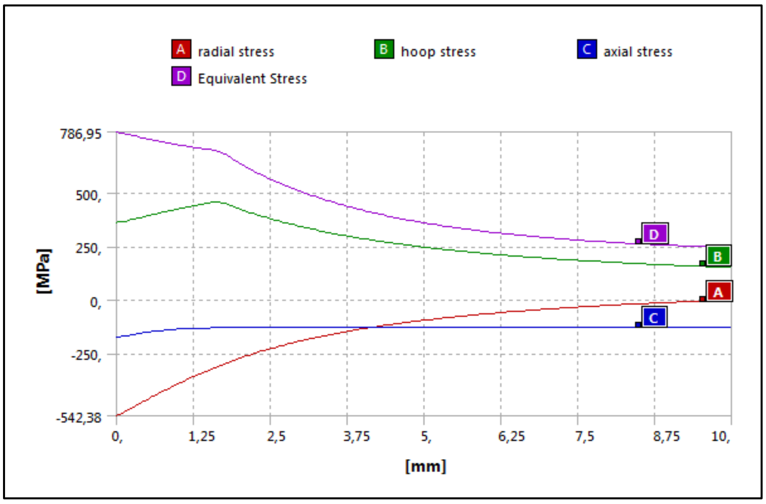

Figure 5.6 Stress distributions for loading step (Pa=550 MPa)

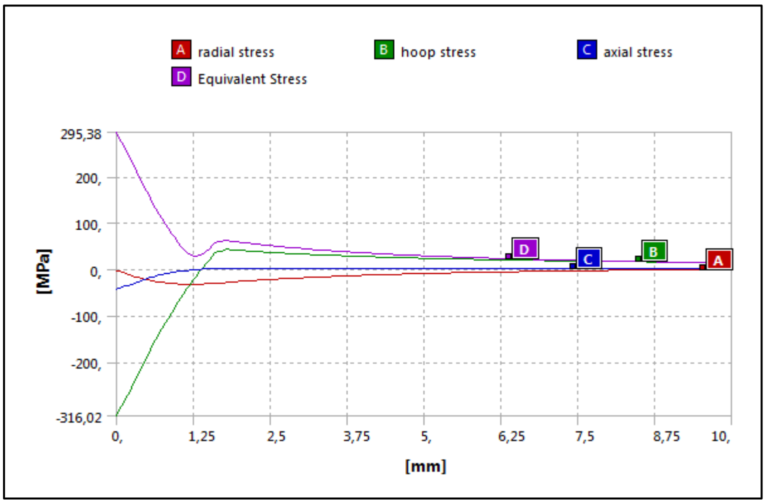

Figure 5.7 Stress distributions for unloading step (Pa=550 MPa)

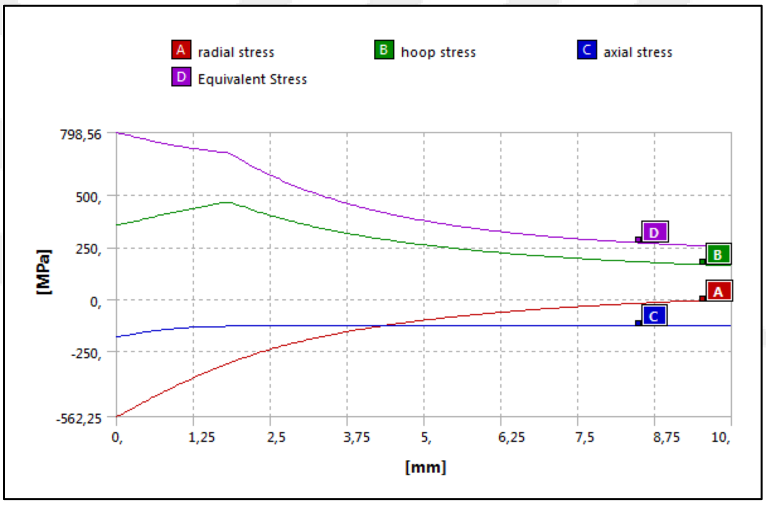

Figure 5.8 Stress distributions for loading step (Pa=570 MPa)

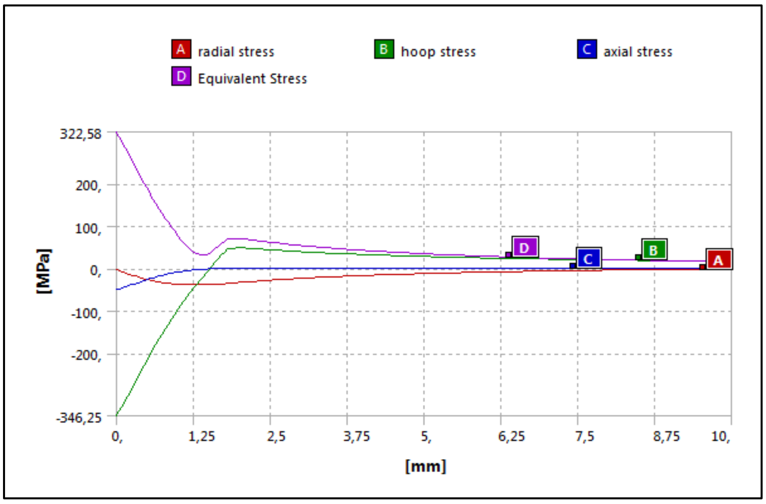

Figure 5.9 Stress distributions for unloading step (Pa=570 MPa)

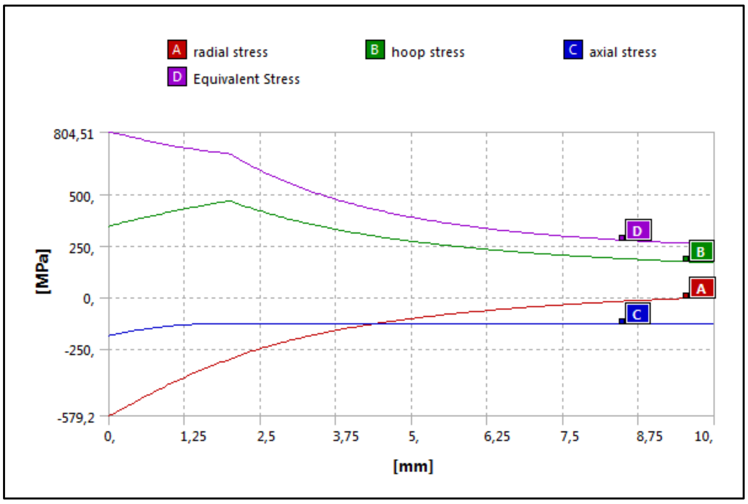

Figure 5.10 Stress distributions for loading step (Pa=587 MPa)

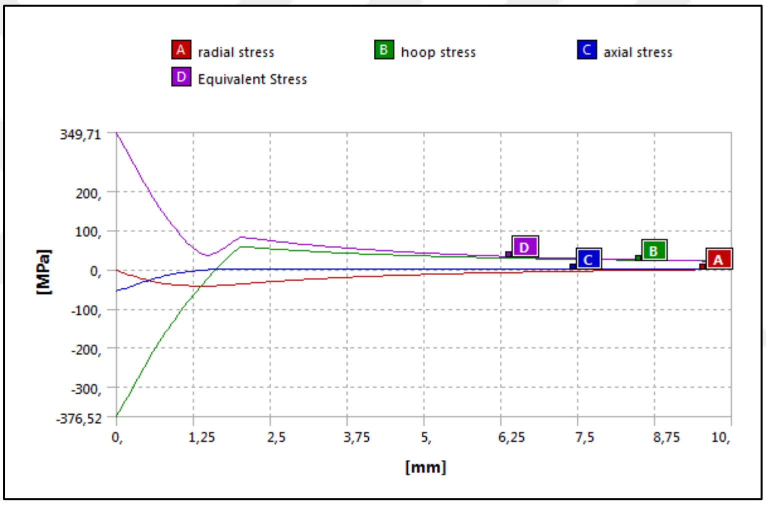

Figure 5.11 Stress distributions for unloading step (Pa=587 MPa)

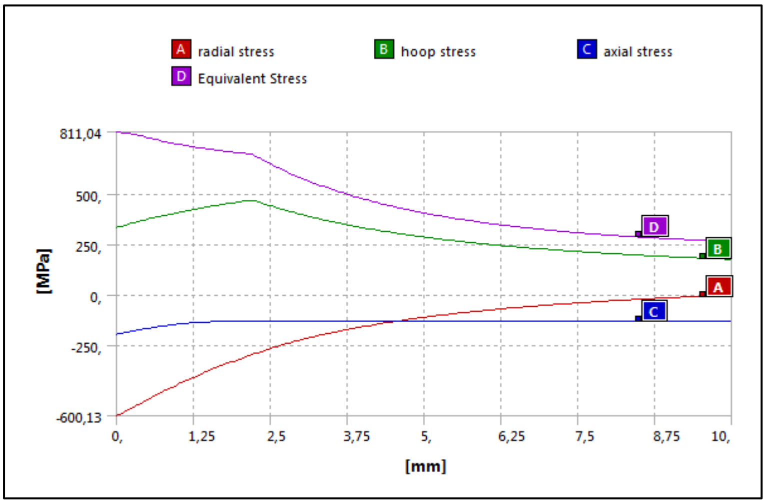

Figure 5.12 Stress distributions for loading step (Pa=608 MPa)

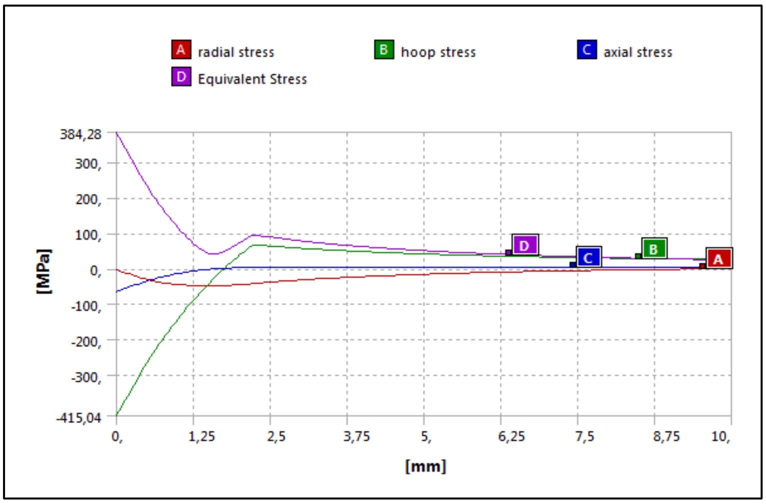

Figure 5.13 Stress distributions for unloading step (Pa=608 MPa)

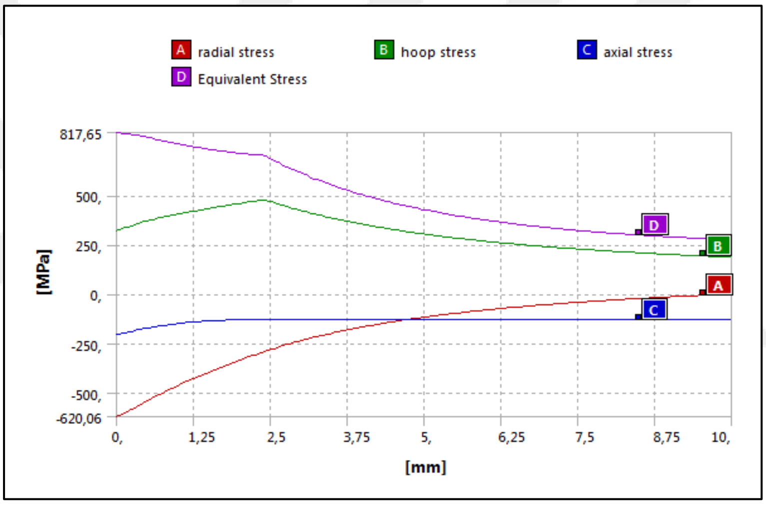

Figure 5.14 Stress distributions for loading step (Pa=628 MPa)

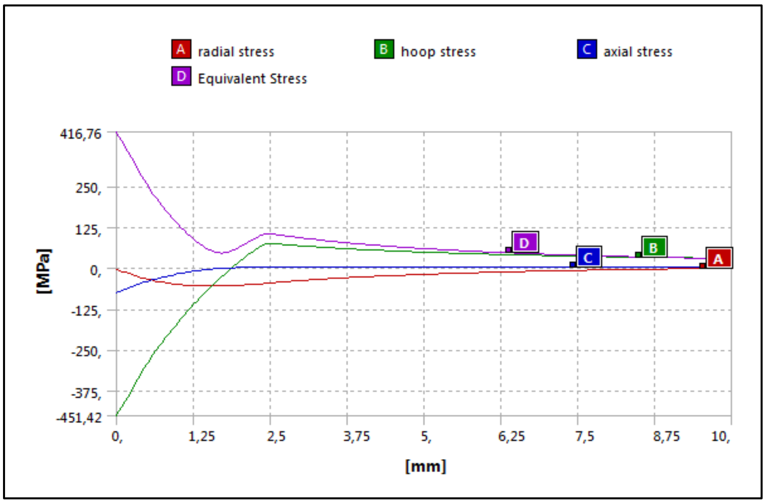

Figure 5.15 Stress distributions for unloading step (Pa=628 MPa)

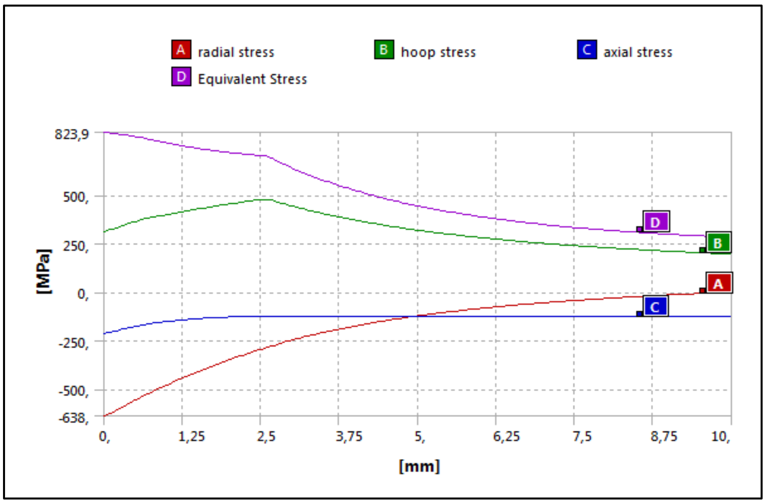

Figure 5.16 Stress distributions for loading step (Pa=646 MPa)

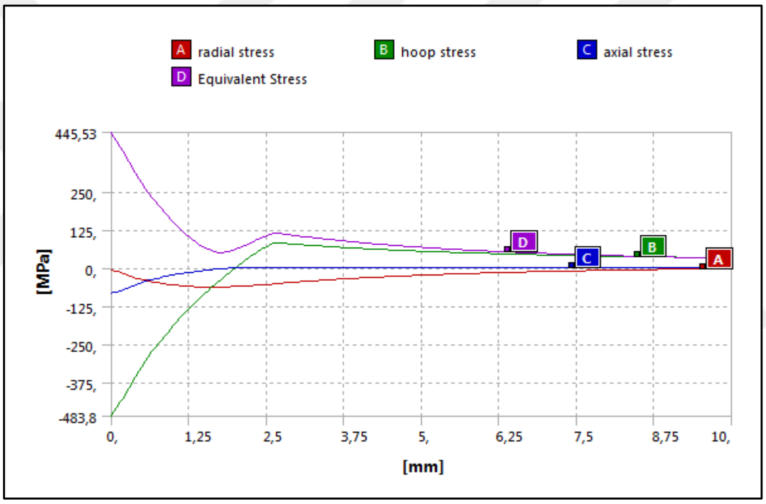

Figure 5.17 Stress distributions for unloading step (Pa=646 MPa)

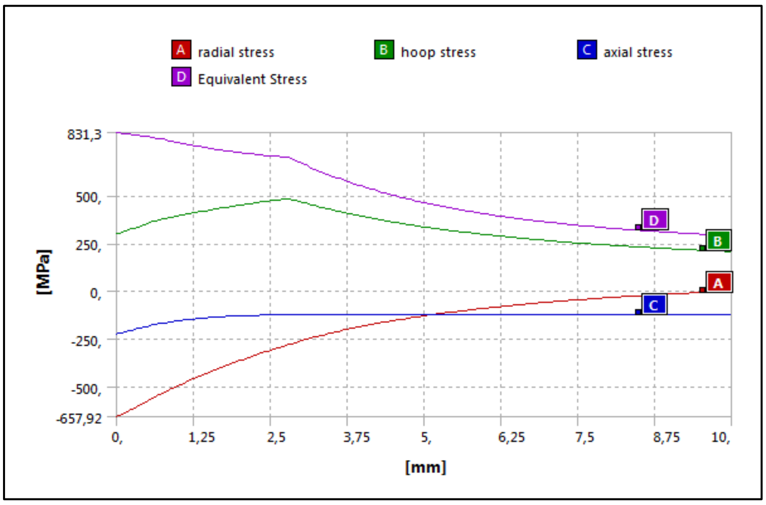

Figure 5.18 Stress distributions for loading step (Pa=666 MPa)

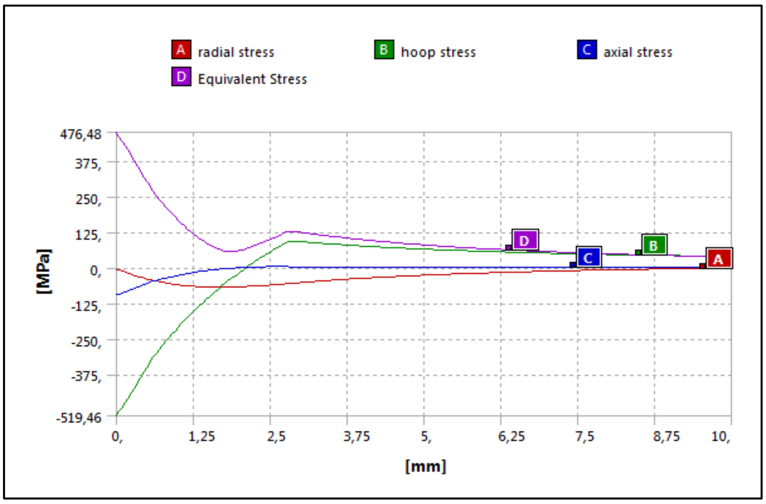

Figure 5.19 Stress distributions for unloading step (Pa=666 MPa)

In addition to the stress distribution plots, screenshot views (taken from ANSYS Workbench) of each stress components in both loading and unloading steps for maximum autofrettage pressure (666 MPa) are given in Figures 5.20 to 5.27. Since the length of the cylinder is too long, only about the quarter of the total geometry is represented in these figures.

It is seen in the figures that, the maximum equivalent stress (Von-Mises) occurs at the cylinder-fixture contact surface and there is a stress fluctuation near this region due to the effect of the clamping force. The stress distributions are getting constant and vary only depending on the thickness as moving down from this region towards the center of the cylinder.

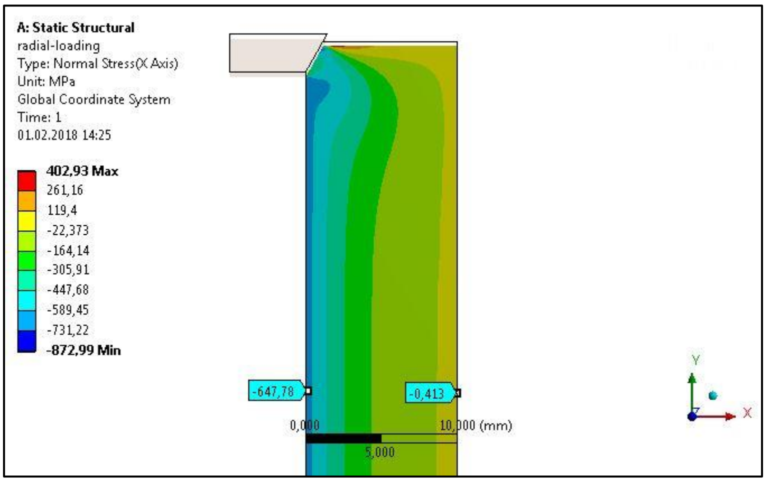

Figure 5.20 Radial stress distribution in loading step (Pa=666 MPa)

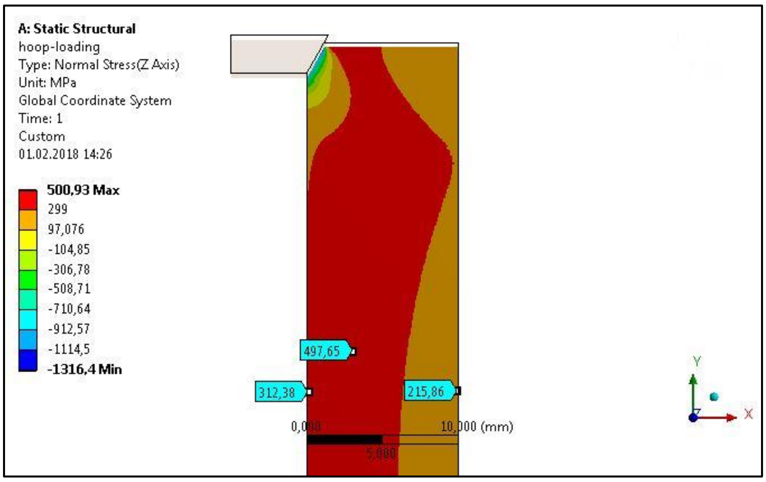

Figure 5.21 Hoop stress distribution in loading step (Pa=666 MPa)

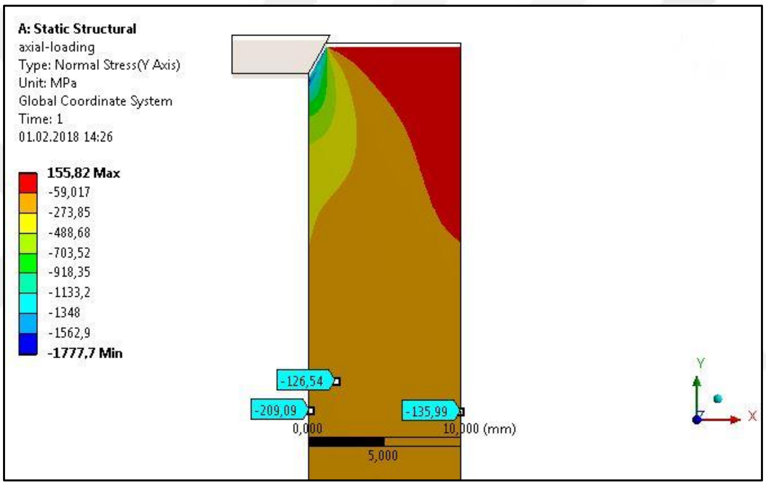

Figure 5.22 Axial stress distribution in loading step (Pa=666 MPa)

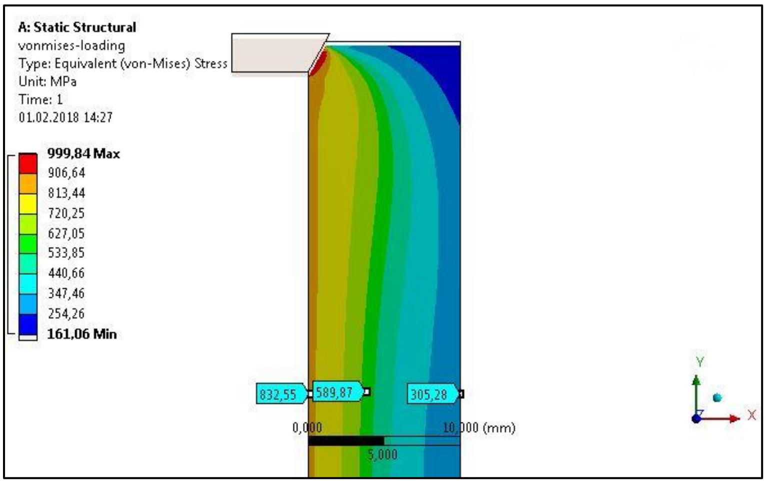

Figure 5.23 Von-Mises stress distribution in loading step (Pa=666 MPa)

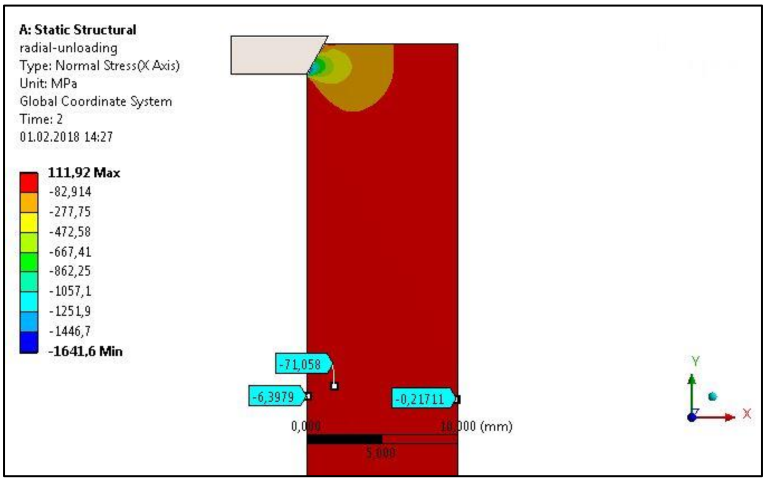

Figure 5.24 Radial stress distribution in unloading step (Pa=666 MPa)

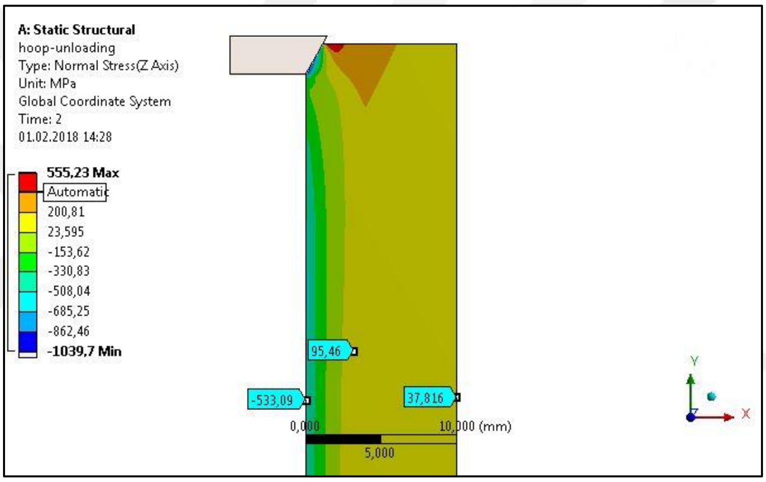

Figure 5.25 Hoop stress distribution in unloading step (Pa=666 MPa)

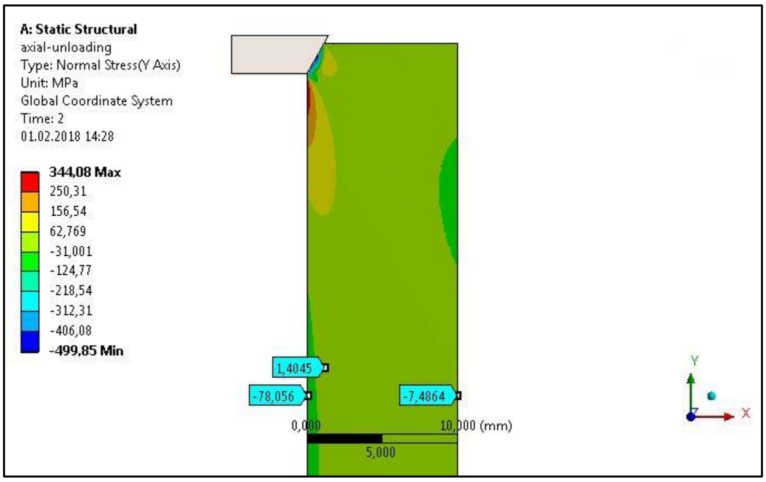

Figure 5.26 Axial stress distribution in unloading step (Pa=666 MPa)

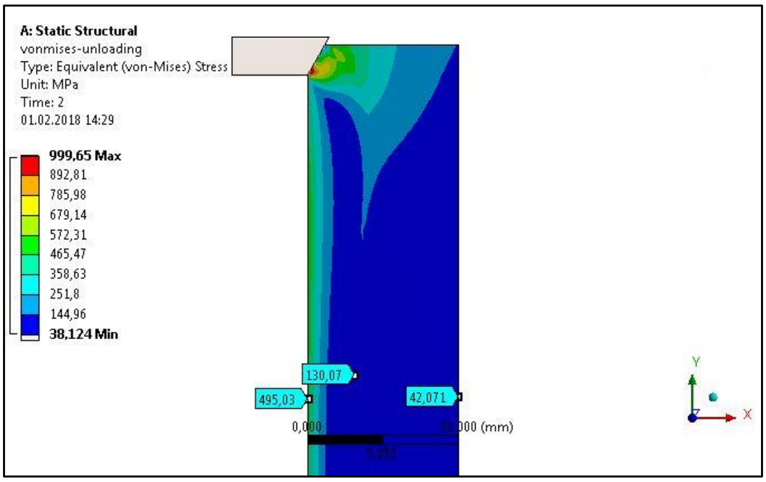

Figure 5.27 Von-Mises stress distribution in unloading step (Pa=666 MPa)

The elastic-plastic interface radius (b) is an important parameter used in the design process. When an autofrettaged cylinder is subjected to operating pressure, the maximum equivalent stress occurs at the interface radius. Also, the interface radius indicates how much of the material is undergoing plastic deformation after autofrettage operation. The interface radii determined for each autofrettage pressure are given in Table 5.4. It is also seen in this table that about 13% to 28% of the thickness of the material is undergone plastic deformation.

Table 5.4 Elastic-plastic interface radius

Autof. Pressure [MPa]	**530**	**550**	**570**	**587**	**608**	**628**	**646**	**666**
Clamping Force [kN]	**124**	**126**	**127**	**128**	**130**	**132**	**133**	**134**
Interface radius [mm]	6.42	6.62	6.83	7.00	7.20	7.41	7.59	7.81

In this study, dimensions of the samples are determined to be similar to the dimensions of fuel rails used in diesel engines. Injection pressures used by the automotive companies are in the range of about 140-200 MPa. Therefore, the working pressure is considered as 200 MPa and the stress distributions under this pressure are evaluated. Figures 5.28 to 5.30 illustrate all stress components for the cylinders autofrettaged under 530 (the lowest), 587 and 666 (the highest) MPa pressure. It is seen in the figures that the maximum Von-Misses stress occurs at the elastic-plastic interface while it does at the inner surface for non-autofrettaged (denoted by “NA” in the table) cylinder. The maximum stress values for each autofrettage pressure as well as for non-autofrettaged cylinder are also given in Table 5.5. Minimum stress value is obtained for 587 MPa autofrettage pressure as 279.5 MPa among all the autofrettage conditions considered and it is approximately 110.7

MPa less than non-autofrettaged cylinder which is calculated from the Lâme equations as 389.7 MPa.

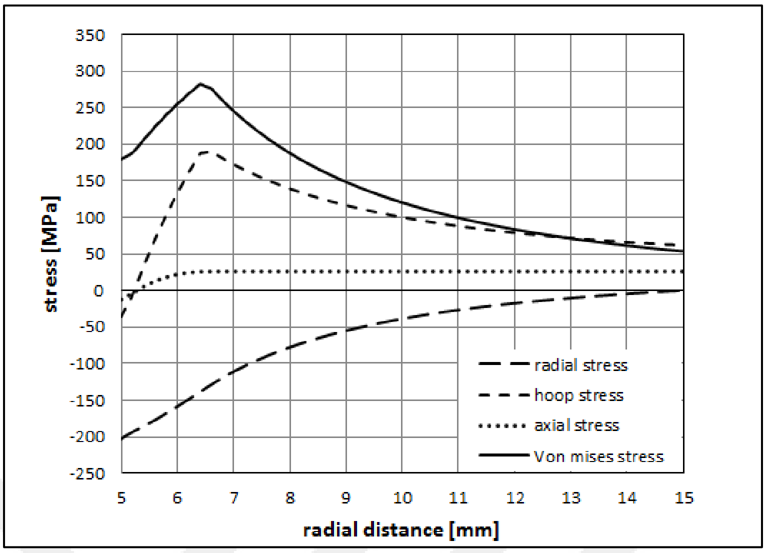

Figure 5.28 Stress distributions under 200 MPa working pressure (Pa=530 MPa)

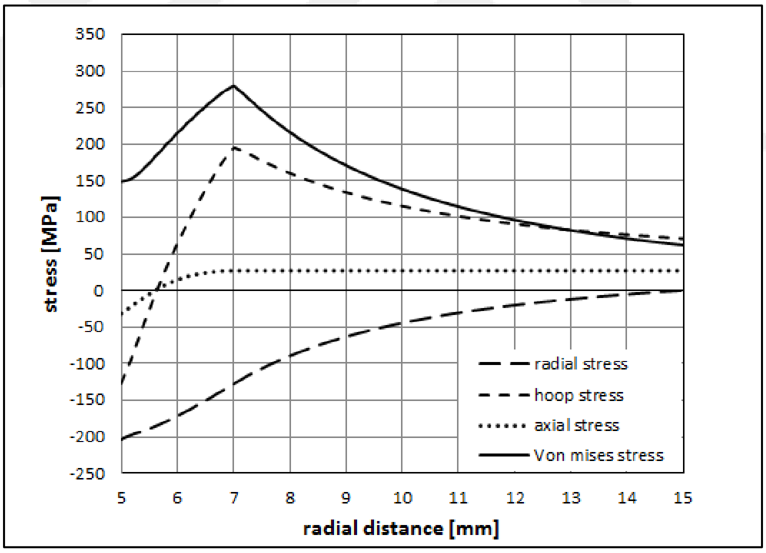

Figure 5.29 Stress distributions under 200 MPa working pressure (Pa=587 MPa)

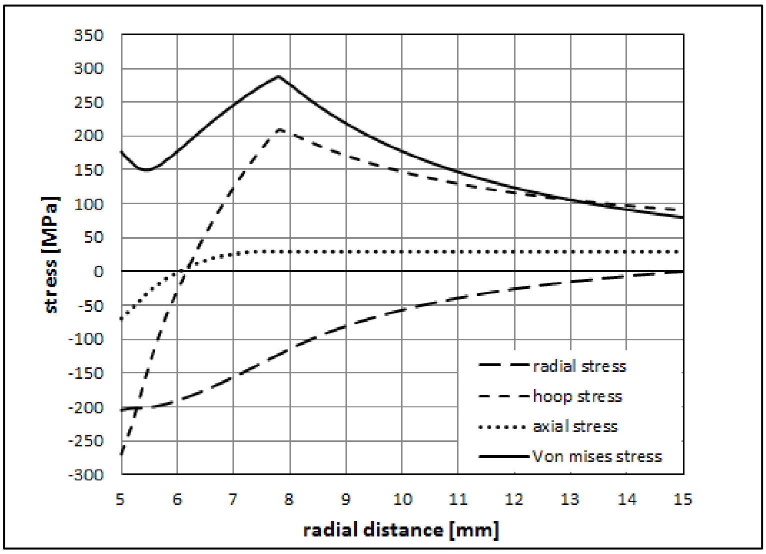

Figure 5.30 Stress distributions under 200 MPa working pressure (Pa=666 MPa)

Table 5.5 Elastic-plastic interface radius

Pa [MPa]	NA	530	550	570	***587***	608	628	646	666
Max. Von-Misses stress [MPa]	389	281	280	280	***279***	280	282	284	287

Strain results for loading stage are illustrated in Figures 5.31 to 5.39 for each autofrettage pressure. Radial and axial strains are of compressive type while tangential strain is of tension type. Radial and tangential strains are maximum at the inner surface and decreasing towards to the outer surface. Axial strain is increasing up to the elastic-plastic interface and then remains constant. At the inner wall, radial strains are increasing; tangential strains are increasing up to 570 MPa pressure then they are decreasing and axial strains are decreasing with an increase in the autofrettage pressure. Also, all the strain components at the outer surface are increasing with respect to autofrettage pressure. Maximum strain in the loading stage is the radial strain and occurs at the inner wall of the cylinder.

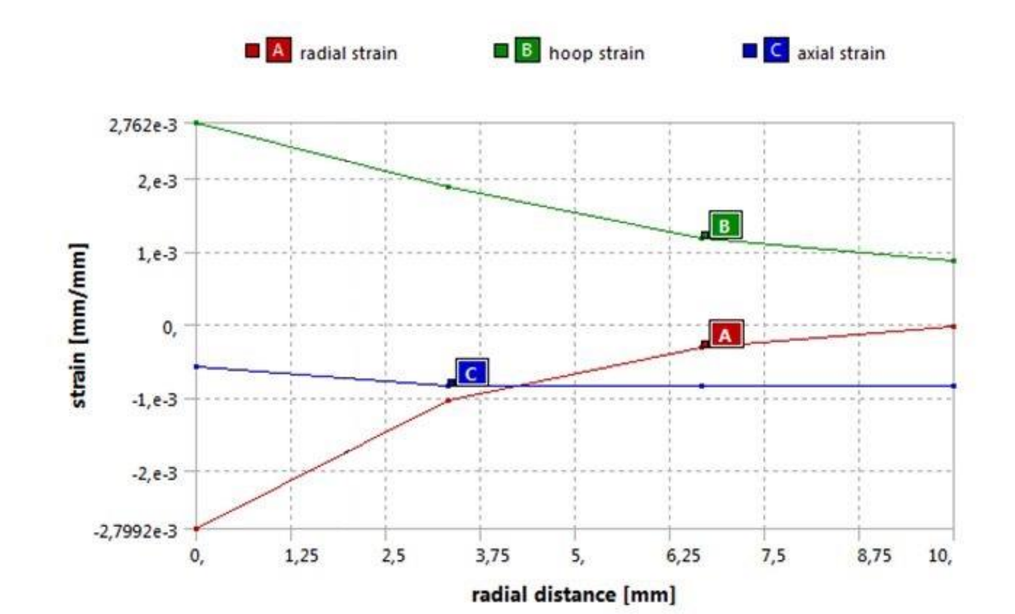

Length [mm]	[A] radial strain [mm/mm]	[B] hoop strain [mm/mm]	[C] axial strain [mm/mm]
0,	-2,7992e-003	2,762e-003	-5,8464e-004
3,3333	-1,0298e-003	1,8902e-003	-8,333e-004
6,6667	-3,1464e-004	1,1751e-003	-8,3331e-004
10,	-2,0312e-005	8,8076e-004	

Figure 5.31 Strain results in loading stage (Pa=530 MPa)

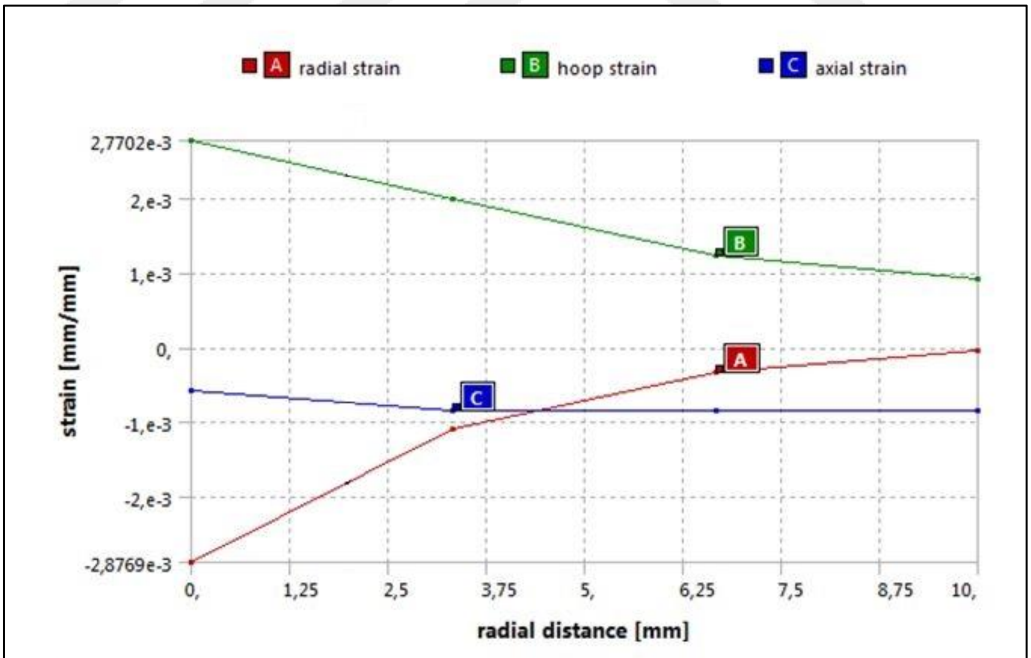

Length [mm]	[A] radial strain [mm/mm]	[B] hoop strain [mm/mm]	[C] axial strain [mm/mm]
0,	-2,8769e-003	2,7702e-003	-5,7728e-004
3,3333	-1,0962e-003	1,9845e-003	-8,4666e-004
6,6667	-3,4169e-004	1,23e-003	
10,	-3,1173e-005	9,1946e-004	

Figure 5.32 Strain results in loading stage (Pa=550 MPa)

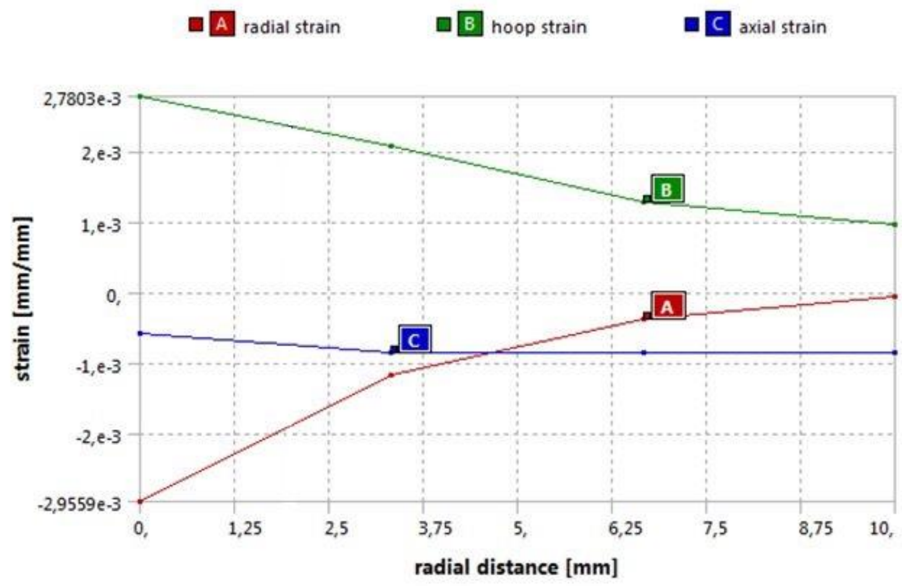

Length [mm]	[A] radial strain [mm/mm]	[B] hoop strain [mm/mm]	[C] axial strain [mm/mm]
0,	-2,9559e-003	2,7803e-003	-5,6864e-004
3,3333	-1,1679e-003	2,0804e-003	-8,5251e-004
6,6667	-3,7235e-004	1,2848e-003	
10,	-4,4934e-005	9,5742e-004	-8,5252e-004

Figure 5.33 Strain results in loading stage (Pa=570 MPa)

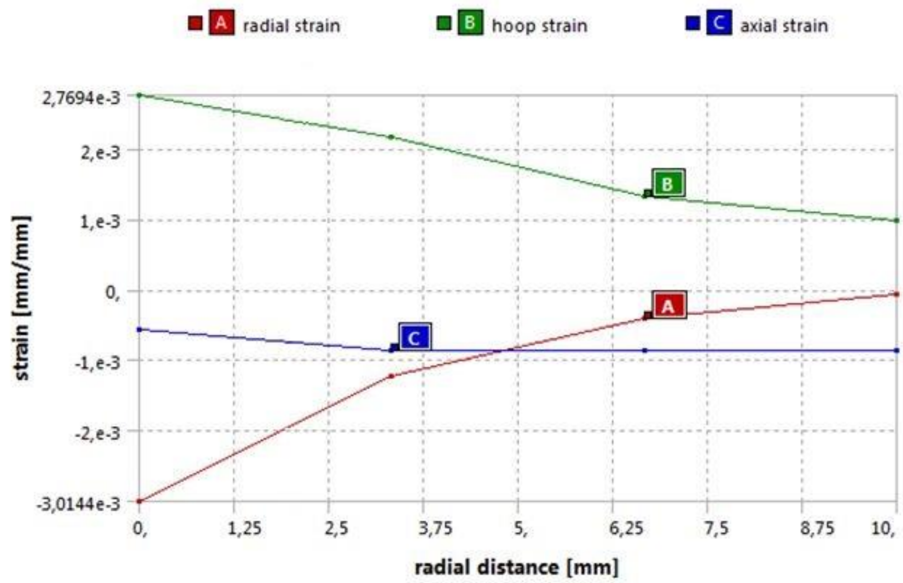

Length [mm]	[A] radial strain [mm/mm]	[B] hoop strain [mm/mm]	[C] axial strain [mm/mm]
0,	-3,0144e-003	2,7694e-003	-5,6234e-004
3,3333	-1,2316e-003	2,1665e-003	-8,5897e-004
6,6667	-3,9939e-004	1,3342e-003	
10,	-5,687e-005	9,9173e-004	

Figure 5.34 Strain results in loading stage (Pa=587 MPa)

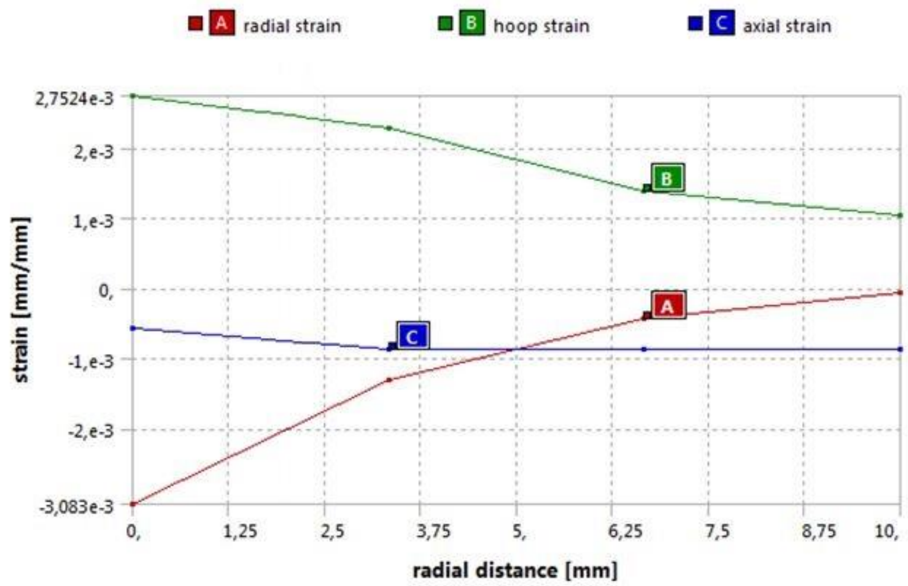

Length [mm]	[A] radial strain [mm/mm]	[B] hoop strain [mm/mm]	[C] axial strain [mm/mm]
0,	-3,083e-003	2,7524e-003	-5,598e-004
3,3333	-1,313e-003	2,2806e-003	
6,6667	-4,3286e-004	1,4005e-003	-8,7337e-004
10,	-7,0641e-005	1,0383e-003	

Figure 5.35 Strain results in loading stage (Pa=608 MPa)

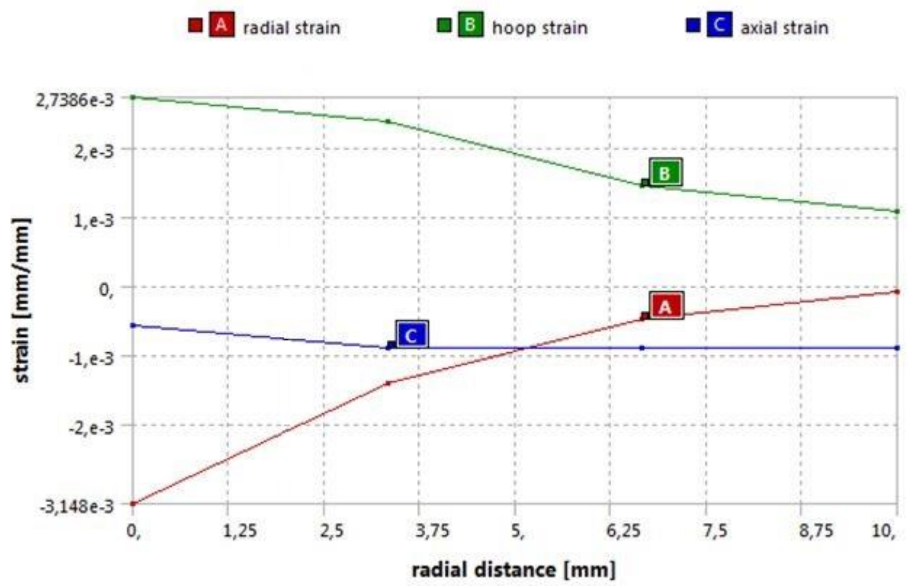

Length [mm]	[A] radial strain [mm/mm]	[B] hoop strain [mm/mm]	[C] axial strain [mm/mm]
0,	-3,148e-003	2,7386e-003	-5,6055e-004
3,3333	-1,3949e-003	2,3958e-003	
6,6667	-4,665e-004	1,4674e-003	-8,8833e-004
10,	-8,4406e-005	1,0853e-003	

Figure 5.36 Strain results in loading stage (Pa=628 MPa)

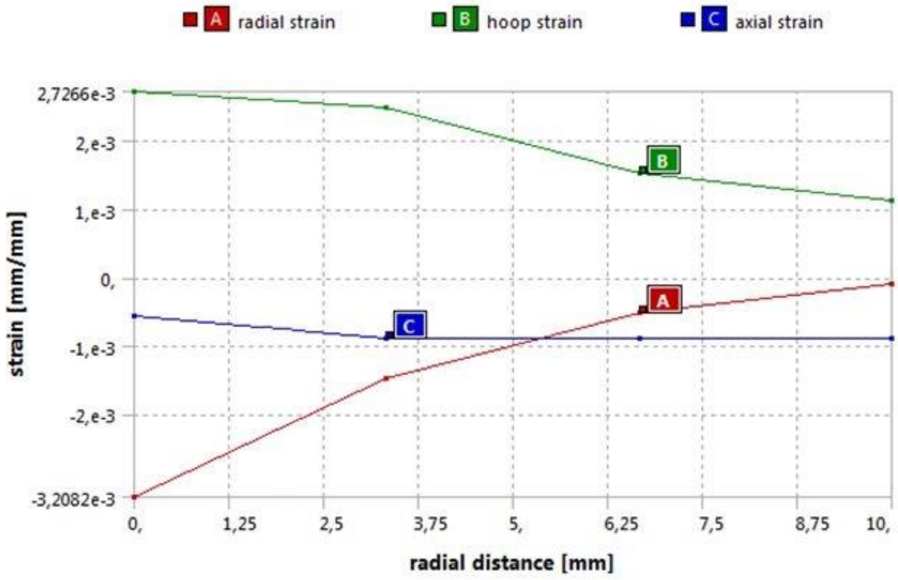

Length [mm]	[A] radial strain [mm/mm]	[B] hoop strain [mm/mm]	[C] axial strain [mm/mm]
0,	-3,2082e-003	2,7266e-003	-5,5742e-004
3,3333	-1,4743e-003	2,5029e-003	-8,961e-004
6,6667	-5,0022e-004	1,5288e-003	
10,	-9,933e-005	1,1279e-003	-8,9611e-004

Figure 5.37 Strain results in loading stage (Pa=646 MPa)

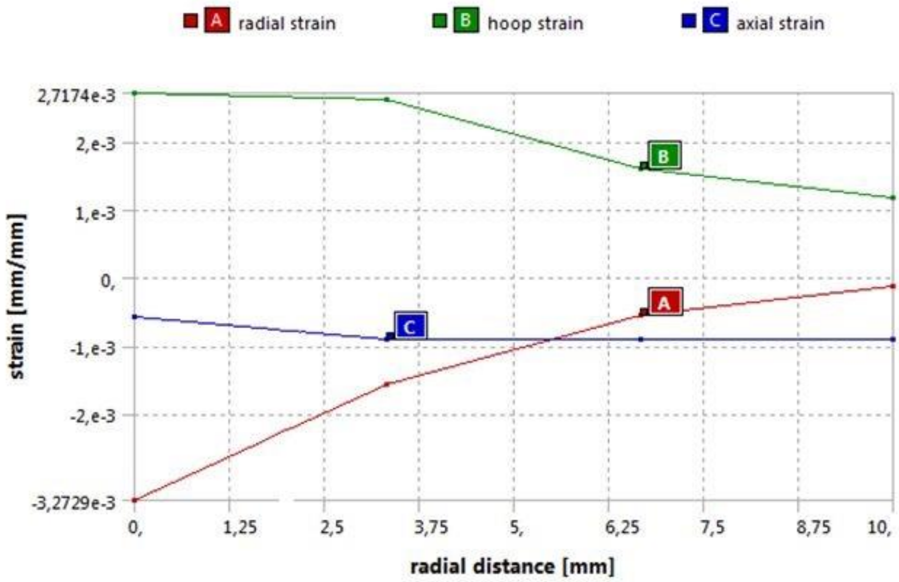

Length [mm]	[A] radial strain [mm/mm]	[B] hoop strain [mm/mm]	[C] axial strain [mm/mm]
0,	-3,2729e-003	2,7174e-003	-5,6329e-004
3,3333	-1,568e-003	2,6282e-003	-9,0369e-004
6,6667	-5,4028e-004	1,6005e-003	-9,037e-004
10,	-1,1732e-004	1,1775e-003	

Figure 5.38 Strain results in loading stage (Pa=666 MPa)

Strain results for unloading stage (residual strains) are illustrated in Figures 5.39 to 5.46 for each autofrettage pressures. All the strain components at both inner wall and outer surface are increasing with an increase in the autofrettage pressure. They are maximum at the inner wall and minimum at the outer surface. Also, tangential strain is the maximum residual strain among the all strain components. Radial strain is of tension type at the inner wall, decreasing up to elastic-plastic interface and then progressively increasing towards to outer surface. Hoop strain is of compressive type at the inner wall, decreasing up to elastic-plastic interface, becomes tension, and then decreasing towards to the outer surface. Axial strain is of tension type at the inner wall and decreasing towards to interface, becomes compressive type, and then remains constant up to the outer surface.

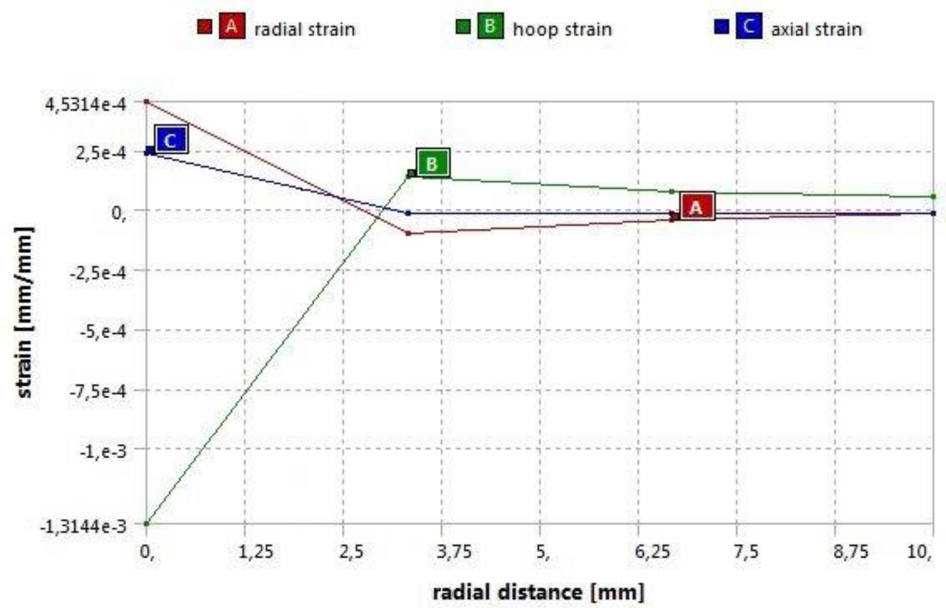

Length [mm]	[A] radial strain [mm/mm]	[B] hoop strain [mm/mm]	[C] axial strain [mm/mm]
0,	4,5314e-004	-1,3144e-003	2,3676e-004
3,3333	-1,0014e-004	1,3649e-004	-1,19e-005
6,6667	-4,2185e-005	7,8536e-005	-1,1901e-005
10,	-1,8334e-005	5,4684e-005	

Figure 5.39 Strain results in unloading stage (Pa=530 MPa)

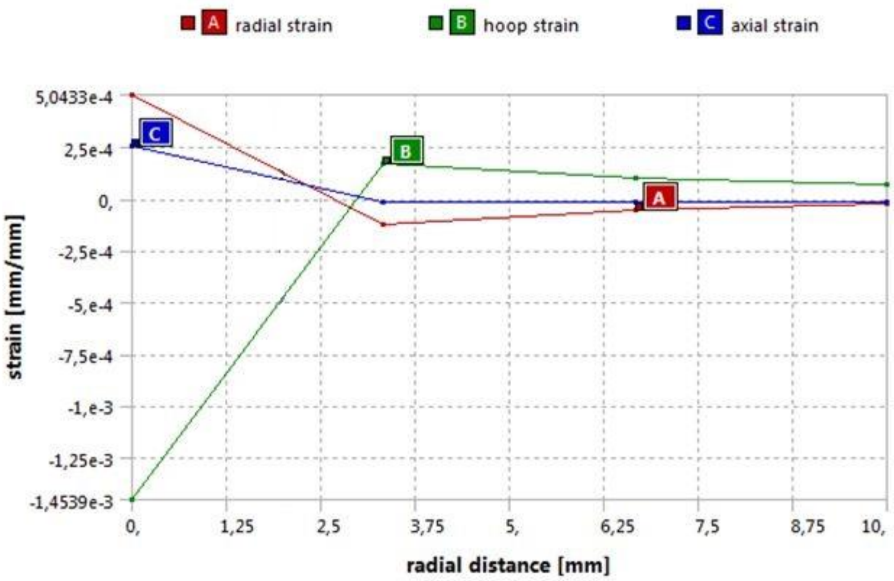

Length [mm]	[A] radial strain [mm/mm]	[B] hoop strain [mm/mm]	[C] axial strain [mm/mm]
0,	5,0433e-004	-1,4539e-003	2,5462e-004
3,3333	-1,2529e-004	1,7069e-004	-1,4761e-005
6,6667	-5,2804e-005	9,8198e-005	
10,	-2,297e-005	6,8364e-005	-1,4762e-005

Figure 5.40 Strain results in unloading stage (Pa=550 MPa)

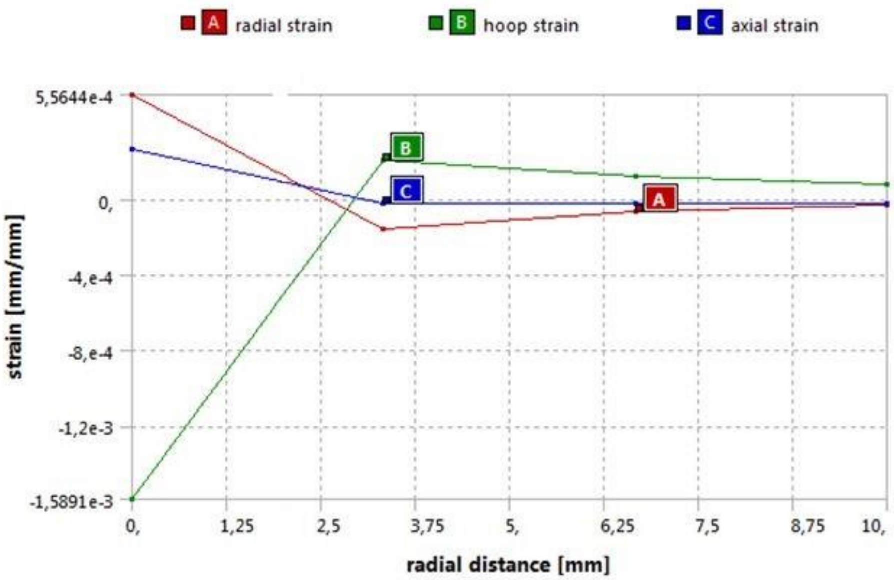

Length [mm]	[A] radial strain [mm/mm]	[B] hoop strain [mm/mm]	[C] axial strain [mm/mm]
0,	5,5644e-004	-1,5891e-003	2,6611e-004
3,3333	-1,5348e-004	2,0887e-004	-1,7769e-005
6,6667	-6,4734e-005	1,2012e-004	-1,777e-005
10,	-2,8211e-005	8,3602e-005	-1,7771e-005

Figure 5.41 Strain results in unloading stage (Pa=570 MPa)

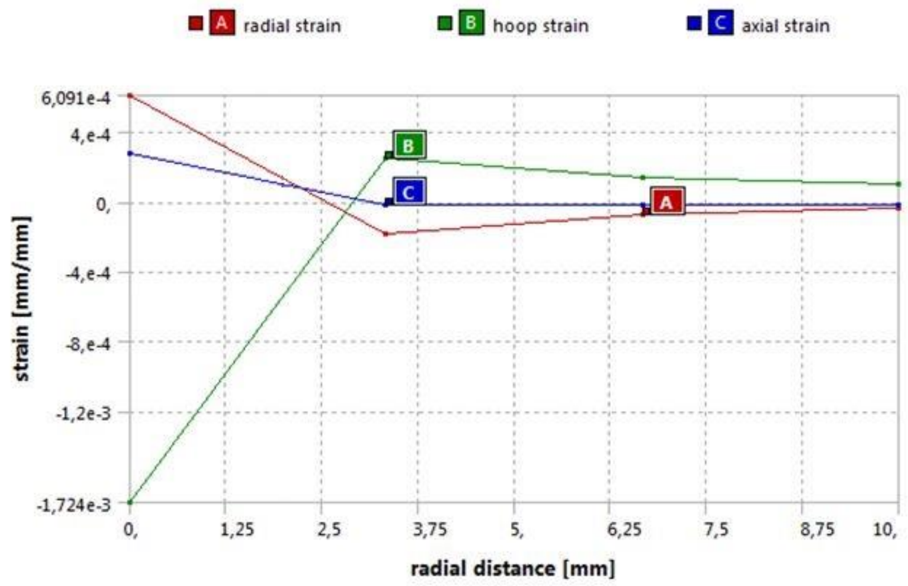

Length [mm]	[A] radial strain [mm/mm]	[B] hoop strain [mm/mm]	[C] axial strain [mm/mm]
0,	6,091e-004	-1,724e-003	2,7596e-004
3,3333	-1,8056e-004	2,4556e-004	-2,0657e-005
6,6667	-7,62e-005	1,412e-004	-2,0658e-005
10,	-3,3248e-005	9,8245e-005	-2,0659e-005

Figure 5.42 Strain results in unloading stage (Pa=587 MPa)

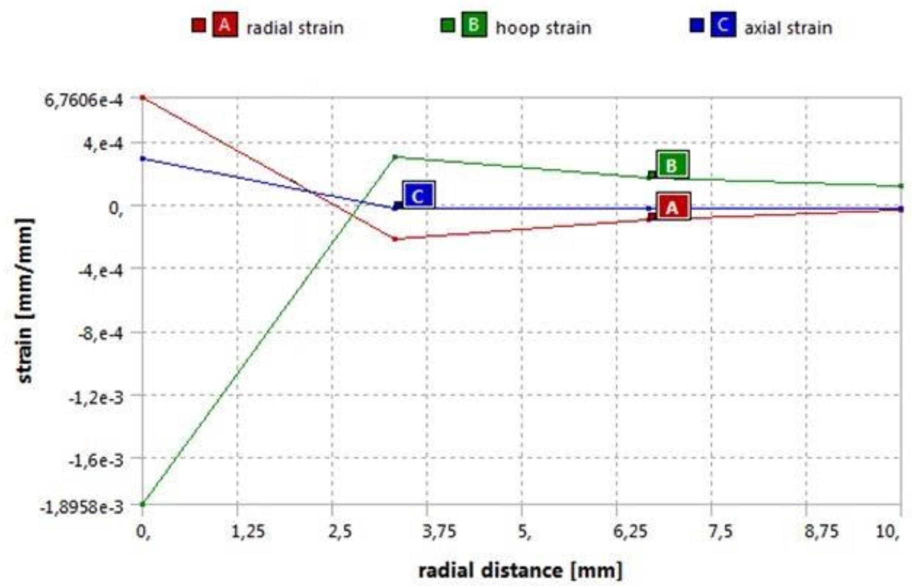

Length [mm]	[A] radial strain [mm/mm]	[B] hoop strain [mm/mm]	[C] axial strain [mm/mm]
0,	6,7606e-004	-1,8958e-003	2,8876e-004
3,3333	-2,1838e-004	2,9687e-004	-2,4807e-005
6,6667	-9,2191e-005	1,7068e-004	-2,4808e-005
10,	-4,0254e-005	1,1875e-004	-2,4809e-005

Figure 5.43 Strain results in unloading stage (Pa=608 MPa)

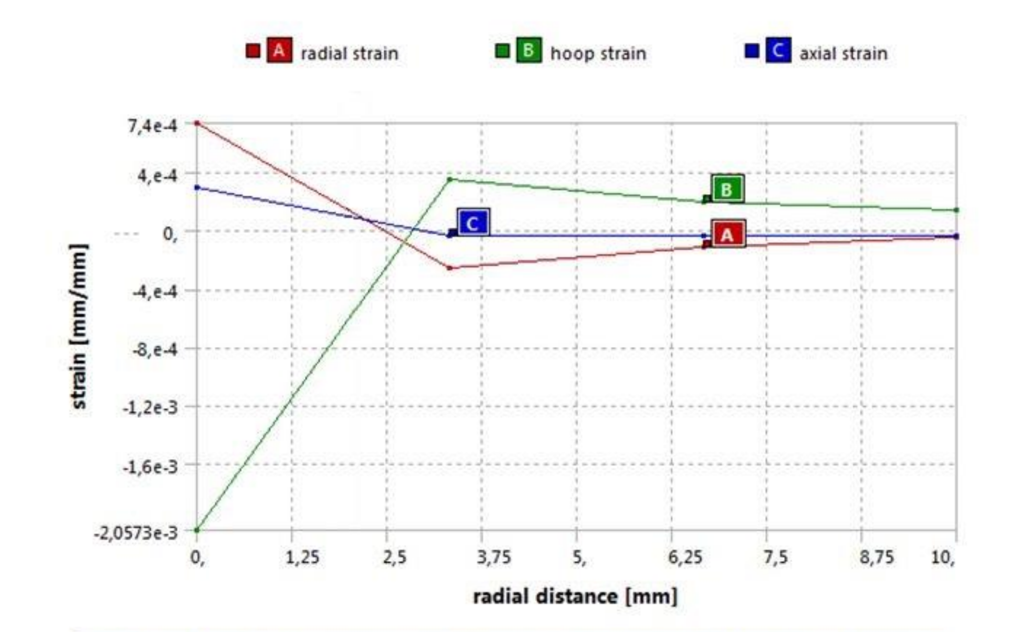

Length [mm]	[A] radial strain [mm/mm]	[B] hoop strain [mm/mm]	[C] axial strain [mm/mm]
0,	7,4e-004	-2,0573e-003	2,9851e-004
3,3333	-2,5908e-004	3,5208e-004	-2,9266e-005
6,6667	-1,094e-004	2,024e-004	-2,9268e-005
10,	-4,7794e-005	1,408e-004	-2,9269e-005

Figure 5.44 Strain results in unloading stage (Pa=628 MPa)

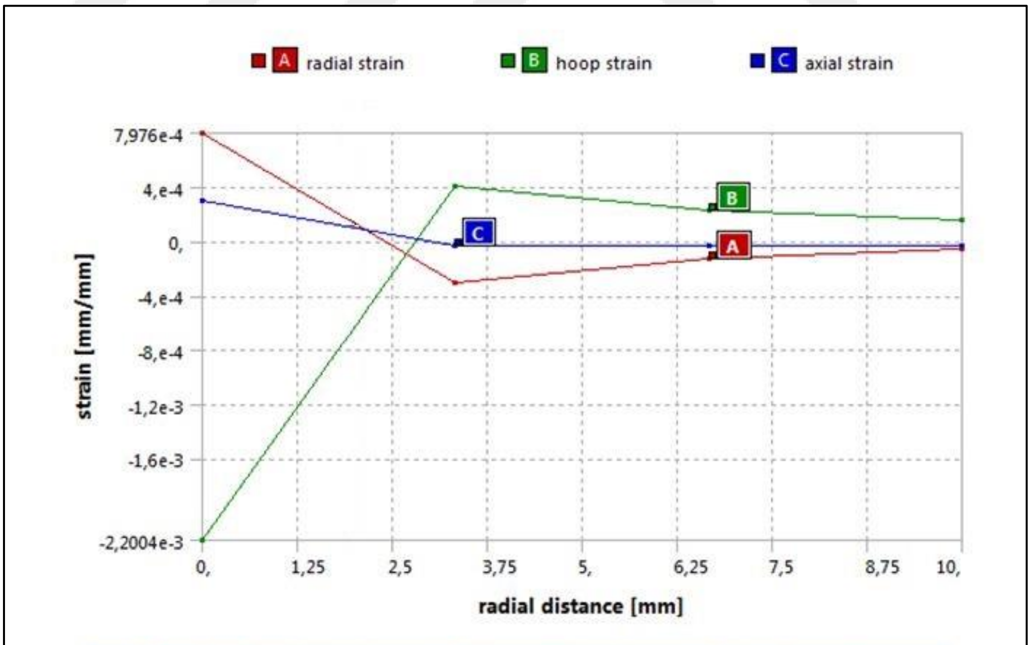

Length [mm]	[A] radial strain [mm/mm]	[B] hoop strain [mm/mm]	[C] axial strain [mm/mm]
0,	7,976e-004	-2,2004e-003	3,0496e-004
3,3333	-2,995e-004	4,0694e-004	-3,3716e-005
6,6667	-1,2649e-004	2,3392e-004	-3,3718e-005
10,	-5,5279e-005	1,6272e-004	-3,372e-005

Figure 5.45 Strain results in unloading stage (Pa=646 MPa)

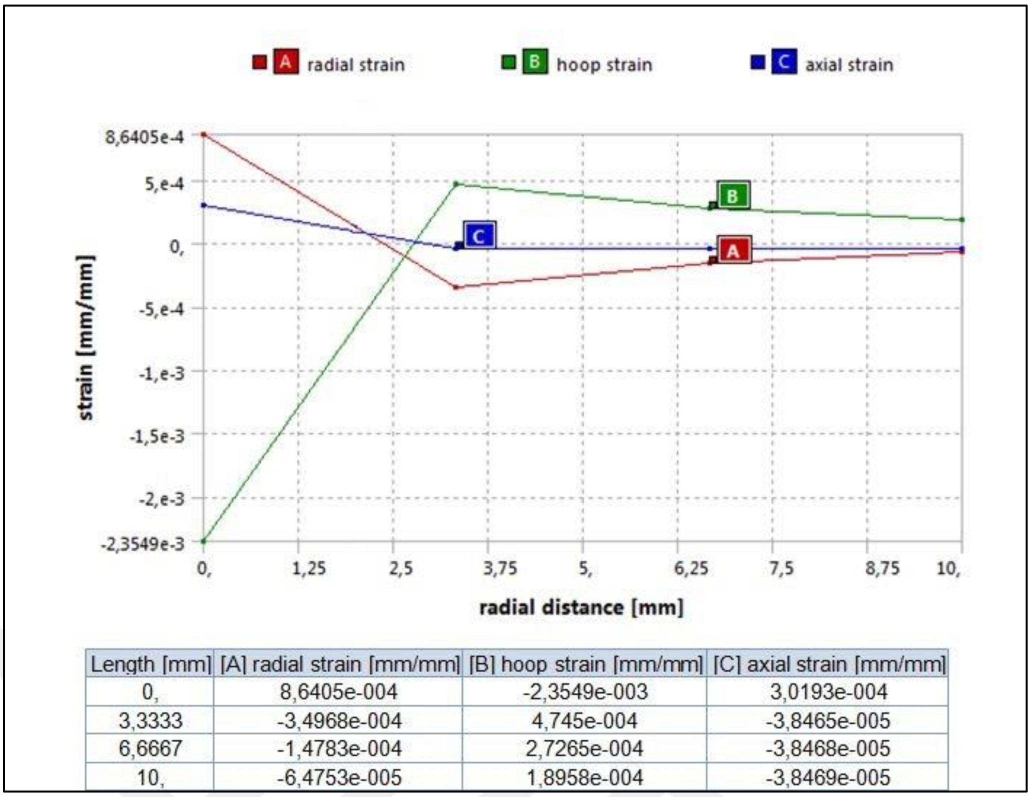

Length [mm]	[A] radial strain [mm/mm]	[B] hoop strain [mm/mm]	[C] axial strain [mm/mm]
0,	8,6405e-004	-2,3549e-003	3,0193e-004
3,3333	-3,4968e-004	4,745e-004	-3,8465e-005
6,6667	-1,4783e-004	2,7265e-004	-3,8468e-005
10,	-6,4753e-005	1,8958e-004	-3,8469e-005

Figure 5.46 Strain results in unloading stage (Pa=666 MPa)

5.4 Comparison of the Results

In this section, experimental and numerical results are compared with each other in terms of strain results in both loading and unloading steps and residual stress (radial and tangential) results.

5.4.1 Comparison of Strain Results

Resulting strains in tangential and axial directions at the outer surface of the cylinder are given in Tables 5.6 and 5.7 for loading and unloading steps respectively. As it is seen in the Tables, strain values for both methods increase with an increase in the pressure and the clamping force. Also, the results are close to each other. The mean absolute percentage error (MAPE) is calculated as 10.1% and 9.0% from tangential and axial strain results respectively. Those error ranges may be considered as a reasonable deviation.

Table 5.6 Numerical and experimental strain results (loading step)

Pa (MPa)	Fc (kN)	Tangential Strain x10^6		Axial strain x 10^6	
		FEM Results	Strain gauge M.	FEM Results	Strain gauge M.
530	124	881	899	-833	-791
550	126	919	941	-847	-825
570	127	957	978	-853	-832
587	128	992	1018	-859	-865
608	130	1038	1065	-873	-880
628	132	1085	1072	-888	-895
646	133	1128	1115	-896	-903
666	134	1178	1167	-904	-910

Table 5.7 Numerical and experimental strain results (unloading step)

Pa (MPa)	Fc (kN)	Tangential Strain x10^6		Axial strain x 10^6	
		FEM Results	Strain gauge M.	FEM Results	Strain gauge M.
530	124	55	71	-12	-17
550	126	68	83	-15	-21
570	127	84	103	-18	-20
587	128	98	143	-21	-23
608	130	119	157	-25	-25
628	132	141	175	-29	-37
646	133	163	182	-34	-39
666	134	190	193	-38	-47

5.4.2 Comparison of Residual Stress Results

In order to compare the experimental results with numerical results, the lowest and the highest stress values within the radial measurement range are determined from the numerical results and it is examined whether the experimental results are between these values or not. Both experimental and numerical results are given in Tables 5.8 and 5.9. It is seen in the Tables that the experimental results are generally very close to the range values. The values that are not within range are shown in italic style in these tables.

Table 5.8 Experimental and numerical residual radial stress results

Meas. Point	**Radial Range (mm)**	**Pa= 530 MPa Fc=124 kN**		**Pa=550 MPa Fc=126 kN**		**Pa=570 MPa Fc=127 kN**		**Pa=587 MPa Fc=128 kN**	
		FEM	**EXP**	**FEM**	**EXP**	**FEM**	**EXP**	**FEM**	**EXP**
1	5-6	(-27) – (-2)	-23.8	(-32) – (-3)	-29.8	(-36) – (-3)	-26.4	(-40) – (-3)	-37.7
2	6-7	(-27) – (-21)	***-31.3***	(-32) – (-26)	-28.6	(-38) – (-32)	***-42.5***	(-42) – (-38)	***-32.3***
3	7-8	(-21) – (-15)	***-24.2***	(-28) – (-18)	-28.3	(-33) – (-22)	-22.1	(-38) – (-26)	-36.1
4	10-11	(-7) – (-5)	***-13.3***	(-10) – (-6)	-10.6	(-12) – (-8)	-12.0	(-13) – (-9)	***-15.8***
5	12-13	(-3) – (-2)	***-0.1***	(-4) – (-2)	-3.0	(-5) – (-3)	-2.7	(-6) – (-3)	-2.8
Meas. Point	**Radial Range (mm)**	**Pa= 608 MPa Fc=130 kN**		**Pa=628 MPa Fc=132 kN**		**Pa=646 MPa Fc=133 kN**		**Pa=666 MPa Fc=134 kN**	
		FEM	**EXP**	**FEM**	**EXP**	**FEM**	**EXP**	**FEM**	**EXP**
1	5-6	(-45) – (-4)	-41.0	(-50) – (-4)	-43.9	(-54) – (-4)	-53.3	(-59) – (-4)	-55.9
2	6-7	(-49) – (-44)	***-53.3***	(-55) – (-48)	-48.2	(-61) – (-53)	***-63.6***	(-66) – (-58)	-63.9
3	7-8	(-46) – (-31)	-31.1	(-53) – (-38)	-40.5	(-59) – (-44)	-52.3	(-66) – (-51)	-51.9
4	10-11	(-16) – (-11)	-15.3	(-19) – (-13)	-14.7	(-22) – (-15)	-20.0	(-26) – (-17)	-19.6
5	12-13	(-7) – (-4)	***-8.8***	(-9) – (-5)	-7.3	(-10) – (-6)	-9.3	(-12) – (-7)	-10.2

Table 5.9 Experimental and numerical residual tangential stress results

Meas. Point	**Radial Range (mm)**	**Pa= 530 MPa Fc=124 kN**		**Pa=550 MPa Fc=126 kN**		**Pa=570 MPa Fc=127 kN**		**Pa=587 MPa Fc=128 kN**	
		FEM	**EXP**	**FEM**	**EXP**	**FEM**	**EXP**	**FEM**	**EXP**
1	5-6	(-285) – (-47)	-86.4	(-316) – (-71)	-96.9	(-346) – (-95)	-122.2	(-377) – (-116)	-161.2
2	6-7	(-57) – (36)	30.0	(-82) – (43)	1.5	(-106) – (50)	-74.9	(-127) – (56)	-100.9
3	7-8	(26) – (33)	***36.3***	(33) – (41)	***56.6***	(40) – (50)	***4.3***	(47) – (56)	***8.7***
4	10-11	(17) – (19)	***31.3***	(21) – (24)	24.6	(25) – (29)	***55.1***	(30) – (34)	***48.6***
5	12-13	(14) – (15)	***9.3***	(17) – (19)	***27.4***	(21) – (23)	***37.5***	(24) – (27)	***30.4***
Meas. Point	**Radial Range (mm)**	**Pa= 608 MPa Fc=130 kN**		**Pa=628 MPa Fc=132 kN**		**Pa=646 MPa Fc=133 kN**		**Pa=666 MPa Fc=134 kN**	
		FEM	**EXP**	**FEM**	**EXP**	**FEM**	**EXP**	**FEM**	**EXP**
1	5-6	(-415) – (-141)	-203.8	(-451) – (-164)	-156.5	(-484) –(-185)	-210.3	(-519) – (-208)	-206.2
2	6-7	(-152) – (40)	-103.3	(-176) – (21)	-100.2	(-197) – (5)	-123.6	(-220) – (-14)	-146.9
3	7-8	(33) – (65)	***8.5***	(14) – (74)	***3.0***	(-3) – (83)	5.3	(-22) – (92)	1.3
4	10-11	(36) – (41)	41.8	(43) – (49)	***67.1***	(50) – (57)	***60.2***	(58) – (66)	***72.0***
5	12-13	(30) – (33)	***23.9***	(35) – (39)	***25.2***	(41) – (45)	***53.2***	(47) – (52)	***67.7***

Residual stress distributions obtained from numerical and experimental results for each autofrettage test are given in Figures 5.47 to 5.54. In these plots, the position of each measurement is considered at the middle of the coverage area of the probe.

It is seen that the XRD results for radial stresses almost completely overlap with the numerical results for all pressure values. A similar situation occurs for the tangential stresses. However, there is a slight deviation from the hoop stress curvature especially in the third measurement points. Immediate changes in the stresses at elastic–plastic interface may cause this deviation.

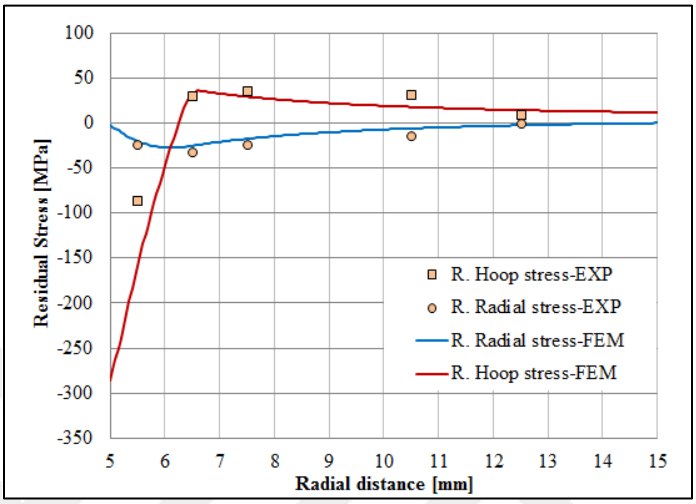

Figure 5.47 Radial and tangential (hoop) residual stresses (Pa=530 MPa)

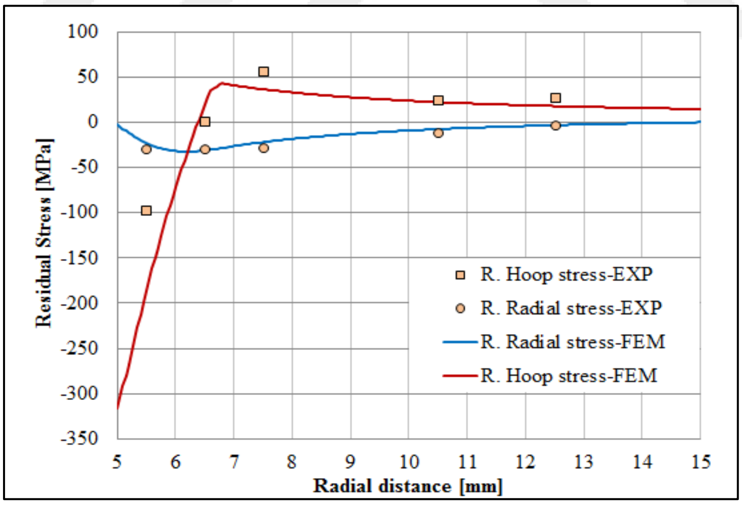

Figure 5.48 Radial and tangential (hoop) residual stresses (Pa=550 MPa)

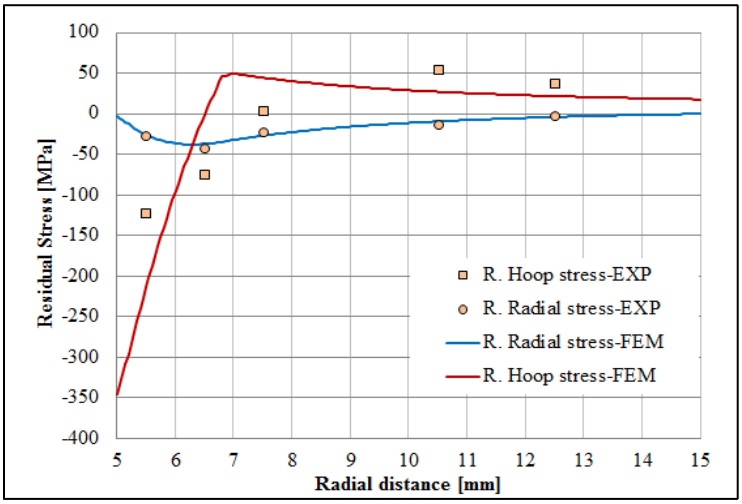

Figure 5.49 Radial and tangential (hoop) residual stresses (Pa=570 MPa)

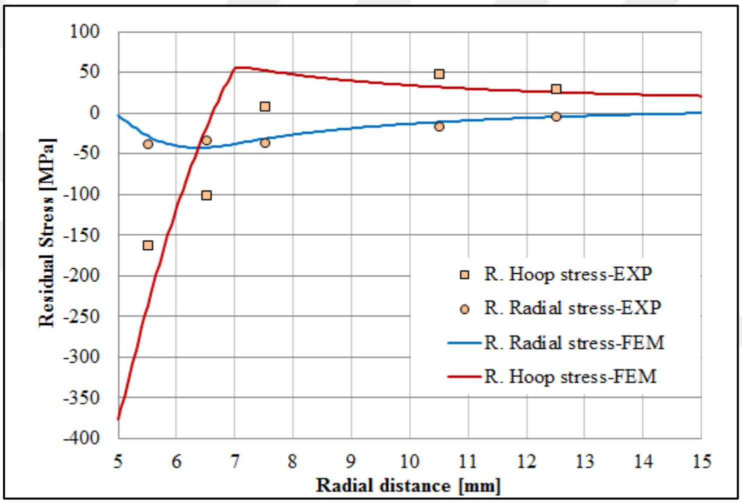

Figure 5.50 Radial and tangential (hoop) residual stresses (Pa=587 MPa)

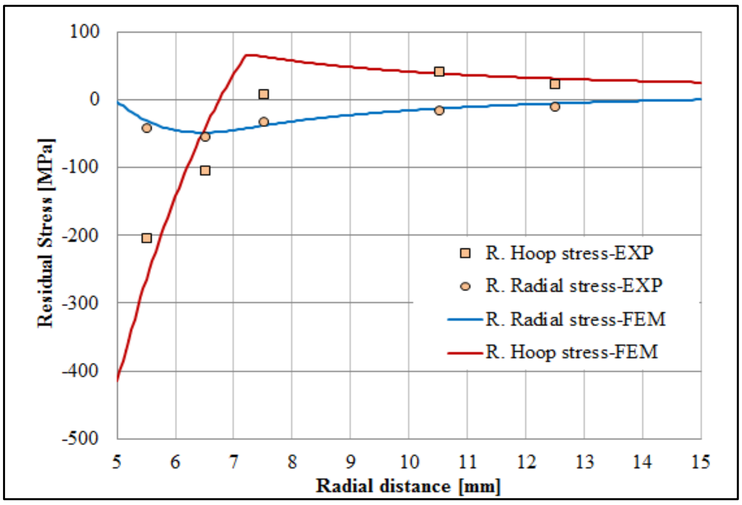

Figure 5.51 Radial and tangential (hoop) residual stresses (Pa=608 MPa)

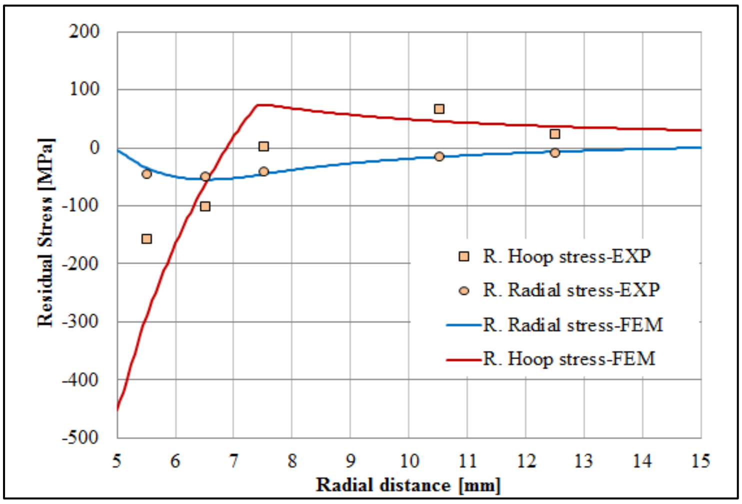

Figure 5.52 Radial and hoop residual stresses (Pa=628 MPa)

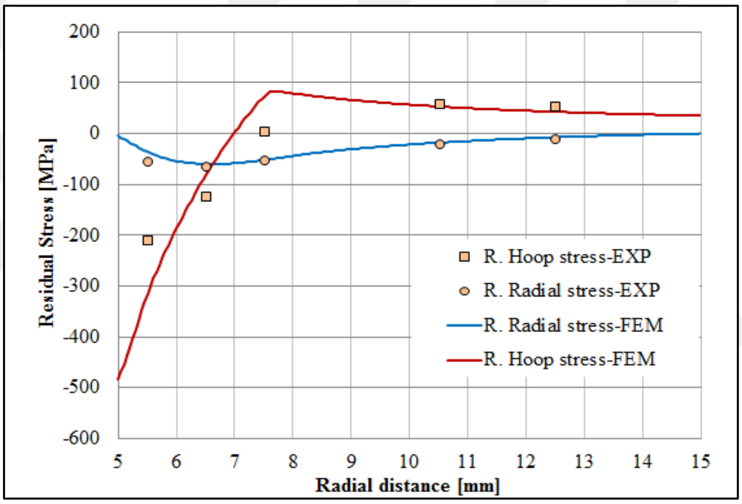

Figure 5.53 Radial and hoop residual stresses (Pa=646 MPa)

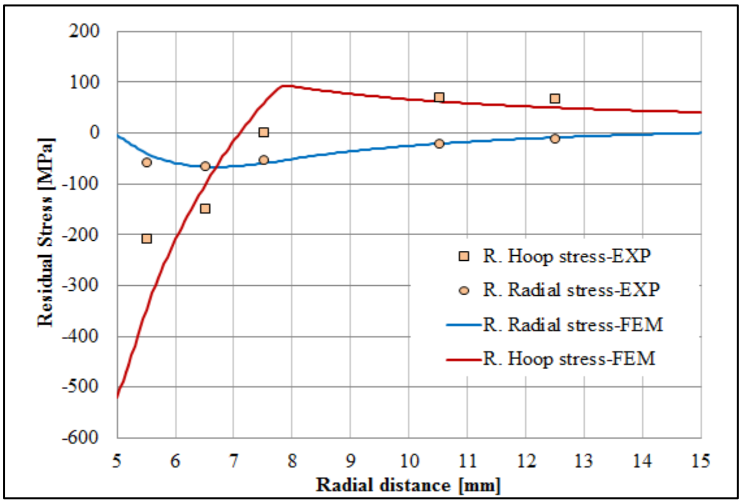

Figure 5.54 Radial and hoop residual stresses (Pa=666 MPa)

CHAPTER 6

CONCLUSIONS AND FUTURE WORKS

6.1 Introductıon

In this study, residual stress distributions and strain values at loading and unloading stages for thick-walled cylinders subjected to different autofrettage pressures are obtained experimentally. Residual stresses are measured at five different points along the thickness of the cylinders by XRD method. The residual stresses resulting from the cutting process are eliminated by electro polishing. A 2D axisymmetric model based on the experimental setup was developed in ANSYS® Workbench 15.0 and the experimental results are compared with the FE analysis results.

As a conclusion, following remarks are derived from this investigation:

- XRD method can be safely used in the determination of residual stresses for autofrettaged cylinders if only it is used together with the electro-polishing process. In a similar study, Jain et al. [32] found a significant difference between the XRD residual stress results and numerical results. The difference may be due to the lack of using electro-polishing process before the measurements.
- Almost all residual radial stresses determined experimentally agree with the numerical results, while there are some differences in tangential stress results. Owing to the nature of the probe used in the XRD measurements it is not possible to measure the residual stresses at any exact point on the wall of the cylinder. This may be the reason why some of the results are not in the range values of numerical results specified for each location.
- Compressive residual stresses are developed at the inner surface due to the autofrettage process and the magnitude of those stresses increases with an increase in the autofrettage pressure.

- For all autofrettage pressure values used in this study, the residual stresses become less than yield strength in compression (S_{yc}) at the inner surface which indicates that there is no reverse yielding in the working pressure range.
- The plastic region increases with respect to the autofrettage pressure. The amount of increase in the elastic-plastic interface radius is found to be approximately 0.01 mm/MPa. It is also found that about 13% to 28% of the thickness of the material is undergone plastic deformation for 530 MPa to 666 MPa autofrettage pressures respectively.
- The highest Von Misses stress in the working stage occurs at the elastic-plastic interface for autofrettaged cylinders while it occurs at the inner surface for non-autofrettaged cylinders.
- The values of maximum Von-Misses stress for 200 MPa working pressure are determined for both non-autofrettaged and autofrettaged cylinders. For non-autofrettaged cylinders it is calculated as 389 MPa from the Lâme equations. For autofrettaged cylinders they are found as 281, 280, 280, 279, 280, 282, 284 and 287 MPa for the autofrettage values of 530, 550, 570, 587, 608, 628, 646 and 666 MPa respectively. It is seen that, the stress values decreases first and then increases after a certain value. For the autofrettage pressure values used in this thesis, minimum stress value for 200 MPa working pressure is obtained as 279 MPa for 587 MPa autofrettage pressure.
- There is a considerable increase in strains at the first 3-6 seconds of pressure holding time depending on the autofrettage pressure and then they are remaining almost constant for the rest of the time. Basara et al. [34] found similar results for fuel injection lines, but they found much longer pressure holding time to complete plastic deformation. They also suggested that the components should be autofrettaged at some higher pressure for a short period instead of keeping them for a longer period at the pressure determined by analytical calculations. It is not found such a relationship between autofrettage pressure and holding time in this study. It may be only said that the increase in the strains with pressure holding time should be taken into account in mass production for more accurate results and the pressure holding time should not be taken less than 3 seconds.

- Strain results are found to be in agreement with numerical results and the mean average percentage error (MAPE) is calculated as 10.1% and 9.0% from tangential and axial strains respectively. This error ranges may be considered as a reasonable deviation.
- The FE model developed in this study can safely be used in the determination of residual stresses on the wall of pressurized cylinders for similar applications.

6.2 Future Works

The following subjects can be examined for further investigations about this study:

- This work can be extended to those cylindrical parts which may have discontinuities in shape like fuel rails in diesel engines.
- Different residual stress measurement techniques may be applied in an experimental study and the results obtained from each method may be compared.
- Different material models may be tried in FE analysis and the differences between the results may be compared.
- In addition to the working pressure and the Bauschinger effect, an optimization study can be carried out in which the effect of the pressure holding time is also included.
- The effect of autofrettage process on fatigue life is not evaluated in this thesis. This topic can be examined in a future study and it may be a very useful study especially for automotive industry.
- High pressure cylinders of intensifier pumps are imported from abroad with high prices. A hydraulic autofrettage test stand may be designed and produced within the scope of university-industry cooperation to produce these components in our country.
- Analytical analysis for the cases of having compressive axial load during autofrettage process can be carried out.

REFERENCES

[1] Darijani, H., Kargarnovin M. H., and R. Naghdabadi. (2009). Design of thick-walled cylindrical vessels under internal pressure based on elasto-plastic approach. *Materials & Design.* **30**, 3537-3544.

[2] Nath, Rashmi Ranjan. (2011). Design and Analysis of Thick walled cylinders with holes. *PhD Thesis*, National Institute of Technology.

[3] Abdelsalam, O. R. (2012). Analysis and Optimization of Autofrettaged and Shrink-Fitted Compound Cylinders under Thermo-Mechanical Loads. *PhD Thesis*, Concordia University.

[4] Shim W.S., Kim J.H., Lee Y.S., Cha, K.U., Hong S.K. (2010). A study on hydraulic autofrettage of thick-walled cylinders incorporating bauschinger effect. *Exp Mech*., **50**, 621–626.

[5] Kamal S.M., Dixit U.S. (2015). Feasibility study of thermal autofrettage of thick-walled cylinders. *J Press Vessel Technol*., **137**, 335-376.

[6] Zare H.R., Darijani H. (2016). A novel autofrettage method for strengthening and design of thick-walled cylinders. *Mater Des*., **105**, 366–374.

[7] Malik M.A., Khushnood S. (2003). A review of swage-autofrettage process. *Conf Nucl. Eng*., 1–12.

[8] Shufen, R., and Dixit, U.S. (2018). A review of theoretical and experimental research on various autofrettage processes. *Journal of Pressure Vessel Technology*.

[9] Hill R. 1950. The mathematical theory of plasticity. New York: Clarendon Press Oxford.

[10] Topçu F. and Filiz İ.H., (2009). Yüksek Basınç Silindirleri Tasarımında Farklı Yöntemler. *Makine Tasarım ve İmalat Teknolojileri Kongresi*, Konya.

[11] Milligan, R. V., W. H. Koo, and T. E. Davidson. (1966). The Bauschinger effect in a high-strength steel. *Journal of Basic Engineering.* **88**(2), 480-488.

[12] Huang XP. (2005). A general autofrettage model of a thick-walled cylinder based on tensile-compressive stress-strain curve of a material. *J Strain Anal Eng Des*. **40**, 599–607.

[13] Çandar, Hakan, and İ. Hüseyin Filiz. (2017). Optimum autofrettage pressure for a high pressure cylinder of a waterjet intensifier pump. *Universal Journal of Engineering Science* **5**(3), 44-55.

[14] White, C. S., Bronkhorst, C. A., and Anand L. (1990). An improved isotropic-kinematic hardening model for moderate deformation metal plasticity. *Mechanics of Materials.* **10**(1-2), 127-147.

[15] Parker A., and Underwood J. H. (1998). Influence of the Bauschinger Effect on Residual Stress and Fatigue Lifetimes in Autofrettaged Thick-Walled Cylinders. *Fatigue and Fracture Mechanics.* **29**.

[16] Parker A. (2001). Autofrettage of Open-End Tubes Pressures, Stresses, Strains, and Code Comparisons. *Journal of Pressure Vessel Technology*. **123**, 271-281.

[17] Lee E. Y., Lee Y. S., Yang Q. M., Kim J. H., Cha K. U., Hong S. K. (2009). Autofrettage process analysis of a compound cylinder based on the elastic-perfectly plastic and strain hardening stress-strain curve. *Journal of Mechanical Science and Technology*. **23**(12), 3153-3160.

[18] Chen P. C. T. (1986). The Bauschinger and hardening effect on residual stresses in an autofrettaged thick-walled cylinder. *Journal of Pressure Vessel Technology.* **108**, 108-112.

[19] Ragab A., Abbas A., Khorshied S. (2001). Experimental verification of the autofrettage process for thickwalled tubes. *J Mech Eng Sci*. **215**, 727–736.

[20] Chen P. T., and O'hara G. P. (1983). Finite element results of pressurized thick tubes based on two elastic-plastic material models. Army Armament Research and Development Center Watervliet NY Large Caliber Weapon Systems Lab,. ARLCB-TR-83047.

[21] Gibson M. C., Parker A. P., Hameed A., Hetherington J. G. (2012). Implementing Realistic, Nonlinear, Material Stress–Strain Behavior in ANSYS for the Autofrettage of Thick-Walled Cylinders. *Journal of Pressure Vessel Technology*, **134**(5), 051202.

[22] Feng H., Donth B., and Mughrabi H. (1998). Finite-element modelling of low-temperature autofrettage of thick-walled tubes of the austenitic stainless steel AISI 304 L: Part II. Thick-walled tube with cross-bore. *Modelling and Simulation in Materials Science and Engineering* **6**(1).

[23] Jahed, Hamid, Mohammad Reza Faritus, and Zeinab Jahed. (2012). Residual stress measurements in an autofrettage tube using hole drilling method. *Journal of Pressure Vessel Technology*. **134**, 051501.

[24] George D., and Smith D. J. (2000). The application of the deep hole technique for measuring residual stresses in an autofrettaged tube. *ASME-Publications-Pvp*. **406**, 25-32.

[25] Franklin G. J. and Morrison J. L. M. (1960). Autofrettage of cylinders: prediction of pressure/external expansion curves and calculation of residual stresses. *Proceedings of the Institution of Mechanical Engineers*. **174**, 947-974.

[26] Faupel J. H. (1955). Residual stresses in heavy-wall cylinders. *Journal of the Franklin Institute* **259**, 405-419.

[27] Stacey, A., and Webster G. A. (1988). Determination of residual stress distributions in autofrettaged tubing. *International Journal of Pressure Vessels and Piping* **31**, 205-220.

[28] Parker A. P., Underwood J. H., Kendall D. P. (1999). Bauschinger effect design procedures for autofrettaged tubes including material removal and Sachs' method. *Journal of pressure vessel technology*. **121**, 430-437.

[29] Parker A. P. (2004). A critical examination of Sachs' material-removal method for determination of residual stress. *Journal of pressure vessel technology*. **126**, 234-236..

[30] Ma Y., Zhang S. Y., Goodway C., Done R., Evans B., Kirichek O., Bowden, Z. (2012). A non-destructive experimental investigation of elastic plastic interfaces of autofrettaged thick-walled cylindrical aluminium high pressure vessels. High Pressure Research, **32**, 364-375.

[31] Lee S.L, Britt L., Capsimalis G. (1994). Nondestructive characterization of materials VI. In: Green RE, Kozaczek KJ, Ruud CO, editors. Nondestructive characterization of materials VI. Boston (MA).

[32] Jain A., Khanwelkar S., Saurav K. (2016). Design and performance of hydraulic autofrettage using universal testing machine. IJRMET. **6**, 154–157.

[33] Venter A. M., Swardt R. R., Kyriacou S. (2000). Comparative measurements on autofrettaged cylinders with large Bauschinger reverse yielding zones. *The Journal of Strain Analysis for Engineering Design*. **35**, 459-469.

[34] Basara A., Alt N., Schlücker E. (2011). Influence of the pressure holding time on strain generation in fuel injection lines. *International Journal of Pressure Vessels and Piping*. **88**, 132-137.

[35] Majzoobi G. H., Farrahi G. H., Mahmoudi A. H. (2003). A finite element simulation and an experimental study of autofrettage for strain hardened thick-walled cylinders. *Materials Science and Engineering*. A, **359**(1-2), 326-331.

[36] Zeng Xiaoying, Li Gangling. (1984). Proceeding of the 5th International conference on pressure vessel technology, vol. 1, ASME United Engineering Center, New York. 85-95.

[37] Seifi R. and Babalhavaeji M. (2012). Bursting pressure of autofrettaged cylinders with inclined external cracks. *International Journal of Pressure Vessels and Piping*. **89**, 112-119.

[38] Maleki M., Farrahi G. H., Jahromi B. H., Hosseinian E. (2010). Residual stress analysis of autofrettaged thick-walled spherical pressure vessel. *International Journal of Pressure Vessels and Piping*, **87**(7), 396-401.

[39] Varga L. (1991). Design of optimum high-pressure monobloc vessels. *International journal of pressure vessels and piping*. **48**(1), 93-110.

[40] Zhu R. and Yang J. (1998). Autofrettage of thick cylinders. *International Journal of Pressure Vessels and Piping*. **75**(6), 443-446.

[41] Majzoobi G. H. and Ghomi A. (2006). Optimisation of autofrettage in thick-walled cylinders. *Journal of Achievements in Materials and Manufacturing Engineering*. **16**(1), 2.

[42] Hojjati M. H. and Hassani A. (2007). Theoretical and finite-element modeling of autofrettage process in strain-hardening thick-walled cylinders. *International Journal of Pressure Vessels and Piping*. **84**(5), 310-319.

[43] Ali, A. R. M. and Ghosh N. C. (2010). Optimum design of pressure vessel subjected to autofrettage process. *International Journal of Mechanical, Aerospace, Industrial, Mechatronic and Manufacturing Engineering*, **4**(10), 1040-1045.

[44] Filiz İ. H., 2013. Solved Problems Machine Elements, vol. 1, Gaziantep, pp. 14-19.

[45] Majet Su Jeti ile Kesme Sanayi, Biksan Sanayi Sit., Istanbul-TURKEY.

[46] Dreamstime. https://www.dreamstime.com/photos-images/cannon-barrel.html. Accessed 13.04.2018.

[47] Kobelev V. (2010). Theory of optimal residual stresses and defects distribution. *Structural and Multidisciplinary Optimization*. **41**(3), 351-370.

[48] Partovi, A. and Saadat S., (2012). Analysis of autofrettaged high pressure components. M.Sc. Thesis, Blekinge Institute of Technology, Sweden.

[49] Tomita, N. (1983). Autofrettage process. U.S. Patent No. 4,417,459. 29 Nov.

[50] Maximator Test, LLC. http://maximator-test.com/autofrettage/. Accessed 13.04.2018.

[51] Malik M. A. and Khushnood S. (2003). A review of swage-autofrettage process. In Proceedings of the 11th International Conference on Nuclear Engineering, Tokyo, Japan, 20-23.

[52] Kampmann B. and Diemer J. (2007). Autofrettage process and autofrettage apparatus. Patent US8408033B2, 7 08.

[53] Carter R.H., and William S.D. (2013). Compressed elastomer process for autofrettage and lining tubes. U.S. Patent No. 8,418,392. 16.

[54] Ezra, A., (1973). Method and apparatus for explosive autofrettage. U.S. Patent No 3,751,954.

[55] Berman I., and David H. P. (1969). Creep autofrettage. U.S. Patent No. 3,438,114. 15 Apr.

[56] Abdelsalam O. M. R. Y. (2012). Analysis and Optimization of Autofrettaged and Shrink-Fitted Compound Cylinders Under Thermo-Mechanical Loads. PhD. Thesis, Concordia University, Canada.

[57] Bauschinger J. (1881). Ueber die veranderung der elasticitatsgrenze und elastcitatsmodul verschiedener. Metal Civiling N.F., **27**, 289-348.

[58] Bate P. S., and Wilson D. V. (1986). Analysis of the Bauschinger effect. *Acta Metallurgica*. **34**(6), 1097-1105.

[59] Deak G. I. (1962). A study on the causes of the Bauschinger effect. PhD. Thesis, Massachusetts Institute of Technology.

[60] Youtsos A. (2006). Residual Stress and Its Effects on Fatigue and Fracture. 16th European Conference of Fracture – ECF16, Alexandroupolis, Greece.

[61] Pugh, H. L. D. 1971. Mechanical behaviour of materials under pressure. England:Applied Science Publishers.

[62] Budynas R. G. 2008. Shigley's mechanical engineering design. New York: McGraw-Hill.

[63] Maximator GmbH. Autofrettage and burst pressure test stand operating manual Project:P140009/PN 497

[64] 2A Kalıp Makina, Üçevler Mah. 81.sk., Bursa, Turkey

[65] Kudryavtsev Y. F. (2008). Residual stress. In Springer Handbook of Experimental Solid Mechanics (pp. 371-388). Springer US.

[66] Rossini N. S., Dassisti M., Benyounis K. Y., Olabi A. G. (2012). Methods of measuring residual stresses in components. *Materials & Design*. **35**, 572-588.

[67] Megahed M. M. and Abbas A. T. (1991). Influence of reverse yielding on residual stresses induced by autofrettage. *International journal of mechanical sciences*. **33**(2), 139-150.

[68] Micro-Measurements, V. (2007). Measurement of residual stresses by the hole drilling strain gage method. Tech Note TN, 503.

[69] Stresstech. https://www.stresstech.com/en-fi/products/espi-hole-drilling-equipment/. Accessed 13.04.2018.

[70] Paranjpe, S. (2005). Measurement of residual stress in materials using neutrons. In Proc. of a Technical Meeting. Vienna, Italy.

[71] Fitzpatrick M. E., Fry A. T., Holdway P., Kandil F. A., Shackleton J., Suominen L. (2005). Determination of residual stresses by X-ray diffraction. National Physical Laboratory, Teddington, UK.

[72] Madenci, E. and Guven I. (2015). The finite element method and applications in engineering using ANSYS®. Springer.

[73] Huebner, Kenneth H. 2001. The finite element method for engineers. NY:John Wiley & Sons.

[74] Maximator GmbH. Autofrettage technology and equipments. Customer presentation.

CURRICULUM VITAE

PERSONAL INFORMATION

Name and Surname: Hakan ÇANDAR

Nationality: Turkish

Birth place and date: ERZİNCAN/Merkez – 25.09.1985

Marital status: Married

Phone number: +90(505)9666895

Email: candar@gantep.edu.tr

EDUCATION

	Graduate school	Year
Master	University of Gaziantep	2012
Bachelor	Cumhuriyet University	2008
High School	Bursa-Nilüfer Milli Piyango A.L.	2003

Work experience

	Place	Enrollment
2009-Present	University of Gaziantep	Research Assistant

PUBLICATIONS

Refereed Journal Publications

Çandar, H., and Filiz, İ. H. (2017). Experimental study on residual stresses in autofrettaged thick-walled high pressure cylinders. *High Pressure Research*, **37**(4), 516-528.

Çandar, H., and Filiz, İ. H. (2017). Optimum autofrettage pressure for a high pressure cylinder of a waterjet intensifier pump. *Universal Journal of Engineering Science*, **5**(3), 44-55.

Refereed Conference Proceedings

Çandar, H., Filiz, İ.H., (2015). Optimum Autofrettage Pressure for a High Pressure Cylinder of a Waterjet Intensifier Pump. *International Conference on Engineering and Natural Science*, Sokpje, Macedonia.

Çandar, H., Filiz, İ.H., (2012). Effects of Abrasive Waterjet Cutting Parameters on the Surface Quality of Al 7075. *15th International Conference on Machine Design and Production*, Denizli, Turkey.

Çandar, H., Filiz, İ.H., (2012). ASJ Kesme İşleminde Tam Faktöriyel ile Taguchi Deney Tasarimi Yöntemlerinin Yüzey Pürüzlülüğü Tahmin Modeli Oluşturmadaki Etkileri. *3. Ulusal Talaşlı İmalat Sempozyumu*, Ankara, Turkey.

FOREIGN LANGUAGE

English,

YOKDIL: 84.00, 2017

UDS: 77.50, 2017.